

Radiative torques: analytical model and basic properties

A. Lazarian¹★ and Thiem Hoang²★

Department of Astronomy, University of Wisconsin, Madison, WI 53706, USA

Accepted 2007 March 29. Received 2007 March 28; in original form 2006 December 15

ABSTRACT

We attempt to get a physical insight into grain alignment processes by studying basic properties of radiative torques (RATs). For this purpose we consider a simple toy model of a helical grain that reproduces well the basic features of RATs. The model grain consists of a spheroidal body with a mirror attached at an angle to it. Being very simple, the model allows analytical description of RATs that act upon it. We show a good correspondence of RATs obtained for this model and those of irregular grains calculated by DDSCAT. Our analysis of the role of different torque components for grain alignment reveals that one of the three RAT components does not affect the alignment, but induces only for grain precession. The other two components provide a generic alignment with grain long axes perpendicular to the radiation direction, if the radiation dominates the grain precession, and perpendicular to magnetic field, otherwise. The latter coincides with the famous predictions of the Davis–Greenstein process, but our model does not invoke paramagnetic relaxation. In fact, we identify a narrow range of angles between the radiation beam and the magnetic field, for which the alignment is opposite to the Davis–Greenstein predictions. This range is likely to vanish, however, in the presence of thermal wobbling of grains. In addition, we find that a substantial part of grains subjected to RATs gets aligned with low angular momentum, which testifies that most of the grains in diffuse interstellar medium do not rotate fast, that is, rotate with thermal or even subthermal velocities. This tendency of RATs to decrease grain angular velocity as a result of the RAT alignment decreases the degree of polarization, by decreasing the degree of internal alignment, that is, the alignment of angular momentum with the grain axes. For the radiation-dominated environments, we find that the alignment can take place on the time-scale much shorter than the time of gaseous damping of grain rotation. This effect makes grains a more reliable tracer of magnetic fields. In addition, we study a self-similar scaling of RATs as a function of λ/a_{eff} . We show that the self-similarity is useful for studying grain alignment by a broad spectrum of radiation, that is, interstellar radiation field.

Key words: polarization – dust, extinction – ISM: magnetic fields.

1 INTRODUCTION

Magnetic fields play a crucial role in many astrophysical processes, for example, star formation, accretion of matter, transport processes, including heat conduction and propagation of cosmic rays. One of the easiest ways to study magnetic field topology is via polarization of radiation arising from extinction or/and emission by aligned dust grains. The new instruments like Scuba II (Bastien, Jenness & Molnar 2005), Sharc II (Novak et al. 2004) and an intended polarimeter for SOFIA open new horizons for tracing of astrophysical magnetic fields with aligned grains.

In this situation it is unacceptable that the processes of grain alignment are not completely understood (see review by Lazarian

2003). The enigma that surrounds grain alignment since its discovery in 1949 (Hall 1949; Hiltner 1949) makes the interpretation of the polarization in terms of magnetic fields somewhat unreliable. The failure of grains to align at high optical depths was discussed, for instance, in Goodman et al. (1995).

A recent progress in understanding of the grain alignment physics removed many questions, but have not remedied the situation completely. Among the milestones let us mention the recent revival of interest to radiative torques (henceforth RATs). Introduced by Dolginov & Mytrophanov (1976), those torques, which arise from the interaction of irregular grains with a flow of photons, were essentially forgotten till Draine & Weingartner (1996, 1997, hereafter DW96, DW97, respectively) provided quantitative numerical studies. While Dolginov & Mytrophanov (1976) were somewhat vague on what makes RATs important for a grain, DW96 demonstrated that their arbitrary chosen irregular grains exhibit

★E-mail: lazarian@astro.wisc.edu (AL); hoang@astro.wisc.edu (TH)

dynamically important RATs when subjected to a typical interstellar radiation field (ISRF). Very importantly, Bruce Draine incorporated RATs into the *publicly available* DDSCAT code (Draine & Flatau 1994), which stimulated a further progress in the field. First laboratory studies of RATs were reported in Abbas et al. (2004).

The renewed interest to RATs coincided with a crisis of the paramagnetic alignment as it is described in textbooks (Purcell 1979; Spitzer & McGlynn 1979; Mathis 1986). Lazarian & Draine (1999a) (hereafter LD99a) identified new elements of grain dynamics, which they termed ‘thermal flipping’ and ‘thermal trapping’. Due to thermal wobbling arising from the dissipative coupling of grain vibrational and rotational degrees of freedom (Lazarian 1994; Lazarian & Roberge 1997) grains smaller than a critical radius a_c flip frequently and thus average out uncompensated torques. These torques, which were first discussed by Purcell (1979), were considered essential to make otherwise inefficient paramagnetic alignment (Davis & Greenstein 1951; Jones & Spitzer 1967) to account for the polarimetric observations. A new dissipative coupling mechanism related to nuclear spins of constituent atoms, which was described in Lazarian & Draine (1999b) (hereafter LD99b), resulted in a_c larger than the typical cut-off scale for grains in diffuse interstellar medium (ISM). As the other mechanisms, for example, mechanical alignment (Gold 1951, review by Lazarian 2003 and references therein), have their limitations, this made the RAT alignment the only viable mechanism to explain the ubiquity of interstellar polarization (DW97) and possibly polarization arising from aligned dust in other astrophysical environments (Lazarian 2007).

The successes of RATs include a more recent work by Cho & Lazarian (2005), where a substantial increase of the RAT efficiency with the grain size was established. This work explained the submillimetre polarization data for quiescent starless cores (Ward-Thompson et al. 2000) by appealing to the differential RAT alignment of large grains. For such cores the analysis of all other mechanisms in Lazarian, Goodman & Myers (1997) predicted only marginal degrees of alignment. The studies elaborating the approach in Cho & Lazarian (2005), for example, Pelkonen, Juvela & Padoan (2007) and Bethell et al. (2007), provided theory-motivated predictions of the degree of alignment for numerically simulated molecular clouds and cores.

However, the above explanation as well as other explanations (see Lazarian 2003) are based on the plausibility of arguments, rather than on the rigorous RAT alignment theory. Indeed, DW96 considered RATs as a means of spin-up. This induced a naive explanation of RAT alignment action that could be perceived in some of the papers that followed the DW96 study. There it was assumed that RATs were proxies of the Purcell’s torques (1979), which arise from the action of photons, rather than from the action of H₂ formation over catalytic sites, as in the original mechanism. While the Purcell’s torques depend on the resurfacing and therefore short lived, RATs depend on grain shape and can be long lived. As a result, long-lived fast rotation of paramagnetic grains should induce good paramagnetic alignment (Purcell 1979). This understanding of RATs is not correct, as it is clear from a more careful reading of DW96 and DW97.

In fact, RATs can be subdivided into the parts that arise from isotropic and anisotropic radiation fluxes. The part arising from anisotropic radiation, for which we adopt a shorthand notation ‘isotropic part’, is, indeed, similar to the Purcell’s torques. The ‘anisotropic part’ is, however, both usually stronger and has properties different from the Purcell’s torques. The major difference arises from the fact that RATs are defined in the laboratory, rather than in the grain coordinate system. Thus, the presence of even a small

anisotropic component of radiation, which is a natural condition for any realistic astrophysical system, is bound to change the dynamics of grain. Note that the alignment by the anisotropic radiation was first discussed by Dolginov & Mytrophonov (1976). They, however, concluded that prolate and oblate grains can be aligned differently. Lazarian (1995) took into account internal relaxation and claimed that both prolate and oblate grains should be aligned with longer axes perpendicular to magnetic field. Nevertheless, the theory lacked a proper description of RATs.

DW97 demonstrated numerically that in the presence of anisotropic radiation the grains can be aligned by RATs with respect to magnetic field on the time-scales much *shorter* than the time-scale for paramagnetic alignment.¹ In general, the magnetic field for the RAT alignment acts through inducing fast Larmor precession; the alignment potentially may happen both with long grain axes parallel and perpendicular to magnetic field. Only the latter is consistent with polarimetric observations, however (see Serkowski, Mathewson & Ford 1975).

In the DW97 study, the alignment with longer grain axes perpendicular to magnetic field (‘right alignment’) happened more frequently than the grain alignment with longer grain axes parallel to magnetic field (‘wrong alignment’). This experimental evidence, based on a limited sampling, raised worrisome questions. Is this a general property of RATs or just a coincidence? Do we expect to see more of ‘wrong alignment’ if the grain environment is different from the interstellar one? What are the chances that we are fooled by the ‘wrong alignment’ while interpreting the polarimetry measurements in terms of the underlying magnetic fields? It seems necessary to address these questions if interpreting polarimetry data in terms of underlying magnetic fields is sought.

Analytical calculations played an important role for formulating the models of both paramagnetic and mechanical alignment (see Davis & Greenstein 1951; Jones & Spitzer 1967; Purcell 1979; Spitzer & McGlynn 1979). Although such calculations dealt with intentionally idealized models of grains, they allowed deep insight into the relevant physics. Dolginov & Mytrophonov (1976) attempted an analytical modelling for RATs. They used a model grain containing two ellipsoids connected together at an angle. The RATs were calculated for such a model grain by assuming that the wavelength is much larger than the grain size, that is, in the Rayleigh–Hans approximation (Dolginov & Silantev 1976). However, adopting their shape, we could not reproduce numerically their analytical predictions for RATs. This induces us to seek analytical models (AMOs) that would correspond to the DDSCAT calculations.

Our approach in the present paper is to provide a physical insight into basic RAT properties. In Section 2 we explain why we consider only RATs due to anisotropic radiation. Then, we describe a simple grain model that is subject to RATs and allows analytical descriptions (Section 3). In Section 4 we present calculations of RATs for a number of irregular shapes and study the correspondence of their RATs with AMO. We also briefly consider possible generalizations of our model (Section 5). In Section 6 we analyse the alignment for both this model and irregular grains with respect to the radiation direction. In Section 7 we study the alignment of our model and irregular grains with respect to magnetic field. Crossovers are studied in Section 8, while we identify the conditions for the magnetic field or the radiation direction to act as the axis of alignment in Section 9.

¹ DW97 identifies this time-scale with the gaseous damping time. In Section 5.5 we show that the alignment could happen much faster in the presence of strong radiation sources.

As, even with modern computers, the calculations of RATs for a variety of wavelengths is time consuming, we address the question of the accuracy of presenting RATs as the function of the ratio of grain size to the wavelength λ/a_{eff} in Section 10. The discussion of our results and the summary are provided in Sections 11 and 12, respectively.

2 ISOTROPIC AND ANISOTROPIC RATs

RATs can emerge even when the radiation field is isotropic. Devices similar to those used by Lebedev (1901) to measure radiation pressure experience torques in the presence of the isotropic radiation (see also the cartoon of a model with absorbing and reflecting strips in DW96).

The dynamics of an irregular grain subjected to isotropic radiation is very similar to a grain subjected to the Purcell's torques arising, for instance, from H₂ formation. For instance, one would expect to have thermal trapping of sufficiently small grains due to thermal fluctuations as described in LD99a. Therefore RATs induced by isotropic radiation (henceforth ‘isotropic RATs’) only marginally alter the problems that the paramagnetic alignment mechanism faces in explaining observational data. In addition, as we mentioned above, the ‘isotropic RATs’ are usually weaker than those that arise when a grain is subjected to anisotropic radiation (see DW97).

Due to the situation described above, for the rest of the paper we shall associate RATs only with the part arising from anisotropic radiation, as, for instance, was done in Cho & Lazarian (2005). In other words, we treat the torques arising from isotropic radiation as a particular realization of the Purcell's torques.

Let us now introduce briefly some basic definitions. RAT Γ_{rad} is defined by

$$\Gamma_{\text{rad}} = \frac{\gamma u_{\lambda} \lambda a_{\text{eff}}^2}{2} Q_{\Gamma}, \quad (1)$$

where Q_{Γ} is the RAT efficiency, γ is the anisotropy degree and u_{λ} is the energy density of radiation field of the wavelength λ . Here a_{eff} is the effective size of the grain which is defined as the radius of a sphere of the same volume with the irregular grain (similar to DW97). In general, Q_{Γ} is a function of angles Θ, β, Φ in which Θ is the angle between the axis \hat{a}_1 corresponding to the maximal moment of inertia (henceforth maximal inertia axis) with respect to the radiation direction \mathbf{k} , β is the rotation angle of the grain around \hat{a}_1 , and Φ is the precession angle of \hat{a}_1 about \mathbf{k} (see Fig. 1). To help the reader familiar with the earlier works on RATs, wherever possible, we use the same notations as in DW96 and DW97.

The RAT efficiency can be decomposed into components in the scattering system via

$$\begin{aligned} Q_{\Gamma}(\Theta, \beta, \Phi) = & Q_{e1}(\Theta, \beta, 0)\hat{e}_1 \\ & + Q_{e2}(\Theta, \beta, 0)(\hat{e}_2 \cos \Phi + \hat{e}_3 \sin \Phi) \\ & + Q_{e3}(\Theta, \beta, 0)(\hat{e}_3 \cos \Phi - \hat{e}_2 \sin \Phi), \end{aligned} \quad (2)$$

where $\hat{e}_1, \hat{e}_2, \hat{e}_3$ are shown in Fig. 2. In addition, for the sake of simplicity, we have denoted $Q_{e1}(\Theta, \beta, 0) \equiv Q_{\Gamma}(\Theta, \beta, 0) \cdot \hat{e}_1$, $Q_{e2}(\Theta, \beta, 0) \equiv Q_{\Gamma}(\Theta, \beta, 0) \cdot \hat{e}_2$, $Q_{e3}(\Theta, \beta, 0) \equiv Q_{\Gamma}(\Theta, \beta, 0) \cdot \hat{e}_3$. In what follows, we use Q_{e1}, Q_{e2}, Q_{e3} for the RAT components and keep in mind that they are functions of Θ, β at $\Phi = 0$. However, in some particular cases, these angles will be explicitly written.

3 INTRODUCING ANALYTICAL MODEL OF A HELICAL GRAIN

Let us consider an asymmetric grain shape consisting of a reflecting spheroid and a square mirror with the side l_2 attached on a pole of

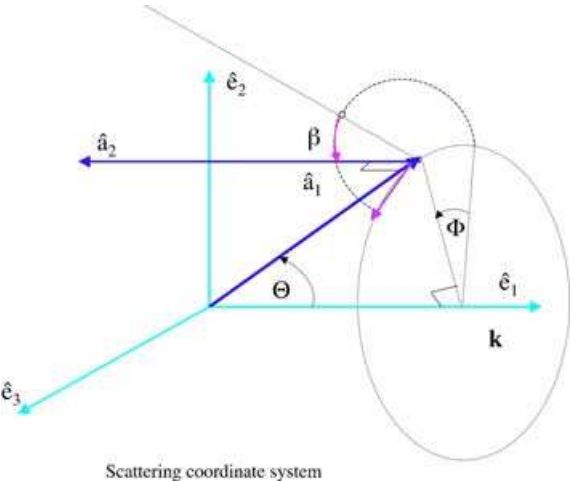


Figure 1. The orientation of a grain, described by three principal axes $\hat{a}_1, \hat{a}_2, \hat{a}_3$, in the laboratory coordinate system (scattering reference system) $\hat{e}_1, \hat{e}_2, \hat{e}_3$ is defined by three angles Θ, β, Φ . The direction of incident photon beam \mathbf{k} is along \hat{e}_1 .

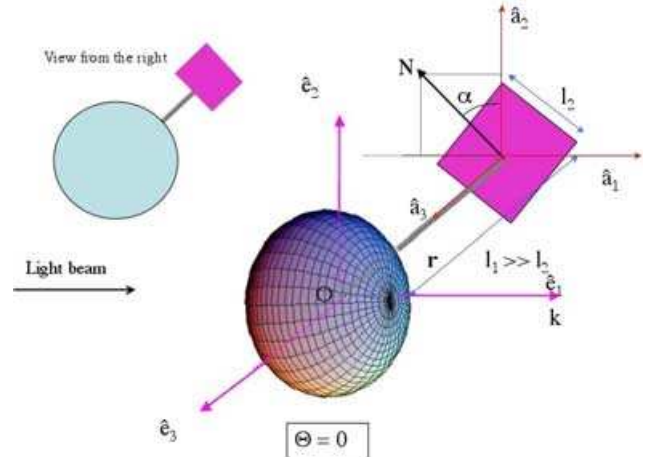


Figure 2. Our grain model consists of a mirror connected to an oblate spheroid by a weightless rod. The distance between the mirror and the spheroid is assumed to be much larger than the mirror's size. Both the mirror and the spheroid are perfectly reflecting.

the length l_1 . For the sake of simplicity, we assume that the mirror and the pole are weightless. Also, both the mirror and the spheroid are assumed to be perfectly reflecting. Moreover, we neglect the shadowing of the mirror by the grain by assuming that $l_1 \gg l_2$ (see Fig. 2).

3.1 RATs from a reflecting spheroidal body

Consider first RATs acting on an oblate spheroidal body. As a consequence of its symmetries, such a grain is not expected to exhibit any spin-up arising from RATs, provided that the incident radiation is not circularly polarized. The latter will be our assumption for the rest of the paper.

Consider a photon beam of wavelength λ , propagating in the \mathbf{k} -direction parallel to the axis \hat{e}_1 of the lab coordinate system (see Figs 1 and 2). The momentum of a photon is deposited to the grain as it reflects from the grain surface. As a result, the grain experiences a net torque.

For simplicity, we assume that the grain rotates fast around the maximal inertia axis, so averaging over such a rotation is suitable. Also, from equation (2) it follows that we only need to find RATs for $\Phi = 0$. Therefore, the resulting RAT is

$$\Gamma_{\text{rad}} = \frac{\gamma u_{\text{rad}} \lambda b^2}{2} (Q_{e1}\hat{e}_1 + Q_{e2}\hat{e}_2 + Q_{e3}\hat{e}_3), \quad (3)$$

where b is the length of the major axis of the spheroid, RAT components are given by (see Appendix A for their derivation)

$$Q_{e3} = \frac{2ea}{\lambda}(s^2 - 1)K(\Theta, e)\sin 2\Theta, \quad (4)$$

$$Q_{e1} = 0, \quad (5)$$

$$Q_{e2} = 0, \quad (6)$$

where $s = a/b < 1$ is the ratio of the minor to the major axes, $K(\Theta, e)$ is a fitting function depending on Θ and the eccentricity of the oblate spheroid (see the lower panel in Fig. A1).

Following equations (4)–(6) we see that a reflecting spheroidal grain does not produce any Q_{e1}, Q_{e2} , but Q_{e3} only. Therefore, it is easy to see that the only effect of RATs on the spheroidal grain is to cause the precession in the plane perpendicular to the radiation direction $\mathbf{k} \parallel \hat{e}_1$.

3.2 Torques from a reflecting mirror

Consider now torques that act upon the perfectly reflecting mirror attached at an angle to the oblate spheroid (see Fig. 2). The pole is considered too thin to interact with the radiation.² The normal unit vector \hat{N} which determines the orientation of the mirror in the grain coordinate system is given by

$$\hat{N} = n_1\hat{a}_1 + n_2\hat{a}_2, \quad (7)$$

where $\hat{a}_1, \hat{a}_2, \hat{a}_3$ are the principal axes of the grain (i.e. the principal axes of the spheroid because the mirror and the pole are weightless). Here $n_1 = \sin \alpha, n_2 = \cos \alpha$ with α the angle between \hat{N} and \hat{a}_2 (see Fig. 2).

Due to the rotation, the cross-section of the mirror with the surface area A , varies as (see Appendix B)

$$A_{\perp} = A|\hat{e}_1 \cdot \hat{N}| = A|n_1 \cos \Theta - n_2 \sin \Theta \cos \beta|. \quad (8)$$

Following the same above procedure (see Appendix B for detail), we get RAT

$$\Gamma_{\text{rad}} = \frac{\gamma u_{\text{rad}} \lambda l_2^2}{2} (Q_{e1}\hat{e}_1 + Q_{e2}\hat{e}_2 + Q_{e3}\hat{e}_3), \quad (9)$$

where l_2 is the size of the square mirror, l_1 is the length of the pole, and RAT components are given by

$$Q_{e1} = \frac{4l_1}{\lambda}|n_1 \cos \Theta - n_2 \sin \Theta \cos \beta| \left[n_1 n_2 \cos^2 \Theta \right. \\ \left. + \frac{n_1^2}{2} \cos \beta \sin 2\Theta - \frac{n_2^2}{2} \cos \beta \sin 2\Theta \right. \\ \left. - n_1 n_2 \sin^2 \Theta \cos^2 \beta \right], \quad (10)$$

$$Q_{e2} = -\frac{4l_1}{\lambda}|n_1 \cos \Theta - n_2 \sin \Theta \cos \beta|[n_1^2 \cos \beta \cos^2 \Theta \\ - \frac{n_1 n_2}{2} \cos^2 \beta \sin 2\Theta - \frac{n_1 n_2}{2} \sin 2\Theta + n_2^2 \cos \beta \sin^2 \Theta], \quad (11)$$

² In our model, the only purpose of the existence of the pole is to minimize the effects of shadowing of the oblate grain core by the mirror.

$$Q_{e3} = -\frac{4l_1}{\lambda}|n_1 \cos \Theta - n_2 \sin \Theta \cos \beta|[n_1 \sin \beta[n_1 \cos \Theta \\ - n_2 \cos \beta \sin \Theta]]. \quad (12)$$

For $\Theta = 0, \pi$, the RAT components for the mirror are

$$Q_{e1} = \frac{4l_1 n_1^2 n_2}{\lambda}, \quad (13)$$

$$Q_{e2} = -\frac{4l_1 n_1^3}{\lambda} \cos \beta, \quad (14)$$

$$Q_{e3} = -\frac{4l_1 n_1^3}{\lambda} \sin \beta. \quad (15)$$

Equations (13)–(15) reveal that Q_{e1} does not depend on β , but Q_{e2}, Q_{e3} are periodic functions of β . As a result, when averaging over the rotation angle β from 0 to 2π , Q_{e2}, Q_{e3} vanish for $\Theta = 0, \pi$ (see a proof based on more general symmetry considerations in Section 4.2).

For arbitrary Θ , assuming that the rotation of the grain around the shortest axis is very fast, we can average RATs over β from 0 to 2π . The resulting RAT components are given by

$$Q_{e1} = \frac{4\pi l_1 n_1 n_2}{\lambda} (3 \cos^2 \Theta - 1) f(\Theta, \alpha), \quad (16)$$

$$Q_{e2} = \frac{4\pi l_1 n_1 n_2}{\lambda} \sin 2\Theta g(\Theta, \alpha), \quad (17)$$

$$Q_{e3} = 0, \quad (18)$$

where $f(\Theta, \alpha), g(\Theta, \alpha)$ are fitting functions depending on Θ, α which characterize the influence of variation of cross-section on RATs. The analytical approximations for them are given in Appendix B. Note that the dependence on l_1 arises in equations (16) and (17) due to the assumption $\lambda \ll l_1$. In the opposite limit we expect λ to act as an arm for torques and therefore no dependences of the RAT efficiencies Q_{e1}, Q_{e2} on l_1/λ to exist.

3.3 AMO: RATs' properties

For the sake of simplicity, for the rest of the paper, apart from the Appendices B2 and B3, we consider AMO for a single value of angle $\alpha = \pi/4$. Combining RATs produced by the reflecting oblate spheroid (see equations 4–6), and RATs induced by the reflecting mirror (see equations 16–18), for $\alpha = \pi/4$ AMO has the following components

$$Q_{e1} = \frac{4\pi l_1 n_1 n_2}{\lambda} (3 \cos^2 \Theta - 1) f(\Theta, \pi/4), \quad (19)$$

$$Q_{e2} = \frac{4\pi l_1 n_1 n_2}{\lambda} \sin 2\Theta g(\Theta, \pi/4), \quad (20)$$

$$Q_{e3} = \frac{2ea(s^2 - 1)}{\lambda} K(\Theta, e) \sin 2\Theta, \quad (21)$$

where the analytical and numerical fitting functions $f(\Theta, \pi/4)$ and $g(\Theta, \pi/4)$ are shown in Figs B1 and B2, respectively.

However, as we see further, Q_{e3} does not affect the alignment apart from inducing the precession. To roughly estimate the latter, one does not need to know the exact form of $K(\Theta, e)$ (see Section 6).

Equation (19) reveals clearly that Q_{e1} is symmetric, while equation (20) shows that Q_{e2} is asymmetric. In addition, Q_{e2} is zero for

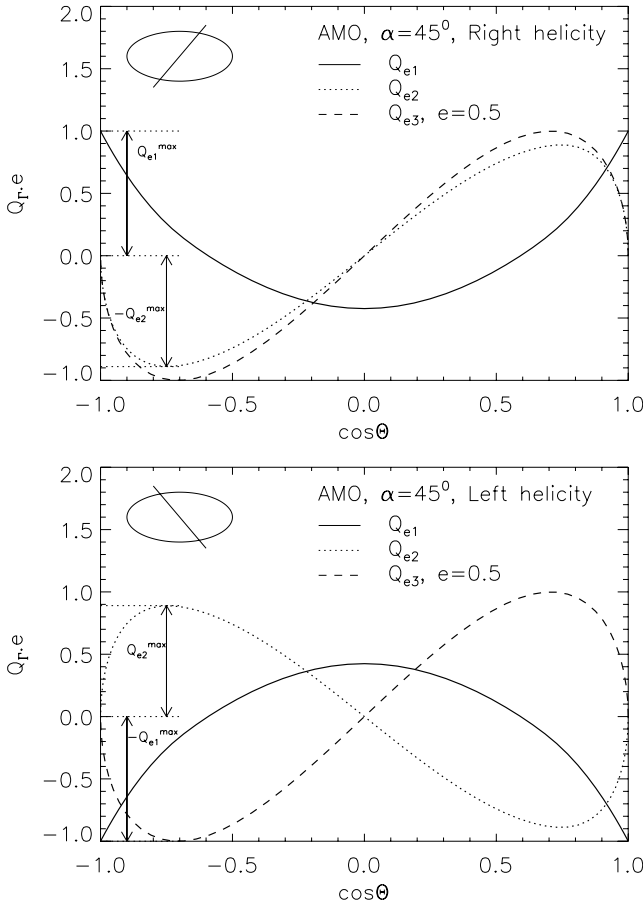


Figure 3. The components of RAT normalized over the maximum of $|Q_{e1}|$ as a function of Θ for right-handed (upper panel) and left-handed (lower panel) models of AMO. The helicity change is obtained by twisting the mirror by $\pi/2$. The maximum of Q_{e3} is also normalized to be equal to Q_{e1}^{\max} . Figures exhibit zeros of Q_{e2} and symmetries of RATs that we study for irregular grains using DDSCAT in Section 4.

$\Theta = 0, \pi$ and $\pi/2$, that is, when the maximal inertia axis \mathbf{a}_1 is parallel or perpendicular to the light direction (see also Fig. 3).

In particular, two first components, Q_{e1}, Q_{e2} depend on the product of projections of the normal vector, that is, $n_1 n_2$, which suggests us to define the helicity of a grain. A grain of *right-handed* helicity is defined so that, when the maximal inertia axis \mathbf{a}_1 is parallel to the radiation beam, it can rotate in clockwise sense around the radiation beam; a grain has *left-handed* helicity if it rotates anti-clockwise around the radiation beam. With these definitions, we see from equations (19) and (20) that the grain with right-handed helicity corresponds to the mirror being oriented so that $n_1 n_2 > 0$, and $n_1 n_2 < 0$ for the grain with left-handed helicity. It is straightforward to change the grain helicity from right- to left-hand side by a rotation of the mirror over an angle of $\pi/2$. Thus, grains with left- and right-hand side helicity are mirror symmetric, as expected. Naturally, the helicity of a spheroid is zero.

Fig. 3 shows components of RAT normalized over the maximum of $|Q_{e1}|$, so that they exhibit the functional dependence of RATs on Θ . Since Q_{e3} arises from the reflecting spheroid, not subject to the mirror size, in order for AMO to be self-consistent, we normalize Q_{e3} so that $Q_{e3}^{\max} = Q_{e1}^{\max}$. It is evident from examining the upper and lower panels of Fig. 3 that the transition from left- to right-handed grains induces a simultaneous change of the both Q_{e1} and

Q_{e2} components. This can be easily understood based on the fact that both Q_{e1} and Q_{e2} depend on the product $n_1 n_2$, which defines the helicity of grain. Therefore, as the helicity changes, that is, $n_1 n_2$ reverses the sign, Q_{e1}, Q_{e2} change synchronically. We shall see that this property is also present for arbitrarily chosen irregular grains that we study numerically in Section 4. Fig. 3 also shows clearly that the third component Q_{e3} that arises from the spheroidal body of the grain does not change as the grain gets the opposite helicity. This is exactly what we expect from a spheroid.

4 RATs: AMO VERSUS IRREGULAR GRAINS

We justify AMO's utility by finding the correspondence of the functional form obtained for the torques that our toy model experiences with those exerted on actual irregular grains. We start with finding generic properties of RATs for irregular grains using general symmetry considerations and follow further with numerical calculations.

4.1 Symmetry considerations for RATs

Here we show that some properties of RATs follow from general considerations based on the analysis of symmetries. For instance, we have observed that for AMO Q_{e2} and Q_{e3} become zero after β -averaging at points $\Theta = 0$ and π , while Q_{e1} does not depend on β . This property is valid for arbitrarily shaped grains. Indeed, when Θ is either 0 or π the radiation direction presents the axis of symmetry. It is obvious, therefore that changes of β cannot change the RAT component along the radiation direction (i.e. does not change Q_{e1}), while any perpendicular component of RAT (i.e. both Q_{e2} and Q_{e3}), should vanish as the result of β -averaging.³

Further on, we discuss the properties of β -averaged RATs. We can observe that similar to the case of AMO, the component of RATs Q_{e1} for irregular grains is symmetric with respect to $\Theta \rightarrow \pi - \Theta$ change (see Fig. 6). This symmetry is not exact, but it gets better for grains for which mutual shadowing of dipoles gets less. The symmetry of Q_{e1} ensures that the torque along \mathbf{k} has the same sign and similar magnitude when the grain flips over. At the same time the RAT component Q_{e2} is antisymmetric (see Fig. 6), it changes the sign for a transformation $\pi - \Theta$. This also corresponds to AMO. Similarly to Q_{e3} the symmetry of Q_{e1} is only approximate.

4.2 Zero-points of Q_{e2} at $\Theta = \pi/2$

For AMO, according to equation (21), Q_{e2} is equal to zero for $\Theta = \pi/2$. A similar property also exists for irregular grains, as obviously seen in Figs 6 and 7. There it is shown that when the maximal inertia axis is perpendicular to the radiation direction, the magnitude of Q_{e2} is very small. This can be explained in terms of the interaction of the electric dipoles with the electric field vector of radiation as follows: the interaction between electric field and electric dipoles induces their rotation around \mathbf{e}_2 to emit circularly polarized photons. However, since \mathbf{a}_1 is perpendicular to \mathbf{k} , the electric field is only able to induce the rotation of the electric dipoles in a plane containing \mathbf{e}_2 . As a result, the torque component vanishes. Quantitatively, according to equation (C5) (see Appendix C), it follows that, when

³ In fact, these considerations prove not only the zero values of Q_{e2} and Q_{e3} but also their periodicity as a function of β .

$\Theta = 90^\circ$, we have

$$\mathbf{Q}_{\text{abs}} \cdot \mathbf{e}_2 \sim k \cos \beta \operatorname{Re} \sum_j [p_j E_{\text{inc}}] e^{ikx_j}. \quad (22)$$

Since $x_j = r \sin \alpha \sin \beta$, it follows

$$\mathbf{Q}_{\text{abs}} \cdot \mathbf{e}_2 \sim \sum_j \cos \beta \cos(A \sin \beta) [p_j E_{\text{inc}}], \quad (23)$$

where the term $[p_j E_{\text{inc}}]$ is a function that is independent of β . It is obvious that $\mathbf{Q}_{\text{abs}} \cdot \mathbf{e}_2$ is a function of β which is zero when averaging is performed for β over $[0, 2\pi]$. We calculated $\mathbf{Q}_{\text{abs}} \cdot \mathbf{e}_2$ for different λ/a and grain shapes, and found that Q_{e2} is indeed close to zero at $\cos \Theta = 0$, which is consistent with our analytical expectation.

4.3 DDSCAT calculations

Fig. 4 presents the test grain shapes that we have calculated RATs for using DDSCAT. Parameters for calculations are given in Table 1. Shapes 1, 2 and 3 have been used in DW97. We added to them shapes 4 and 5. In addition, we created a mirror symmetric shape of shape 1, namely, shape 1* and provided the DDSCAT calculations for a spheroidal grain (see more details in Table 1). We adopt dielectric functions for astronomical silicate in which a feature in the ultra-violet is removed (see DW97; Weingartner & Draine 2001; Cho & Lazarian 2005).

We discussed for AMO that the sign of helicity can be changed by taking the mirror image of the grain. We performed a similar procedure to the irregular grains and obtained results similar to the ones obtained for AMO (see Figs 7 and 8).

Note that we observe that Q_{e1} and Q_{e2} change synchronously when we calculate torques for a mirror image of a grain. We see that the shape 1 has one type of helicity, while shapes 4, 5 and mirror symmetric image of shape 1, that is, shape 1*, have another type of helicity.

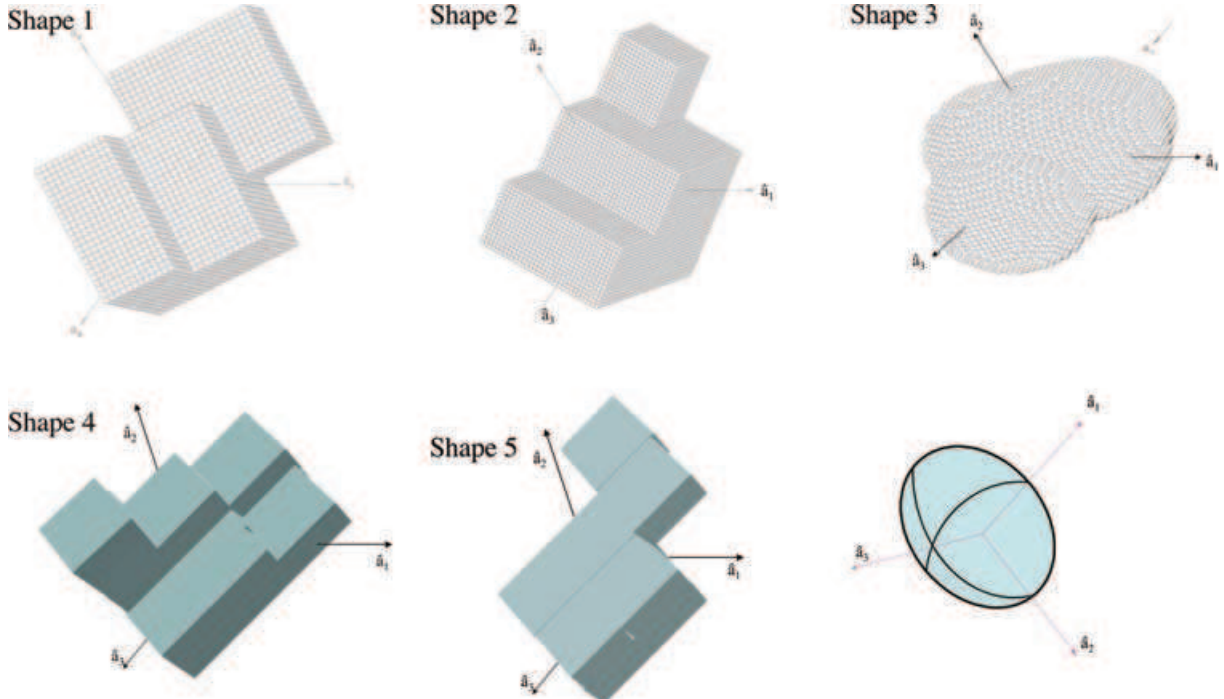


Figure 4. Geometry of grains under study: shapes 1–3 are similar to those of DW97, shapes 4 and 5 are created from 15 and 11 cubic blocks, respectively, and an ellipsoidal shape.

Table 1. Grain shapes and parameters for calculation of RATs.

Grain shapes	Dipole #	Size (μm)	Wavelength (μm)	Helicity
Shape 1	832000	0.05–0.2	ISRF	Right-handed
Shape 1*	53248	0.2	1.2	Left-handed
Shape 2	45056	0.2	ISRF	Left-handed
Shape 3	102570	0.2	ISRF	Left-handed
Shape 4	15000	0.2	1.2	Left-handed
Shape 5	11000	0.2	1.2	Left-handed
Hollow 1	832000	1.0	0.1	Right-handed

For all calculations here, we adopt the dielectric function for astronomical silicate.

Fig. 5 provides a comparison of normalized RATs between AMO and DDSCAT calculations performed for two irregular grains induced by monochromatic radiation field of $\lambda = 0.2 \mu\text{m}$ (see more in Section 4.4). It can be seen that they possess the same symmetric properties as well as zero-points. Also, the functional form of normalized Q_{e1} and Q_{e2} calculated for the irregular grains and AMO are remarkably similar, in particular for the Q_{e2} component. Typically, the RAT components for shape 2 are similar to those of AMO with $Q_{e1}^{\max}/Q_{e2}^{\max} = 1$ ratio, while RATs of shape 4 are similar to those of AMO with $Q_{e1}^{\max}/Q_{e2}^{\max} = 0.78$. Hence, by changing the ratio of amplitudes of the RAT components for AMO, we can obtain analytical expressions of RATs for a number of irregular grains. To have RATs appropriate to irregular grains, it is necessary to use DDSCAT to estimate the magnitude of RATs. Combining functional forms from AMO and magnitude from DDSCAT, we can obtain analytical approximate expressions for RATs components of irregular grains. Note that in Figs 3 and 5, we normalized RATs over $|Q_{e1}^{\max}| = |Q_{e1}(\Theta = 0)|$, so Q_{e1}^{\max} is the same for all realizations of AMO and the irregular grains. It is easy to see that with this choice, AMO reproduces very well Q_{e2} for irregular grains, but gets

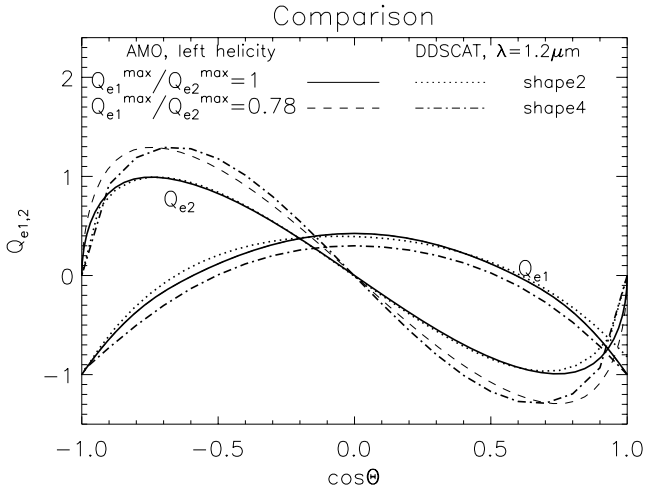


Figure 5. The comparison of RATs normalized over the maximum of $|Q_{e1}|$ between AMO (the left-handed grain) and DDSCAT (for shapes 2 and 4 and monochromatic radiation of $\lambda = 1.2 \mu\text{m}$). Solid and dashed lines show normalized RATs corresponding to $Q_{e1}^{\max}/Q_{e2}^{\max} = 0.78$ and 1 in which the functional forms are obtained from the analytical approximation given by equations (19) and (20) with tabulated functions f, g . Dot and dash-dotted lines show normalized RATs for shapes 2 and 4, respectively.

Q_{e1} , which is a bit larger at $\cos \Theta = 0$ ($\Theta = \pi/2$) than that for irregular grains. Potentially, this may mean that more appropriate parametrization should include Q_{e1}^{\max} , which is not defined as Q_{e1} at $|\cos \Theta| = 1$ ($\Theta = 0$ or π) as we do in this paper, but, for instance, the amplitude value of Q_{e1} , which is $|Q_{e1}(\Theta=0)| + |Q_{e1}(\Theta=\pi/2)|$. We feel, however, that our present parametrization has the advantage of simplicity and is sufficiently accurate.

4.4 Parameter study

Above we compared the properties of RATs in AMO with those obtained numerically from DDSCAT for a few chosen grain shapes and radiation spectra. To see how general our numerical results are, we attempt a limited parameter study, namely, we study how the properties of RATs vary with the spectrum of the incident radiation for different grain shapes. One can view the AMO formulae as a *physically motivated* fit to RATs acting on astrophysical grain with $a_{\text{eff}}/\lambda < 1$. The parameter study is intended to find out how good is this fit.

Fig. 7 shows Q_{e1} and Q_{e2} for shape 1 produced by different radiation fields. There the upper panel show that when monochromatic radiation fields of λ/a_{eff} increases, the symmetry of Q_{e1} and zeros of Q_{e2} do not change. However, their amplitude decreases. In addition, the symmetric property of Q_{e1} and zeros of Q_{e2} also remain unchanged when being averaged over different radiation spectrum (see the lower panel in Fig. 7).

Now let consider RAT properties for different irregular grains. The upper panel in Fig. 8 shows RATs for different shapes: shape 1* which is a mirror symmetric copy of shape 1, and shapes 4 and 5 are built from 15 and 11 cubic blocks, respectively.

We also see clearly that Q_{e1} exhibits the symmetry, and Q_{e2} exhibits the asymmetry that we have already seen with AMO and other grain shapes.

From Figs 7 and 8, it follows that the form of Q_{e1}, Q_{e2} for shape 1 is mirror symmetric to the corresponding RAT components applied to shape 1*. This mirror symmetry is also evident when we compare

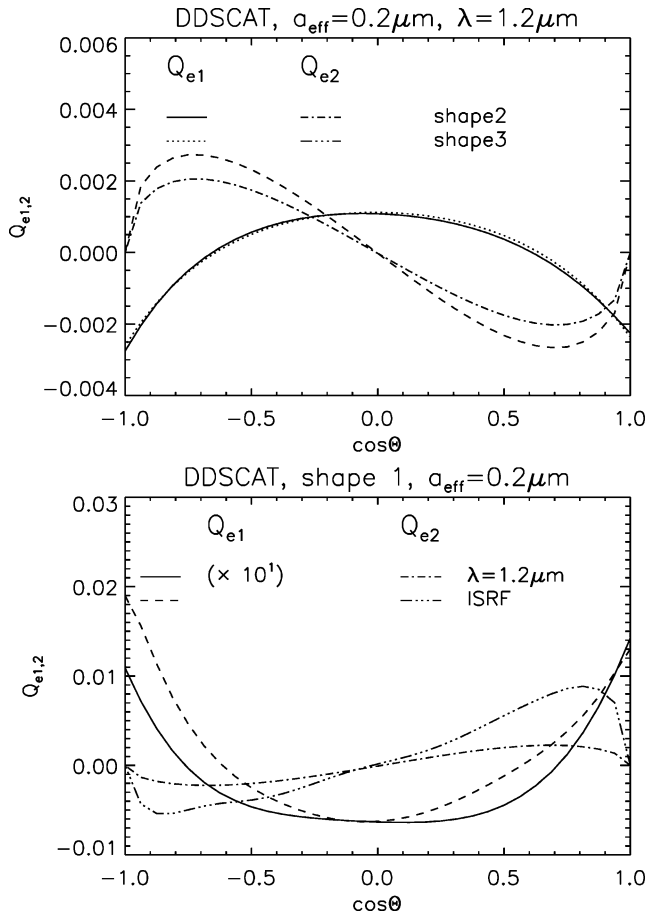


Figure 6. Q_{e1} and Q_{e2} for grains of left-handed (upper panel) and right-handed (lower panel) helicity. The symmetry of Q_{e1} with the transformation $\pi - \Theta$ is clearly seen for all grain shapes. Q_{e2} is antisymmetric with respect to the same transformation $\pi - \Theta$. A similarity with the torques produced by AMO is evident (see also Fig. 5).

Q_{e1}, Q_{e2} with those of shapes 4, 5 (see Fig. 4). This implies, similar to AMO, irregular grains may be of right- and left-handed helicities. A comparison between Figs 6, 7 (upper panel) and 8 (upper panel) shows that shapes 1*, 2, 3, 4, 5 are of left-handed helicity, while shape 1 is of right-handed helicity. Note that Fig. 7 (lower panel) clearly shows that the helicity is independent of wavelength and is an intrinsic attribute of grains which is associated to their shape. Especially, we can obtain a grain with the opposite helicity by performing a mirror symmetric transformation, which is illustrated by AMO in Fig. 3. We remind the reader that the correspondence between Q_{e1} and Q_{e2} for AMO and shapes 2 and 4 is illustrated by Fig. 5.

For the third RAT component Q_{e3} , it exhibits analogous properties with Q_{e2} obviously seen in the lower panel in Fig. 8. Also, for an axisymmetric shape, that is, spheroid, Q_{e3} is still significant. Note that its functional form obtained by DDSCAT is very consistent with that predicted by AMO in Section 3 (see dot and dot-dashed line in Fig. 8). Furthermore, we see that it has similar forms for left-handed (shapes 2 and 3) and right-handed (shape 1) helical grains (see Fig. 8, lower panel). While the dependences of Q_{e1} and Q_{e2} undergo a transformation when shape 1 is substituted by shape 1*, having the opposite helicity, a comparison of lower and upper panels of Fig. 8 shows that the shape of Q_{e3} component stays the same. This is expected, as Q_{e3} does not depend on the helicity of grains.

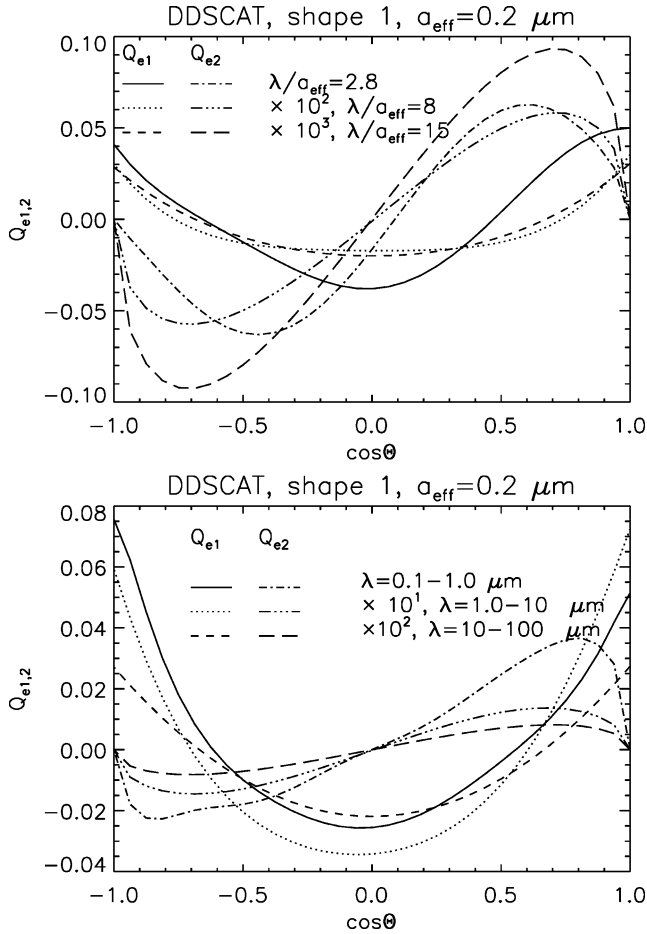


Figure 7. RATs for shape 1 corresponding to various λ/a_{eff} (upper panel) and RATs averaged over a range of wavelengths (lower panel).

Also, the Q_{e3} component has zeros at $\Theta = 0, \pi$, similar to Q_{e2} (see the lower panel in Fig. 8). However, the antisymmetry of Q_{e3} is less prominent than for Q_{e2} .

As we will see that the ratio $Q_{e1}^{\max}/Q_{e2}^{\max}$ is an important parameter that determines the existence of high- J attractor points. For irregular grains, this ratio is a function of the ratio of wavelength to grain size, as shown in Fig. 9 for three irregular grains. The peak of $Q_{e1}^{\max}, Q_{e2}^{\max}$ is different for different shapes. The form of the curve for sufficiently large ratios of λ/a_{eff} can be approximated as $10^{a_{\text{eff}}/\lambda}$. This dependence can be used to reduce the number of DDSCAT calculations necessary for determining the alignment for arbitrary radiation fields.

In general, we observe strong similarities between the plots of RAT components obtained for very different grains. Thus we can expect that the RAT alignment should be similar for such grains. We will discuss the alignment for AMO and irregular grains in Sections 6 and 7.

4.5 RATs: comparison with AMO

The actual grains are not perfectly reflecting particles and the scattering that they induce cannot be described by geometric optics that we employ for AMO. Therefore the justification of the AMO utility can be obtained via a comparison of the functional form of the torque components obtained for irregular grains with the AMO predictions. Naturally, one should not expect to see the amplitudes of

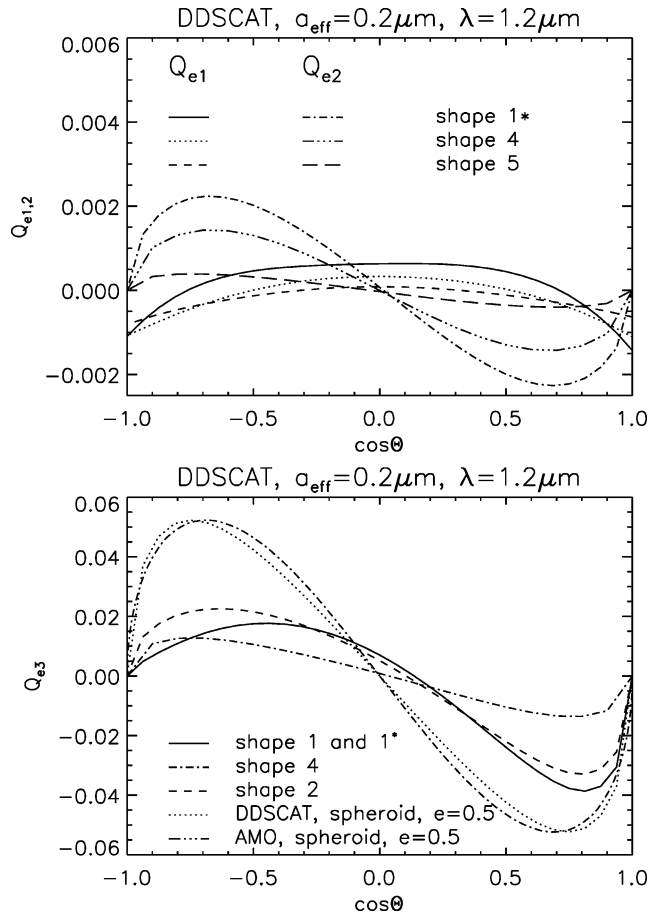


Figure 8. Upper panel: RATs for different grain shapes. Shape 1* corresponds to mirror symmetric image of shape 1. Symmetric features of Q_{e1} and zeros of Q_{e2} are clearly found. Lower panel: The third component of RATs Q_{e3} for different shapes are shown together with that of a spheroid with $e = 0.5$ predicted by AMO. An analogy exists between the zeros of Q_{e2} and Q_{e3} . Also, the shape of Q_{e3} is not affected by the change of grain helicity.

the torques to be the same. Therefore the comparison should be done for the normalized torque components. However, we preserve the ratio of the components.

Naturally, our sample of RATs acting on grains studied with DDSCAT is limited. It includes several grain sizes. For instance, for shape 1, we studied for grain sizes of 0.05, 0.08, 0.1 and 0.2 μm . For other shapes, the size $a_{\text{eff}} = 0.2 \mu\text{m}$ is studied, except the hollow shape 1 with $a_{\text{eff}} = 1 \mu\text{m}$. We calculated RATs for the entire spectrum of ISRF corresponding to 21 wavelengths in the range $\lambda = 0.1$ to $100 \mu\text{m}$, for shapes 1, 2 and 3, and the monochromatic radiation with $\lambda = 1.2 \mu\text{m}$ for other shapes. This provides us with RATs calculated for 130 realizations of grains and radiation fields.⁴ This makes it the most extensive sample of RATs studied numerically. It is obvious that in our paper we cannot present plots of the RATs for all the realizations that we calculated (see e.g. Fig. 5). A quantitative comparison based on the deviation testing for normalized RATs of all realizations and AMO will be presented below.

We show in Fig. 9 that, for irregular grains, the relative amplitude of Q_{e1} versus Q_{e2} changes both with the grain shape and

⁴ Each realization corresponds to a given grain size and a given wavelength.

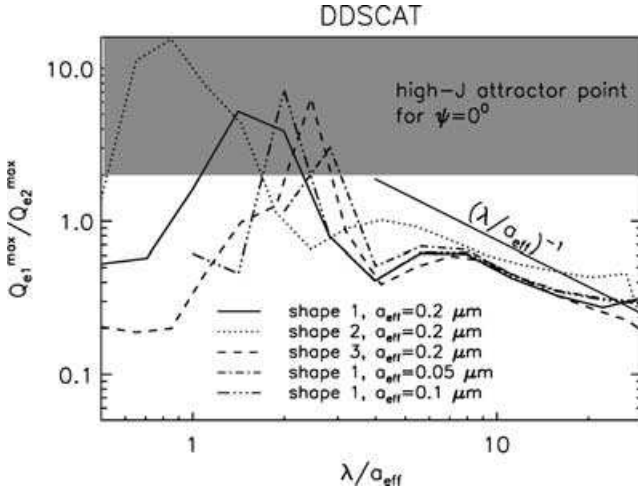


Figure 9. Ratio of Q_{e1}^{\max} , Q_{e2}^{\max} as function of wavelength to grain size λ/a_{eff} for different grain shapes and sizes. The shaded region corresponds to the parameter space in which the high- J attractor point is present for the alignment with respect to the beam direction (see Section 6).

wavelengths. However, our studies in this paper show that the functional form of the RAT components for all the cases we studied is still well represented by AMO (with different ratios of $Q_{e1}^{\max}/Q_{e2}^{\max}$, e.g. Fig. 5). In other words, while DDSCAT studies of alignment for grains of a few chosen shapes cannot reveal the generic properties of the RAT alignment, revealing the correspondence of the functional dependences of the torques between irregular grains and AMO provides a deep insight into the alignment.

Since we are only interested in the functional forms of RATs, let us introduce the mean deviation over Θ for the components Q_{e1} and Q_{e2} as follows:

$$\langle \Delta^2 \rangle(Q_{ei}) = \frac{1}{\pi(Q_{ei}^{\max})^2} \int_0^\pi [Q_{ei}^{\text{DDSCAT}}(\Theta) - Q_{ei}^{\text{AMO}}(\Theta)]^2 d\Theta, \quad (24)$$

where $Q_{ei}^{\text{DDSCAT}}(\Theta)$ denotes $Q_{e1}(\Theta), Q_{e2}(\Theta)$ for irregular grains, $Q_{ei}^{\text{AMO}}(\Theta)$ denotes the torque components for AMO in which the relative magnitudes are rescaled to have the same ratio $Q_{e1}^{\max}/Q_{e2}^{\max}$ with each realization of irregular grains.⁵ In equation (24), Q_{ei}^{\max} is the maximum of Q_{e1} and Q_{e2} , which is chosen the same for both AMO and irregular grains.

We perform $\langle \Delta^2 \rangle$ testing for our sample consisting of 130 realizations of irregular grain shape, size and wavelength. To see the correspondence of AMO with different grain shape, size and wavelength, in Fig. 10 we show $\langle \Delta^2 \rangle$ as a function of λ/a_{eff} .

Fig. 10 (upper panel) shows a good correspondence for the component Q_{e1} between irregular grains and AMO. The value of $\langle \Delta^2 \rangle$ ranges from as small as 10^{-3} to 2×10^{-1} . In addition, Fig. 10 (lower panel) shows an extremely good correspondence for the component Q_{e2} between all cases of irregular grains and AMO. The values for different sizes of shape 1 are nearly the same, but they change with grain shapes. For instance, shapes 2 and 3 have the better correspondence with AMO than shape 1. The corresponding value of $\langle \Delta^2 \rangle$ is about 2×10^{-2} and 3×10^{-2} for shapes 2, 3 and 1, respectively (see Fig. 10, lower panel). For both components and all

⁵ We note again that, throughout this paper, apart from Appendices B2 and B3, the functional forms of RAT components for AMO corresponds to AMO with $\alpha = 45^\circ$, and the ratio of their maximum is adjustable.

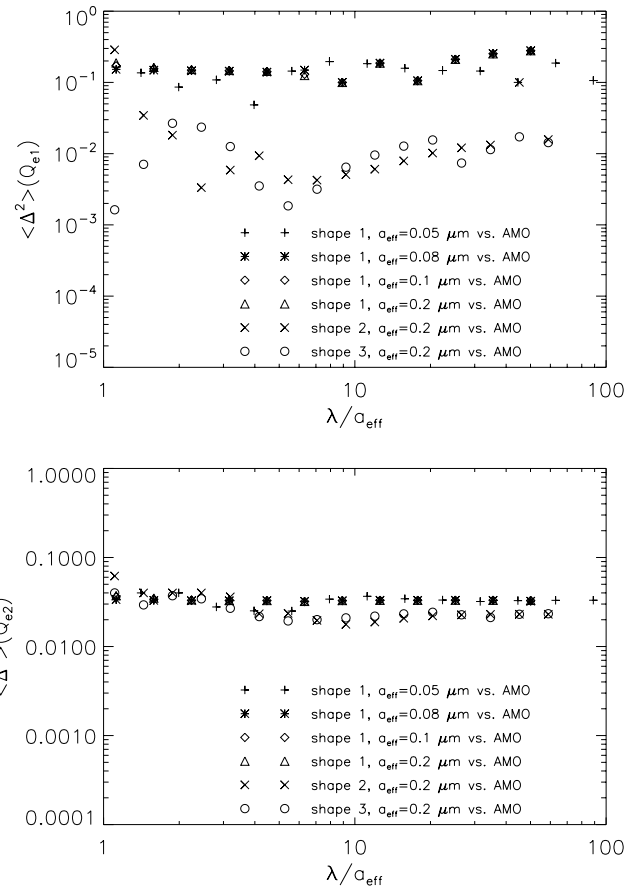


Figure 10. $\langle \Delta^2 \rangle$ testing as function of λ/a_{eff} for normalized Q_{e1} (upper panel) and Q_{e2} (lower panel) between irregular grain shapes and sizes with AMO.

grain shapes and sizes, $\langle \Delta^2 \rangle$ do not change so much with respect to wavelength of radiation field for $\lambda/a_{\text{eff}} > 3$. However, it increases when λ/a_{eff} decreases. It is clear that the smaller $\langle \Delta^2 \rangle$ is, the better correspondence is. Therefore, the observed worse correspondence for the range $\lambda/a_{\text{eff}} < 3$ can be easily explained in terms of the RAT properties for irregular grains. In fact, following Fig. 7 (upper panel), it can be seen that the components Q_{e1}, Q_{e2} for $\lambda/a_{\text{eff}} = 2.8$ are indeed less symmetric than those for $\lambda/a_{\text{eff}} = 8$ and 15. In other words, the symmetry of RATs decreases towards small λ/a_{eff} .

Note that lower values of $\langle \Delta^2 \rangle$ can be obtained for small λ/a_{eff} ratios, if Q_{e1} is considered separately for Θ within ranges $[\pi, \pi/2]$ and $[\pi/2, 0]$. This procedure can compensate for the differences in the surface characteristics on the side of the grain towards the light direction and opposite to it. As we discuss in Section 5 such differences are natural for less idealized models of helical grains. We do not pursue this approach within this paper, preferring a simple model with a reasonable fit to a more complex model that can provide a better fit. Nevertheless, in future, dealing with particular cases, for example, graphite grains, the approach of considering different ranges of Θ may prove advantageous.

Therefore, our quantitative comparison of the RATs based on $\langle \Delta^2 \rangle$ for irregular grains with AMO implies that the functional form of RATs obtained in the limit $\lambda \ll a_{\text{eff}}$ (AMO) is also valid for RATs in the limit $\lambda \sim a_{\text{eff}}$ and $\lambda > a_{\text{eff}}$ (for irregular grains). This allows us to use AMO as a representative model for describing RATs of realistic astrophysical grains, for example, study grain alignment using AMO.

5 AMO: DEFINITION AND GENERALIZATIONS

Our studies above show that the model of AMO corresponding to $\alpha = \pi/4$ corresponds well to the results of numerical calculations of RATs, provided that we treat $Q_{e1}^{\max}/Q_{e2}^{\max}$ as an adjustable parameter. Indeed, while we show in Appendix B that this ratio changes with α , the range of the ratio variations is lower than for irregular grains (cf. Figs B6 and 9).

This adjustment is natural, as we do not really expect the scattering by irregular dielectric grains to be entirely equivalent to scattering by mirrors of our toy model of a grain.

Our analytical studies are based on AMO, which provides a simple model of RATs. If necessary, AMO can be trivially generalized by adding additional mirrors to grain surface and accounting for a partial shadowing of the mirrors by the spheroidal grain body. In addition, one can consider not perfectly reflective models, but models with refractive grain body and also refractive plate instead of a mirror. This allows us to vary AMO's properties.

An arbitrary attachment of mirrors may make Q_{e1} less symmetric. For instance, a grain shown in the upper panel of Fig. 11 has a mirror attached to one of its surfaces. Naturally, turning this surface towards the beam of radiation produces torques that are different from the case when the mirror is hidden by the elliptical body of the grain.

In addition, the adopted AMO does not account for torques arising from absorption. If, however, one adds to the spheroidal grain a one-dimensional damped oscillator with the axis at an angle to the spheroid symmetry axis (see the lower panel in Fig. 11), such a grain would have a non-zero torque component Q_{e2} arising from light absorption. Note that just adding absorbing component to one of the surfaces of the reflecting mirror would distort the symmetry of torques Q_{e1} , which would correspond to RATs calculated for irregular grains for small λ/a_{eff} ratio.

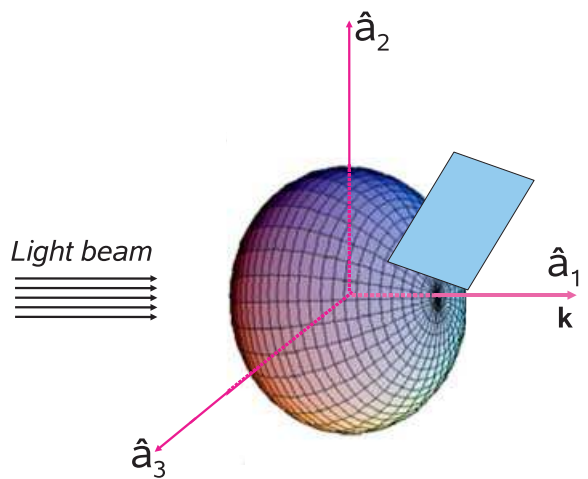
While adding such effects could provide us with better fits of RATs obtained numerically for particular shapes, this would increase the complexity of our model. We do not pursue this path here, therefore. However, we can see that in some cases, for example, dealing with highly absorbing grains (e.g. graphite grains), one may have to make the corresponding AMO more sophisticated.

Note that some modifications do not require making the model more complex. Historically, spheroidal grains were used to demonstrate alignment. However, for demonstrating the effects of H₂ torques Purcell (1979) considered a 'brick-shaped' grain. If we want to study the effects of H₂ torques for AMO, it is natural to consider not a 'spheroid with a wing', as we have done in this paper, but a 'brick with a wing'. In terms of AMO this would not change the properties, apart from the value of Q_{e3} torque, which is not important for the alignment, anyhow.

Intentionally, our AMO is based on an intuitive macroscopic model. Microscopic models based on the analytical treatment of RATs are possible also. For instance, light scattering by optically active (chiral) sphere was analytically studied by Bohren (1974). The author derived analytical solutions for scattering matrix. Due to the optical activeness, such spherical grain can produce RATs. This model would correspond to the Dolginov (1972) suggestion of quartz grains being spun up and aligned by RATs.

Another possible generalization of AMO is to consider that its inertial properties are given not by a spheroid but by a triaxial ellipsoid. An important generalization of AMO is to consider that its inertial properties are given not by a spheroid but by a triaxial ellipsoid. We expect such changes to result in important differences in dynamics during periods of crossovers, while not affecting the

Spheroid + a shadowed mirror



A damped oscillator and a spheroid

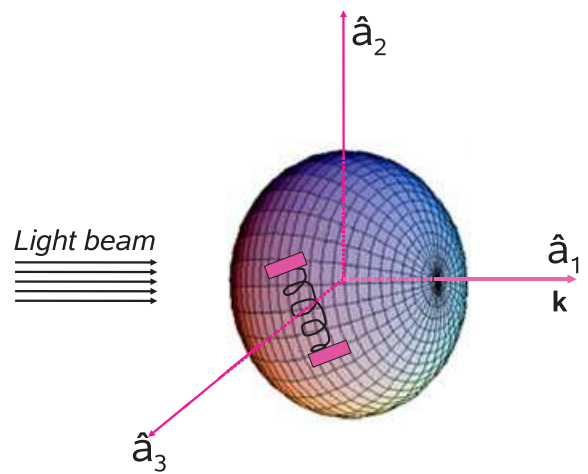


Figure 11. Models of a grain shape consisting of a mirror shadowed partially by the oblate spheroid (upper panel) and a partially damped oscillator attached to the oblate spheroid (lower panel).

rest of the grain phase trajectories. The corresponding effects together with the modification of the inertial properties of AMO are considered in Hoang & Lazarian (2007).

All in all, while it is rather easy to make AMO more sophisticated and provide a better fit for RATs within different ranges of λ and a_{eff} , for the rest of the paper, we adopt a very simple model of AMO. This model provides a reasonable fit to generic properties of RATs acting on actual irregular grains. Thus studying grain alignment with AMO should provide insight into the alignment processes acting upon astrophysical grains.

6 ALIGNMENT WITH RESPECT TO LIGHT DIRECTION

While the earlier studies dealt with the alignment with respect to magnetic field, in this section we show that RATs can align grains on their own, without any influence of magnetic fields. In this case, the direction of radiation \mathbf{k} is the axis of alignment. As we further

discuss in Section 9.1 such alignment happens in the presence of magnetic field when the rate of precession induced by radiation is faster than the Larmor precession rate. Dealing with this simple case also prepares us for dealing with a more complicated case of alignment with respect to magnetic field in Section 7.

6.1 RATs: spin-up, alignment and precession

To understand the role of the RAT components, we calculate torques that spin up, align and induce grain precession. A RAT component that acts to spin up grains, H , is directed along $\hat{\mathbf{a}}_1$, the component that aligns grains, F , is directed along $\hat{\Theta}$ and RAT that causes precession, G , is along $\hat{\Phi}$. They are, respectively, given by (see DW97)

$$\begin{aligned} H(\Theta, \Phi) = & \mathcal{Q}_\Gamma \cdot \mathbf{e}_1(\Theta, \Phi) \cos \Theta + \mathcal{Q}_\Gamma \cdot \mathbf{e}_2(\Theta, \Phi) \sin \Theta \cos \Phi \\ & + \mathcal{Q}_\Gamma \cdot \mathbf{e}_3(\Theta, \Phi) \sin \Theta \sin \Phi, \end{aligned} \quad (25)$$

$$\begin{aligned} F(\Theta, \Phi) = & -\mathcal{Q}_\Gamma \cdot \mathbf{e}_1(\Theta, \Phi) \sin \Theta + \mathcal{Q}_\Gamma \cdot \mathbf{e}_2(\Theta, \Phi) \cos \Theta \cos \Phi \\ & + \mathcal{Q}_\Gamma \cdot \mathbf{e}_3(\Theta, \Phi) \cos \Theta \sin \Phi, \end{aligned} \quad (26)$$

$$G(\Theta, \Phi) = -\mathcal{Q}_\Gamma \cdot \mathbf{e}_2(\Theta, \Phi) \sin \Phi + \mathcal{Q}_\Gamma \cdot \mathbf{e}_3(\Theta, \Phi) \cos \Phi. \quad (27)$$

On the other hand, following equation (2), RATs at a precession angle Φ are given by

$$\mathcal{Q}_\Gamma \cdot \mathbf{e}_1(\Theta, \Phi) = \mathcal{Q}_{e1}(\Theta, 0), \quad (28)$$

$$\mathcal{Q}_\Gamma \cdot \mathbf{e}_2(\Theta, \Phi) = \mathcal{Q}_{e2}(\Theta, 0) \cos \Phi - \mathcal{Q}_{e3}(\Theta, 0) \sin \Phi, \quad (29)$$

$$\mathcal{Q}_\Gamma \cdot \mathbf{e}_3(\Theta, \Phi) = \mathcal{Q}_{e2}(\Theta, 0) \sin \Phi + \mathcal{Q}_{e3}(\Theta, 0) \cos \Phi. \quad (30)$$

Plugging the above equations into (25)–(27) we get

$$G(\Theta, \Phi) = \mathcal{Q}_{e3}(\Theta, 0), \quad (31)$$

$$H(\Theta, \Phi) = \mathcal{Q}_{e1}(\Theta, 0) \cos \Theta + \mathcal{Q}_{e2}(\Theta, 0) \sin \Theta, \quad (32)$$

$$F(\Theta, \Phi) = -\mathcal{Q}_{e1}(\Theta, 0) \sin \Theta + \mathcal{Q}_{e2}(\Theta, 0) \cos \Theta. \quad (33)$$

If for $G(\Theta, \Phi)$ we are mostly interested in its amplitude, the functional forms of $F(\Theta, \Phi)$ and $H(\Theta, \Phi)$ are essential for grain alignment. The problem is that $F(\Theta, \Phi)$ and $H(\Theta, \Phi)$ as well as their counterparts obtained in the presence of magnetic field (see equations 68 and 69), vary substantially from one grain to another. For AMO different grains correspond to different ratios $\mathcal{Q}_{e1}^{\max}/\mathcal{Q}_{e2}^{\max}$. As we mentioned in Sections 4.3 and 4.4, irregular grains are different in terms of RATs for the radiation of different wavelengths and different grain sizes. However, for both AMO and irregular grains, the generic properties of the RAT components (i.e. symmetry of \mathcal{Q}_{e1} , as well as the asymmetry and zeros of $\mathcal{Q}_{e2}, \mathcal{Q}_{e3}$) are always unchanged. Therefore, unlike \mathcal{Q}_{e1} and \mathcal{Q}_{e2} , the components $F(\Theta, \Phi)$ and $H(\Theta, \Phi)$ do not demonstrate a universal behaviour and play an auxiliary role in our study.

We see that the precessing torque depends only on the third component $\mathcal{Q}_{e3}(\Theta, 0)$, while the aligning and spinning torques are related to two first components, namely, $\mathcal{Q}_{e1}(\Theta, 0), \mathcal{Q}_{e2}(\Theta, 0)$. We note that the functions F, G, H are the functions of only variable Θ , in this case.

For AMO with $\alpha = 45^\circ$, substituting analytical expressions $f = f_{\pi/2}$ and g given by equations (B28) and (B31) into equations (16) and (17), we get

$$\mathcal{Q}_{e1}(\Theta, 0) = \frac{16l_1n_1n_2|n_2|}{3\lambda}(5 \cos^2 \Theta - 2), \quad (34)$$

$$\mathcal{Q}_{e2}(\Theta, 0) = \frac{40l_1n_1n_2|n_2|}{3\lambda} \sin 2\Theta(1.191 + 0.1382 \cos^2 \Theta). \quad (35)$$

Substituting equations (21), (34) and (35) into equations (31)–(33), and averaging over Φ we get

$$G(\Theta) = -\frac{2ea(1-s)}{\lambda} K(\Theta, e) \sin 2\Theta, \quad (36)$$

$$\begin{aligned} H(\Theta) = & \frac{8l_1n_1n_2|n_2|}{3\lambda} \cos \Theta[1 + 6.91 \sin^2 \Theta \\ & + \cos^2 \Theta(5 + 1.382 \sin^2 \Theta)], \end{aligned} \quad (37)$$

$$\begin{aligned} F(\Theta) = & \frac{8l_1n_1n_2|n_2|}{3\lambda} \sin \Theta[-1 + 6.91 \cos^2 \Theta \\ & + 1.382 \cos^4 \Theta + 5 \sin^2 \Theta]. \end{aligned} \quad (38)$$

6.2 Simplified treatment of crossovers

In general, the maximal inertia axis \mathbf{a}_1 of our model grain can precess about the vector of the angular momentum \mathbf{J} . In the present paper, however, for the sake of simplicity, we assume a perfect internal alignment, that is, $\mathbf{J} \parallel \mathbf{a}_1$. This assumption coincides with that in DW97 and can be justified by the high efficiency of the internal relaxation within a wobbling grain. This relaxation stems from the Barnett relaxation discovered by Purcell (1979) and/or nuclear relaxation introduced in LD99b. However, these relaxation processes provide a good coupling only when $J \gg J_{\text{th}} \approx (kT_d I_1)^{1/2}$ where T_d is the dust temperature, I_1 is the maximal moment of inertia of grain (Lazarian 1994), that is, when a grain rotates with suprathermal velocities. This condition is not satisfied as a grain approaches crossover points, that is, as $J \rightarrow J_{\text{th}}$.

We adopt below a simplified treatment of crossovers, which is different, however, from the treatment of crossovers in DW97. There it was assumed that $\mathbf{J} \parallel \mathbf{a}_1$ up to the moment of the angular velocity getting zero. After that DW97 assumed that \mathbf{J} changes its direction to the opposite, while the direction of \mathbf{a}_1 is preserved. Such a model of crossovers differs from the earlier work on crossovers, which suggests that, as the angular velocity goes to zero, the grain undergoes a flip, that is, \mathbf{J} preserves its direction, while the direction of \mathbf{a}_1 changes to the opposite (Spitzer & McGlynn 1979; Lazarian & Roberge 1997). Therefore, in what follows, we adopt a model in which $\mathbf{J} \parallel \mathbf{a}_1$ up to a crossover; at the crossover \mathbf{a}_1 flips, while the direction of \mathbf{J} is preserved. This makes the dynamics of grains very different from that in DW97.⁶ Although we accept that our model is not precise when $J \sim J_{\text{th}}$, we claim that our simplified model is ‘roughly true’. The latter point is justified for regular crossovers (i.e. crossovers without thermal fluctuations) in Section 8.

6.3 Stationary and singular points

6.3.1 Equations of motion

To find out whether grains can be aligned with respect to \mathbf{k} , we need to find stationary states for grain motion exerted by RATs. We start with equations of motion:

$$\frac{d\mathbf{J}}{dt} = M\mathbf{H}(\Theta) - \mathbf{J}, \quad (39)$$

⁶ We may mention parenthetically that the dynamics that we get has similarities to the dynamics of grains with thermal fluctuations accounted for, as in WD03. There, however, it was interpreted as a new effect related to thermal fluctuations.

Table 2. Physical parameters for diffuse ISM.

Definitions	Typical values
Gas density	$n = 30 \text{ cm}^{-3}$
Gas temperature	$T_{\text{gas}} = 100 \text{ K}$
Gas damping time	$t_{\text{gas}} = 4.6 \times 10^{12} \left(\frac{\hat{n}}{\hat{n} T_{\text{gas}}^{1/2}} \right) a_{-5} \text{ s}$
Dust temperature	$T_d = 20 \text{ K}$
Anisotropy degree	$\gamma = 0.1$
Grain size	$a_{\text{eff}} = 0.2 \mu\text{m}$
Mean wavelength	$\bar{\lambda} = 1.2 \mu\text{m}$
Mean density of ISRF	$u_{\text{rad}} = 8.64 \times 10^{-13} \text{ erg cm}^{-3}$

The normalized values that we also use are $\hat{T}_{\text{gas}} = T_{\text{gas}}/100 \text{ K}$, $\hat{n} = n/30 \text{ g cm}^{-3}$ and $a_{-5} = a_{\text{eff}}/10^{-5} \text{ cm}$, and normalized grain density $\hat{\rho} = \rho/3 \text{ g cm}^{-3}$.

$$\frac{d\Theta}{dt} = M \frac{F(\Theta)}{J}, \quad (40)$$

where time t and angular momentum J are scaled in the units of the gas damping time t_{gas} (see Table 2) and the thermal angular momentum $I_1 \omega_T$. Here I_1 is the maximal moment of inertia and $\omega_T = (kT_{\text{gas}}/I_1)^{1/2}$ is the thermal angular velocity with the gas temperature T_{gas} . In equations (39) and (40)

$$M = \frac{\gamma u_{\text{rad}} \lambda a_{\text{eff}}^2 t_{\text{gas}}}{2 I_1 \omega_T} \quad (41)$$

contains important parameters of the physical problem. There u_{rad} is the energy density of radiation field, λ is the wavelength. In the present paper, for our estimates, we use the values provided in Table 2 for ISM. It will be explicitly stated in case other values of these parameters are used.

6.3.2 Stationary points

The stationary point is determined by setting the equations of motion (39) and (40) equal to zero. This point may be an attractor or a repeller point. We remind the reader that for a stationary point to be an attractor point, it requires (see Appendix C)

$$\frac{dF(\Theta)}{H(\Theta)d\Theta} \Big|_{\Theta=\Theta_s} < 1, \quad (42)$$

$$H(\Theta) \frac{dF(\Theta)}{d\Theta} \Big|_{\Theta=\Theta_s} < F(\Theta) \frac{dH(\Theta)}{d\Theta} \Big|_{\Theta=\Theta_s}. \quad (43)$$

At the stationary points, $F(\Theta_s) = 0$, so equations (42) and (43) reduce to

$$\frac{dF(\Theta)}{d\Theta} \Big|_{\Theta=\Theta_s} < 0, \text{ for } H(\Theta_s) > 0, \quad (44)$$

and

$$\frac{dF(\Theta)}{d\Theta} \Big|_{\Theta=\Theta_s} > 0, \text{ for } H(\Theta_s) < 0. \quad (45)$$

Consider that initially a grain has the maximal inertia axis \mathbf{a}_1 parallel to \mathbf{k} , that is, $\Theta_0 = 0$, then $F(\Theta_0) = 0, H(\Theta_0) = Q_{e1}(\Theta_0)$. These assumptions are usually used to estimate the grain angular velocity induced by RATs (see DW97; Cho & Lazarian 2005). Therefore, the equations of motion become

$$\frac{d\Theta}{dt} = 0, \quad (46)$$

$$\frac{dJ}{dt} = M Q_{e1} - J. \quad (47)$$

Solutions for the above equations are easily found:

$$\Theta = 0, \quad (48)$$

$$J = M Q_{e1}(\Theta) + [J_0 - M Q_{e1}(\Theta_0)] e^{-t}, \quad (49)$$

where J_0 is the initial angular momentum of grains. Equation (49) shows that as $t \gg 1$, $J = M Q_{e1}(\Theta = 0)$. In other words, grains initially parallel to \mathbf{k} are spun up by RATs and aligned with \mathbf{k} at angular momentum $J_s = M Q_{e1}(\Theta_s = 0)$, regardless of its initial angular momentum J_0 . However, the particular point of phase trajectory map may not provide stable orientation of the grain, that is, may not be attractor points.⁷

For $\sin \Theta_0 \neq 0$, substituting $F(\Theta), H(\Theta)$ from equations (37) and (38) into equations (39) and (40), we obtain

$$\frac{dJ}{dt} = \frac{8l_1 n_1 n_2 |n_2|}{3\lambda} M \cos \Theta [1 + 6.91 \sin^2 \Theta + \cos^2 \Theta (5 + 1.382 \sin^2 \Theta)] - J, \quad (50)$$

$$\frac{d\Theta}{dt} = \frac{8l_1 n_1 n_2 |n_2| M}{3\lambda J} \sin \Theta [-1 + 6.91 \cos^2 \Theta + 1.382 \cos^4 \Theta + 5 \sin^2 \Theta]. \quad (51)$$

Hence, we can easily find a stationary point⁸:

$$\Theta_s = 0, \quad (52)$$

$$J_s = \frac{48l_1 n_1 n_2 |n_2| M}{3\lambda}. \quad (53)$$

From equations (37) and (38) we get

$$\frac{dF(\Theta)}{d\Theta} \Big|_{\Theta_s=0} = \frac{90.232 l_1 n_1 n_2 |n_2|}{3\lambda}, \quad (54)$$

and $H(\Theta_s = 0) > 0$. As a result, the stationary point $\Theta_s = 0$ is a repeller point.

In a general case, $F(\Theta), H(\Theta)$ are given by equations (32) and (33). Thus, substituting them into equations (44) and (45), we get a criteria for a stationary point Θ_s being an attractor point, namely,

$$\frac{-Q'_{e1} \sin \Theta_s + Q'_{e2} \cos \Theta_s}{Q_{e1} \cos \Theta_s + Q_{e2} \sin \Theta_s} < 1, \quad (55)$$

where $Q'_{e1} = dQ_{e1}/d\Theta, Q'_{e2} = dQ_{e2}/d\Theta$. However, our approximate formulae above catches the phenomenon correctly and we still get repeller points for $\Theta_s = 0$ with the exact expressions for AMO.

As the range for ratios of Q_{e1}/Q_{e2} for an arbitrarily chosen irregular grain may be different from AMO, for some irregular grains we still may have attractor points for $\Theta_s = 0$, as it is shown in Fig. 24 for shape 1 subjected to ISRF. There the relevant data corresponding to $\psi = 0$, as in this situation the direction of magnetic field and the light coincide and thus our considerations about the alignment with respect to \mathbf{k} are applicable.

⁷ The shaded area with diagonal lines in Fig. 24 corresponds to the existence of such points. We see that for many wavelengths the condition is not satisfied.

⁸ Another stationary point $\Theta = \pi, J < 0$ is forbidden since J cannot be negative. Note that the analysis in this section is applied for the right-handed helical grain, that is, $n_1 n_2 > 0$.

6.3.3 Singular points: crossovers

When $J = 0$, we have a singular point (see equation 40). In terms of our simplified equations it corresponds to a crossover. As we discussed earlier, a crossover is a period in which a grain spins down to the point that the component of angular momentum parallel to \mathbf{a}_1 gets zero. In the presence of strong internal relaxation that tends to align \mathbf{J} and \mathbf{a}_1 , this means that J should get small (Spitzer & McGlynn 1979). Our equations above are derived in the assumption of $\mathbf{J} \parallel \mathbf{a}_1$ and therefore cannot treat grain crossovers (cf. Sections 6 and 8). However, they can still trace the grain dynamics as the grain phase trajectory approaches the crossover and $J \rightarrow J_{\text{th}}$. Assuming that initial angular momentum of the grain $J_0 \gg J_{\text{th}}$, we disregard the difference between $J = J_{\text{th}}$ and $J = 0$. Thus, from equation (40) it follows that, in order to have a physical crossover, grains must have $J = 0$, and the aligning torque $F(\Theta)$ must be zero. The latter condition is naturally satisfied since we found that $F(\Theta) = 0$ at stationary points. The former one is satisfied as RATs act to decelerate the grain rotation. Indeed, equation (38) shows that $F(\Theta) > 0$, that is, it acts to increase Θ , for every angles $\Theta < \pi$. Yet, equation (37) shows that $H(\Theta) < 0$ for $\cos \Theta < 0$ and $H(\Theta) > 0$ for $\cos \Theta > 0$. Therefore, if initially the angular momentum of grains makes an angle $\cos \Theta < 0$, then their angular momentum is decreased due to $H(\Theta) < 0$; so grains approach directly to the state of $J = 0$ (see the upper panel in Fig. 13 for right-handed helical grain). On the other hand, for grains which initially have $\cos \Theta > 0$, the aligning torque acts to increase Θ , while the spinning torque increases their angular momentum. Eventually, grains attain the angle $\cos \Theta < 0$ for which the spinning torque changes the sign, so they are decelerated to the state of $J = 0$ (see Fig. 13 for phase maps of left- and right-handed helical grains).

One can observe that when grains get to the crossover with very low J , their maximal inertia axis $\hat{\mathbf{a}}_1$ flips with respect to \mathbf{J} to enter the opposite flipping state, that is, grains flip from the upper to lower panel in Fig. 13 (upper panel), for instance. Right after that, grains flip back to the initial state (upper panel). This back and forth flipping process takes place frequently. As a result, the crossover point, in our approach, can be treated as the attractor point at zero angular momentum, hereafter, called low- J attractor point,⁹ to be distinguished from high- J attractor points.

6.4 RATs: alignment by one component

The grain alignment for the case at hand is uniquely related to two components Q_{e1} and Q_{e2} . To understand which component causes the alignment, let us study the role of Q_{e1} and Q_{e2} separately.

If $Q_{e2} = 0$, then $(dQ_{e2}/d\Theta)(\Theta_s = 0, \pi) = 0$, equation (55) for attractor points becomes

$$Q_{e1}(\Theta_s = 0) > 0, \quad (56)$$

$$Q_{e1}(\Theta_s = \pi) < 0. \quad (57)$$

According to AMO, $Q_{e1}(\Theta_s = 0, \pi) = \frac{16l_1n_1n_2|n_2|}{3\lambda}(5\cos^2 \Theta_s - 2) = 1 > 0$. As a result, we expect that the stationary point $\Theta_s = 0$ is an attractor point, that is, grains are perfectly aligned with respect to \mathbf{k} . While, the stationary point $\Theta_s = \pi$ is a repeller point.

⁹ In Hoang & Lazarian (in preparation), we will show that zero angular momentum attractor points become attractor points at thermal angular momentum due to thermal wobbling.

For the case $Q_{e1} = 0$, besides stationary points $\Theta_s = 0, \pi$ as discussed above, there is another stationary point corresponding to $\Theta_s = \pi/2$ (see equation 33). For $\Theta_s = 0, \pi$, equation (55) reduces to

$$\frac{dQ_{e2}}{d\Theta}(\Theta_s = 0) < 0, \quad (58)$$

$$\frac{dQ_{e2}}{d\Theta}(\Theta_s = \pi) > 0. \quad (59)$$

For AMO with $\alpha = 45^\circ$, thus, $Q_{e2} = \frac{40l_1n_1n_2|n_2|}{3\lambda} \sin 2\Theta(1.191 + 0.1382 \cos^2 \Theta)$, we have $\frac{dQ_{e2}}{d\Theta}(\Theta_s = 0, \pi) = \frac{106.2l_1n_1n_2|n_2|}{3\lambda} \cos 2\Theta_s > 0$. It means that condition (58) is not satisfied, but equation (59) is fulfilled. In other words, the stationary point $\Theta_s = 0$ is a repeller point, while the stationary point $\Theta_s = \pi$ is an attractor point.

For a particular stationary point $\Theta_s = \pi/2$, equation (58) in this case becomes

$$\frac{Q'_{e2} \cos \Theta_s}{Q_{e2} \sin \Theta_s} = 0 < 1. \quad (60)$$

Therefore, the stationary point $\Theta_s = \pi/2$ is, indeed, an attractor point. Note, equation (60) which indicates that $\Theta_s = \pi/2$ is the attractor point is valid for an arbitrary form of Q_{e2} . These results show that the component Q_{e2} acts to align grains in the direction perpendicular to the radiation beam for arbitrary grain shapes.

6.5 Phase trajectories

To show our predictions from the above analysis, we construct phase trajectory maps in which each RAT component acts separately. The difference of our phase maps from those in DW97 is that here we present the alignment with respect to \mathbf{k} rather than to magnetic field. In addition, we treat crossovers differently from how they are treated in DW97. With the exception of Figs 23 and 26, to avoid overcrowding of our phase maps we do not draw arrows with t_{gas} intervals.

Throughout the present paper, the phase trajectory map represents the evolution of J and angle between \mathbf{J} and \mathbf{k} or \mathbf{B} .¹⁰ Each phase map has upper and lower panels, which correspond to \mathbf{J} parallel and antiparallel to \mathbf{a}_1 , respectively. Also, a circle denotes an attractor point and a cross denotes a repeller point.

Moreover, the title of the trajectory map presents information about the model (AMO) or grain shape, size for irregular grains. For trajectory maps labelled with AMO on their titles, it is a default that the RAT components are taken from the exact calculations of equations (10)–(12) for $\alpha = 45^\circ$ which have $Q_{e1}^{\max}/Q_{e2}^{\max} = 1.2$. For the maps of AMO in which the ratio $Q_{e1}^{\max}/Q_{e2}^{\max}$ is explicitly shown, it means that the functional forms of RATs are similar for the case $\alpha = 45^\circ$, but the relative amplitudes are rescaled to the shown value.

The map for the case when only Q_{e1} is present has three attractor points: A, B correspond to $\Theta_s = 0$, and E corresponds to zero of Q_{e1} at $\cos \Theta = -0.6$ (see the upper panel in Fig. 12). Therefore, Q_{e1} acts to align grains with \mathbf{J} parallel to \mathbf{k} , that is, \mathbf{a}_1 parallel or antiparallel to \mathbf{k} . In addition, there are two repeller points C, D. These features show clearly our predictions obtained with AMO.

When $Q_{e1} = 0$, Fig. 12 (lower panel) shows that the phase trajectory map has one attractor point D at $\Theta_s = \pi/2$, which corresponds to a perpendicular alignment, one low- J attractor point C at $\Theta_s = \pi$, and two repeller points A, B as predicted by the above analysis. So

¹⁰ We note that the angle between \mathbf{J} and \mathbf{k} or \mathbf{B} is shown rather than the angle between \mathbf{a}_1 and \mathbf{k} or \mathbf{B} as in DW97.

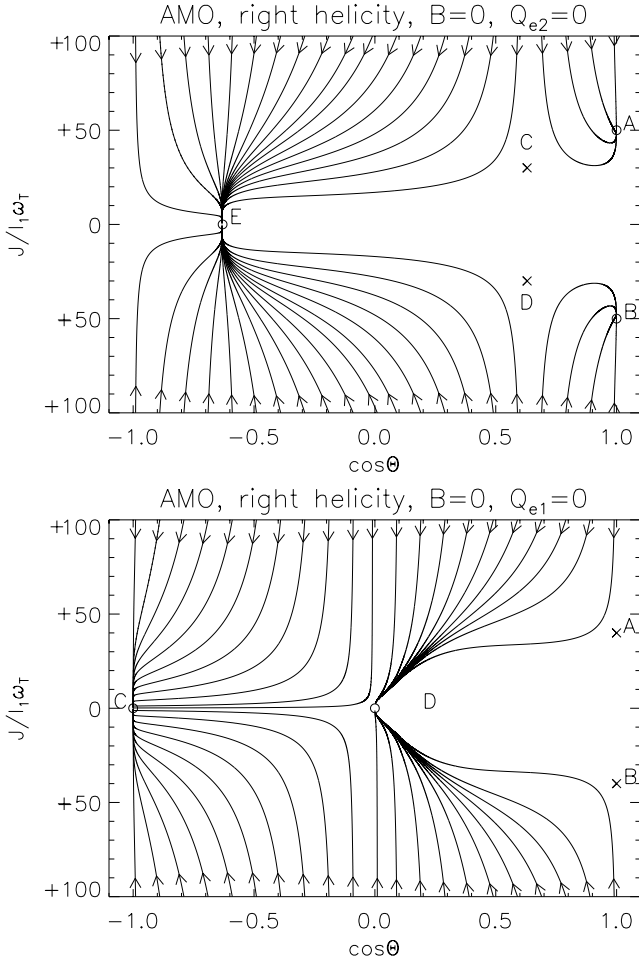


Figure 12. Phase trajectory maps of grains in the absence of magnetic field corresponding to $Q_{e2} = 0$ (upper panel) and $Q_{e1} = 0$ (lower panel). The map in upper panel exhibits two attractor points A, B corresponding to a perfect alignment as pointed out by the analysis; E is a low- J attractor point and the two repellor points are C and D. The lower panel shows two repellor points A, B and two attractor points C, D in which D corresponds to ‘wrong’ alignment.

Q_{e2} can align some grains with the maximal inertia axis \mathbf{a}_1 perpendicular to the light direction. However, we discussed in Section 2 that Q_{e2} is equal to zero at the attractor point $\Theta_s = \pi/2$, while Q_{e1} is different from zero at this point; thus the alignment with the long axes parallel to the direction of light does not occur¹¹ for the case of alignment with respect to \mathbf{k} (see Section 7.5).

6.6 RATs: alignment by joint action of torques, role of $Q_{e1}^{\max}/Q_{e2}^{\max}$ ratio

So far we have dealt with the alignment by one component of RATs, and pointed out that Q_{e1} acts to align grains with long axes \perp to \mathbf{k} , while Q_{e2} can produce the alignment for some grains with long axes \parallel to \mathbf{k} . In reality, grains are driven simultaneously by both components, so the alignment of grains depends on which component of RATs is predominant.

¹¹ We checked that even the addition of Q_{e1} with an amplitude of 10^{-9} of the amplitude of Q_{e2} can destroy such an alignment.

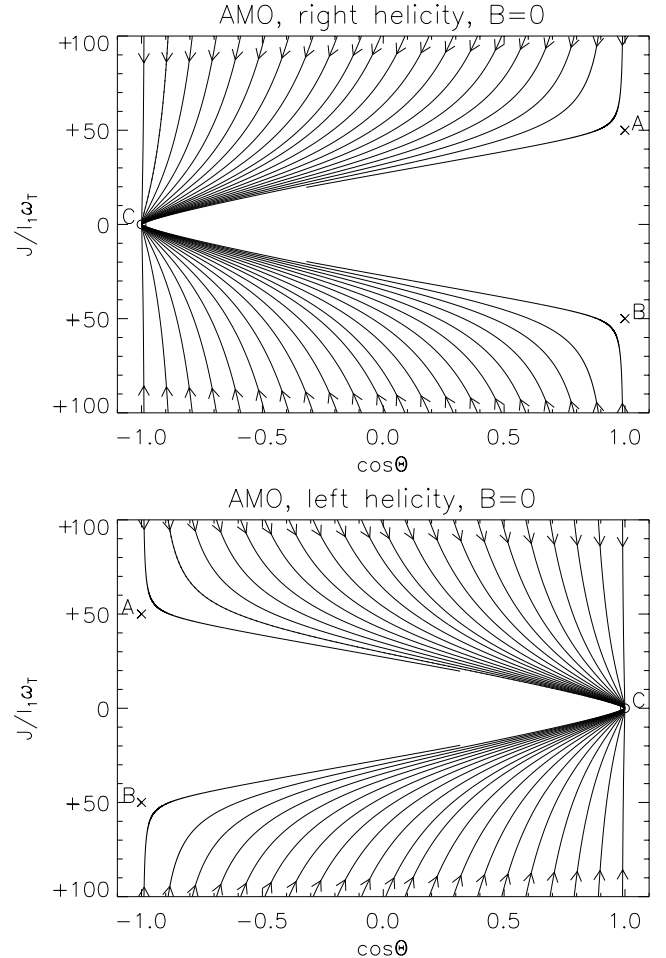


Figure 13. Upper and lower panels show the phase trajectory maps for grains with right- and left-handed helicity, respectively. Figures show that grains have a perfect alignment with respect to \mathbf{k} with one low- J attractor point C at $\Theta = \pi$ (upper panel) and $\Theta = 0$ (lower panel). Also, two repellor points A, B are shown as predicted in our analysis. The maps for upper and lower panels are mirror symmetric.

As discussed in previous sections, for AMO, we have the stationary point which is determined by equations (52) and (53). Also, we have analytically shown that the stationary point $\Theta_s = 0$ (π for left-handed helical AMO) is the repellor point. To test our expectation, we produce phase trajectory maps of grains driven by RATs with the precessing, spinning-up and aligning components given by equations (36)–(38). Fig. 13 shows the maps for right- and left-handed helical AMOs. It can be seen that the phase maps have two stationary points whose positions are exactly given by analytical expressions (52) and (53). Among these stationary points, there are two repellor points A, B at $\Theta_s = 0$ (or π for lower panel), and one low- J attractor point C at $\Theta_s = \pi$ (or $\Theta = 0$ for lower panel). In addition, we see that for the right- and left-handed helical AMOs, the trajectory maps are related through a transformation: $\Theta \rightarrow \pi - \Theta$.

We have seen that, in both cases of grain alignment by one component and joint actions of components, the important features (e.g. attractor and repellor points) present in the trajectory maps that are constructed with exact RATs are consistent with the predictions based on the approximate formulae using the fitting functions $f_{\pi/2}$ and g . It indicates that, though the fitting functions do not give the

best fit in some particular angles Θ , they can provide us, intuitively, the alignment property of grains by RATs.

We found in the case of alignment by one component that if only Q_{e1} is at work, it aligns grains with two attractor points with $J \gg J_{\text{th}}$, $\Theta = 0$, that is, high- J attractor points. In contrast, when only Q_{e2} acts, those points are repellor points; instead Q_{e2} produces an attractor point at $\Theta = \pi/2$. When both components act simultaneously, are there high- J attractor points? Obviously, we may conjecture that if Q_{e1} is predominant over Q_{e2} , then high- J attractor points should still appear. Otherwise, high- J stationary points are repellor points.

For our default AMO with $\alpha = \pi/4$, we have predicted that the stationary points $\Theta = 0$ are always repellor points. This can also be understood in terms of the ratio of $Q_{e1}^{\max}/Q_{e2}^{\max} \sim 1$, for this case, that is, the dominant criteria are not satisfied (see equations 19 and 20).

To study when we have high- J attractor points, let us write RATs for AMO in a simplified form:

$$Q_{e1} = \frac{Q_{e1}^{\max}}{3}(5\cos^2\Theta - 2), \quad (61)$$

$$Q_{e2} = Q_{e2}^{\max} \sin 2\Theta, \quad (62)$$

where $Q_{e1}^{\max}, Q_{e2}^{\max}$ are maximal values of Q_{e1}, Q_{e2} .

Clearly, stationary points for this model are $\Theta_s = 0$ because aligning torque $F(\Theta_s) = -Q_{e1} \sin \Theta_s + Q_{e2} \cos \Theta_s = 0$ at $\Theta_s = 0$.

Using the criteria of an attractor point (i.e. equation 55), it follows that $\Theta_s = 0$ is an attractor point if

$$\frac{1}{Q_{e1}} \frac{dQ_{e2}}{d\Theta}(\Theta_s = 0) < 1. \quad (63)$$

Plugging equations (61) and (62) into equation (63), we get

$$Q_{e1}^{\max} > 2Q_{e2}^{\max}. \quad (64)$$

From Fig. B6 and equation (64), it follows that for the original AMO, that is, AMO in which the relative magnitude of RAT component is not rescaled yet, the maximum of the ratio $\max[Q_{e1}^{\max}/Q_{e2}^{\max}]$ is 1.3, and therefore the stationary points $\Theta_s = 0$ (corresponding to high J) are always repellor points. However, as we have discussed earlier, their relative magnitude is adjustable. Thus, AMO can produce the phase map with high- J attractor points for $\psi = 0^\circ$, provided that it satisfies equation (64). Note that the criterion (64) is only applicable for the case of alignment with respect to \mathbf{k} or $\psi = 0^\circ$ (i.e. $\mathbf{k} \parallel \mathbf{B}$). For an arbitrary angle ψ , the criterion is shown in the lower panel of Fig. 24. There it can be seen that for some irregular grains (i.e. shape 1, ISRF) $\Theta_s = 0$ can correspond to high- J attractor points.

6.7 Alignment for irregular grains

Similar to the AMO case, we consider first the alignment of dust with respect to the radiation direction \mathbf{k} . In particular, to compare the action of RATs for AMO and an irregular grain, we consider the alignment that is induced by individual torque components.

To calculate the phase map, we use again the parameters from Table 2. We exemplify the alignment for irregular grains using shape 1, which shows the maximum deviations from AMO predictions.

Fig. 14 shows the phase trajectory maps of an irregular grain (shape 1) driven by RATs calculated by DDSCAT with either Q_{e2} or Q_{e1} taken to be zero.

We see that these trajectory maps are similar to those constructed by RATs from AMO (see Fig. 12). Indeed, for $Q_{e1} = 0$ case, the map for AMO in Fig. 12 shows two attractor points at $\cos \Theta = 1$, which are found in Fig. 14. However, in the situation when only Q_{e2} acts, the upper panel in Fig. 14 shows an attractor point at $\Theta = \pi/2$ and

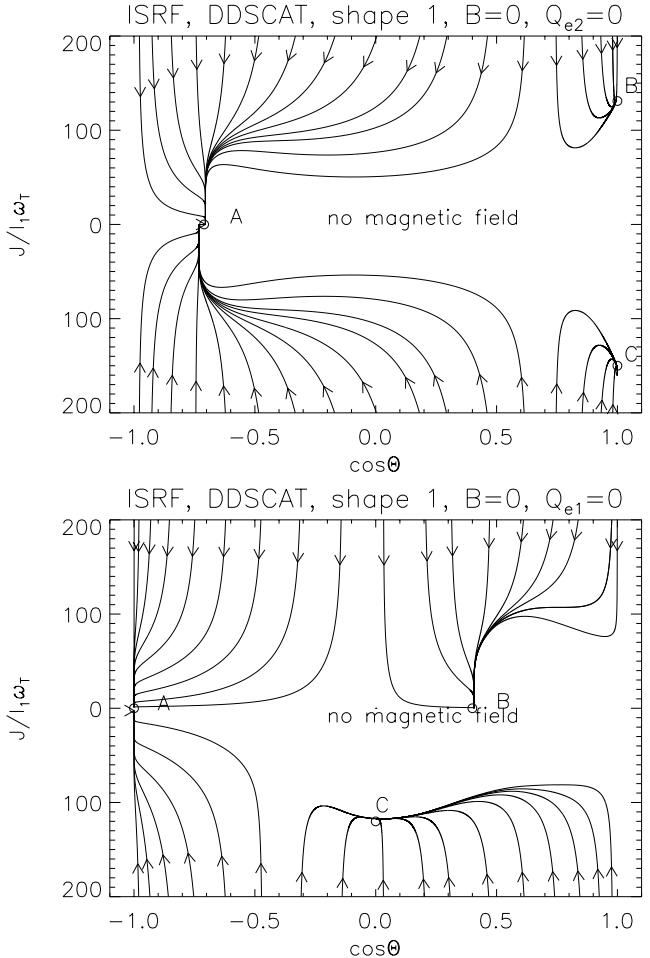


Figure 14. Phase trajectory maps in the absence of magnetic field corresponding to $Q_{e2} = 0$ (upper panel) and $Q_{e1} = 0$ (lower panel). The map in the upper panel has three attractor points A, B, C in which B, C correspond to high angular momentum. The map in lower panel has one attractor point C corresponding to ‘wrong’ alignment and two attractor points with $J = 0$.

$J \gg J_{\text{th}}$, which is somewhat different from Fig. 12. This difference stems from the fact that Q_{e2} for shape 1 is small, but not equal to zero at $\Theta = \pi/2$. Therefore, RATs are still able to spin up grains and align them there.

Fig. 15 shows the phase map when all torque components are at work, for shape 1. It is shown that the trajectory map does not have the attractor point at $\Theta = \pi/2$. Thus, similar to AMO, the attractor point corresponding to aligning grains with long axes parallel to the direction of radiation disappears when non-zero Q_{e1} is accounted for.

Moreover, from Fig. 15 (shape 1) and the upper panel in Fig. 13 for AMO, it is seen that both maps have the same repellor point at $\cos \Theta = 1$ in the upper panel. However, the point C in Fig. 15 is an attractor point, rather than a repellor point B as seen for AMO. This difference stems from the fact that for AMO, $Q_{e1} = \frac{4\pi l_1 n_1 n_2}{3\pi}(5\cos^2\Theta - 2)$ is completely symmetric, that is, $Q_{e1}(\Theta = 0) = Q_{e1}(\Theta = \pi)$, while for shape 1, Fig. 6 (the solid-dotted line) shows that $Q_{e1}(\Theta = 0) < Q_{e1}(\Theta = \pi)$. Therefore, the stationary point $\Theta = 0$ in the upper panel does not satisfy the criteria for attractor points, that is, it is a repellor point, while it is an attractor point in the lower panel.

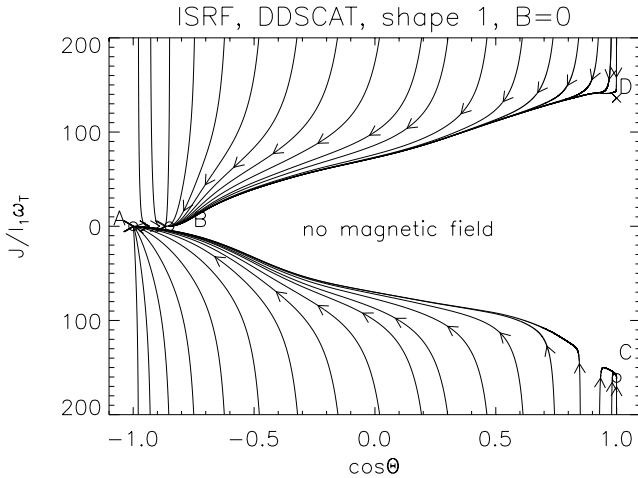


Figure 15. Phase trajectory map for grain shape 1 for $\psi = 0^\circ$ shows the alignment with one high- J attractor point C, two low- J attractor points A and B corresponding to perfect alignment with \mathbf{k} , and one repeller point D.

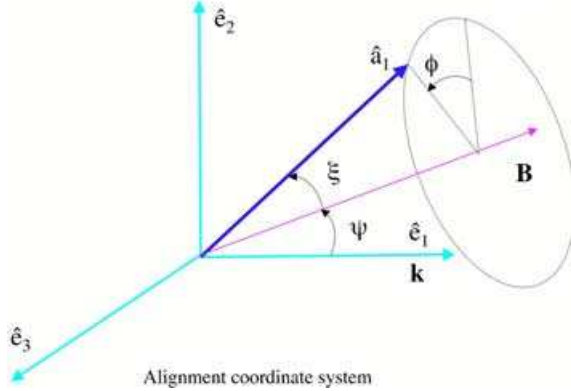


Figure 16. Coordinate systems used to study grain alignment in which the external magnetic field \mathbf{B} defines the alignment axis.

7 ALIGNMENT WITH RESPECT TO \mathbf{B}

We showed in Section 6 that grains can be aligned with respect to \mathbf{k} . Below we consider the case when magnetic field is essential in terms of grain precession (see Fig. 16). As earlier, we disregard the paramagnetic relaxation. We make an extensive use of the physical insight obtained with a more simple case of alignment in Section 6. Indeed, because of the precession about magnetic field the analytical treatment of the corresponding processes gets less transparent here compared to that in Section 6.

7.1 Equations of motion in presence of \mathbf{B}

In the presence of magnetic field, equations of motion in dimensionless units become

$$\frac{d\phi}{dt} = \frac{M}{\sin \xi} G(\xi, \psi, \phi) - \Omega_B, \quad (65)$$

$$\frac{d\xi}{dt} = M \frac{F(\xi, \psi, \phi)}{J}, \quad (66)$$

$$\frac{dJ}{dt} = M H(\xi, \psi, \phi) - J, \quad (67)$$

where Ω_B is the Larmor precession rate of \mathbf{J} around the magnetic field \mathbf{B} . Here F, H, G are RAT components projected to three axes $\xi, \hat{\mathbf{j}}, \hat{\mathbf{\phi}}$, which are given by (see DW97)

$$\begin{aligned} F(\xi, \psi, \phi) &= Q_{e1}(\Theta, 0)[-\sin \psi \cos \xi \cos \phi - \cos \psi \sin \xi] \\ &\quad + Q_{e2}(\Theta, 0)[\cos \Phi (\cos \psi \cos \xi \cos \phi \\ &\quad - \sin \psi \sin \xi) + \sin \Phi \cos \xi \sin \phi] \\ &\quad + Q_{e3}(\Theta, 0)[\cos \Phi \cos \xi \sin \phi + \sin \Phi (\sin \psi \sin \xi \\ &\quad - \cos \psi \cos \xi \cos \phi)], \end{aligned} \quad (68)$$

$$\begin{aligned} H(\xi, \psi, \phi) &= Q_{e1}(\Theta, 0)[-\sin \psi \sin \xi \cos \phi + \cos \psi \cos \xi] \\ &\quad + Q_{e2}(\Theta, 0)[\cos \Phi (\sin \psi \cos \xi \\ &\quad + \cos \psi \sin \xi \cos \phi) + \sin \Phi \sin \xi \sin \phi], \end{aligned} \quad (69)$$

$$\begin{aligned} G(\xi, \psi, \phi) &= Q_{e1}(\Theta, 0)[\sin \psi \sin \phi] \\ &\quad + Q_{e2}[\sin \Phi \cos \phi - \cos \Phi \cos \psi \sin \phi] \\ &\quad + Q_{e3}[\cos \Phi \cos \phi + \sin \Phi \cos \psi \sin \phi]. \end{aligned} \quad (70)$$

Here Θ and Φ are related to ξ, ψ, ϕ via

$$\cos \Theta = \cos \xi \cos \psi - \sin \xi \sin \psi \cos \phi, \quad (71)$$

$$\Phi = 2\tan^{-1} \frac{\sin \Theta - \sin \xi \sin \psi}{\sin \xi \sin \phi}. \quad (72)$$

Equation (69) reveals explicitly that the component $Q_{e3}(\Theta, 0)$ does not contribute to spinning-up grains. On the other hand, we found numerically that the last term containing $Q_{e3}(\Theta, 0)$ in equation (68) goes to zero after averaging over the precession angle ϕ . Therefore, similar to the case of alignment with respect to \mathbf{k} , the only effect of $Q_{e3}(\Theta, 0)$ is to induce the grain precession.

After averaging over the precession angle ϕ , the equations of motion (65)–(67) are reduced to two equations for ξ and J , whereas $F(\xi, \psi, \phi), H(\xi, \psi, \phi)$ are replaced by $\langle F(\xi, \psi) \rangle_\phi, \langle H(\xi, \psi) \rangle_\phi$.

7.2 Stationary points for arbitrary shaped grains

While in this section we deal with AMO, some results can be obtained in a general case of arbitrary shaped grains. More results of this nature are presented in Section 8.

In the presence of magnetic field, aligning and spinning torques are complicated functions of RATs, involving ψ, ξ, ϕ variables. Therefore, it is not easy to derive general analytical expressions for stationary points. However, we can find some particular physically interesting situations that correspond to stationary points.

For instance, the perfect alignment corresponds to the maximal inertia axis \mathbf{a}_1 parallel to the magnetic field, that is, $\sin \xi_s = 0$. For this angle, from equations (71) and (72), we have $\Theta = \psi$, and $\Phi = 0$ or π . Hence, $Q_{e1}(\Theta, 0) = Q_{e1}(\psi, 0)$, $Q_{e2}(\Theta, 0) = Q_{e2}(\psi, 0)$. Equation (68) becomes

$$\begin{aligned} F(\xi_s, \psi, \phi) &= Q_{e1}(\psi, 0) \sin \psi \cos \phi + Q_{e2}(\psi, 0) \cos \Phi \cos \phi \\ &\quad + Q_{e3}(\xi_s, 0) \cos \Phi \sin \phi. \end{aligned} \quad (73)$$

Obviously, $F(\xi_s, \psi, \phi)$ is a function of the precession angle ϕ about the magnetic field \mathbf{B} . Thus, if the grain precesses rapidly around \mathbf{B} , then we can average $F(\xi_s, \psi, \phi)$ over ϕ from 0 to 2π . As

a result,

$$\begin{aligned} \langle F(\xi_s, \psi) \rangle_\phi &= Q_{e1}(\psi, 0) \sin \psi \int_0^{2\pi} \cos \phi d\phi \\ &+ Q_{e2}(\psi, 0) \cos \Phi \int_0^{2\pi} \cos \phi d\phi \\ &+ Q_{e3} \cos \Phi \int_0^{2\pi} \sin \phi d\phi = 0, \end{aligned} \quad (74)$$

which implies that for *grains of an arbitrary shape*, and for *arbitrary direction of light with respect to the magnetic field*, there are always two stationary points at $\xi_s = 0$ and π . This very fact makes the alignment of the grains with long axes perpendicular to \mathbf{B} in some sense the expected one, although it does not present a sufficient condition for such an alignment.

If attractor points exist for ξ_s different from 0 or π , the alignment may get ‘wrong’, that is, with the maximal inertia axis of the grain tending to be parallel to the magnetic field. Here and below we adopt the convention that the alignment is ‘right’ if it corresponds to the Davis–Greenstein predictions, which made the Davis–Greenstein mechanism so popular even in spite of its inefficiency. Needless to say that for RATs we seek ‘right’ alignment, that is, with long grain axes perpendicular to magnetic fields without appealing for paramagnetic relation.

The ‘wrong’ alignment may be expected, for instance, when the radiation beam is perpendicular to the magnetic field, that is, $\psi = \pi/2$. For this ψ , consider the direction of ‘wrong’ alignment corresponding to $\xi_s = \pi/2$. For $\psi = \pi/2$ and $\xi = \pi/2$, we have $\cos \Theta = -\cos \phi$, and $\Phi = \pi/2$ for $\phi < \pi$ and $-\pi/2$ for $\phi > \pi$. Therefore, equation (68) becomes

$$F(\xi_s, \psi, \phi) = Q_{e3}(\Theta, 0) \sin \Phi. \quad (75)$$

Thus

$$\langle F(\xi_s, \psi) \rangle_\phi = \int_0^{2\pi} Q_{e3}(\phi, 0) d\phi = 0. \quad (76)$$

Here we use the property $Q_{e3}(\phi, 0) \sim \sin 2\phi$ in calculating the integral.

7.3 ‘Right’ and ‘wrong’ alignment for AMO

The introduction of fast precession arising from \mathbf{B} makes the dynamics of grains more interesting. For instance, it allows for a parameter space for ‘wrong’ alignment, high- J attractor points for AMO, shifts of the crossover points.

7.3.1 Torques considerations

Above, we have found that in the presence of \mathbf{B} , two permanent stationary points are $\xi_s = 0, \pi$. If being attractor points, they correspond to the ‘right’ alignment.

Consider a case of suspected ‘wrong’ alignment for AMO at $\xi_s \sim \pi/2$. Since as $\psi = \pi/2$, $\cos \Theta = -\cos \phi$, so RATs (see equations 34 and 35) become

$$Q_{e1} = \frac{16l_1 n_1 n_2 |n_2|}{3\lambda} (5 \cos^2 \phi - 2), \quad (77)$$

$$Q_{e2} = \frac{40l_1 n_1 n_2 |n_2|}{3\lambda} \sin 2\phi (1.191 + 0.1382 \cos^2 \phi). \quad (78)$$

Substituting equations (77) and (78) into equation (69) and averaging over the precession angle ϕ , we get

$$\begin{aligned} \langle H(\xi, \psi) \rangle_\phi &= \frac{16l_1 n_1 n_2 |n_2|}{3\lambda} \int_0^{2\pi} (5 \cos^2 \phi - 2) \cos \phi d\phi \\ &+ \frac{40l_1 n_1 n_2 |n_2|}{3\lambda} \left[\int_0^{2\pi} \sin 2\phi \sin \phi (1.191) d\phi \right. \\ &\left. + \int_0^{2\pi} \sin 2\phi (0.1382 \cos^2 \phi) d\phi \right] = 0. \end{aligned} \quad (79)$$

The fact that the integral (79) is equal to zero means that RATs do not spin up grains when they are perpendicular to the magnetic field.

Now, let us study whether $\xi_s = \pi/2$ satisfies the condition of an attractor point. Fig. 18 (upper panel) shows the spinning and aligning torques for $\psi = 89.9^\circ \sim 90^\circ$ ¹² for the state $\mathbf{a}_1 \parallel \mathbf{J}$. It shows that, there are stationary points at $\cos \xi = \pm 1$ and $\cos \xi_s = 0.1, -0.1$ for the \mathbf{J} parallel and antiparallel to \mathbf{a}_1 corresponding to zeros of $\langle F(\xi) \rangle_\phi$. For the stationary point C with $\cos \xi_s = 0.1$, Fig. 18 shows $\frac{d\langle F(\xi) \rangle_\phi}{d\xi}|_{\xi_s} > 0$, and $\langle H(\xi_s) \rangle_\phi > 0$. Hence, this stationary point does not satisfy equation (44), that is, it is a repeller point. Meanwhile, for the stationary point C' at $\cos \xi_s = -0.1$, we have $\frac{d\langle F(\xi) \rangle_\phi}{d\xi}|_{\xi_s} < 0$ and $\langle H(\xi_s) \rangle_\phi > 0$. As a result, the stationary point C' is an attractor point. Similarly, the point A at $\cos \xi_s = 1$ is an attractor point since $\frac{d\langle F(\xi) \rangle_\phi}{d\xi}|_{\xi_s} < 0$ and $\langle H(\xi_s) \rangle_\phi > 0$; also, the point B is a low- J attractor point. However, the points A' and B' are repeller points in the case \mathbf{J} antiparallel to \mathbf{a}_1 .

Therefore, the possibility of existence of ‘wrong’ alignment is feasible, but it happens at a low angular momentum. So, RATs from anisotropic radiation field themselves cannot maintain the ‘wrong’ alignment with respect to magnetic field in the presence of thermal wobbling and the bombardment by the ambient gas (see Hoang & Lazarian, in preparation).

7.3.2 Effect of isotropic torques on ‘wrong’ alignment

If grains are sufficiently large not to experience frequent thermal flips (see LD99a), they can be subjected to regular isotropic torques, which include both Purcell’s torques (Purcell 1979) and those from isotropic radiation flux (DW96). According to LD99b, this corresponds to grains larger than 10^{-4} cm, which is much larger than the typical size of the grains in Table 2. However, such large grains are relevant to many astrophysical environments, for example, comets, dark clouds, accretion discs.

The ‘wrong’ alignment gets modified when we take into account RATs induced by isotropic radiation, or equivalently, Purcell’s H_2 torques. Indeed, ‘isotropic’ RATs and Purcell’s spin-wheel are both parallel to the maximal inertia axis, that is, \mathbf{a}_1 . Therefore, the total spinning and aligning torques are $\langle H(\xi, \psi) \rangle_\phi + Q_{\text{iso}}$, $\langle F(\xi, \psi) \rangle_\phi$, respectively.

Since the aligning torque $\langle F(\xi, \psi) \rangle_\phi$ depends uniquely on RATs induced by anisotropic radiation, the positions of ‘wrong’ attractor points do not change. Meanwhile, their angular momenta are added by a term resulting from ‘isotropic’ RATs or Purcell spin-wheel.

¹² Here we take $\psi = 89.9^\circ$ to avoid the singularity that may appear due to zero of $\langle H \rangle$ as shown in equation (79) when considering condition of attractor points.

Now, let us introduce H_2 torques. H_2 torques, after averaging over the grain rotation around the maximal inertia axis, are given by

$$\Gamma_{H_2} = \mathbf{a}_1 \frac{I_1 \omega_{H_2}}{t_{\text{gas}}} p, \quad (80)$$

where

$$\omega_{H_2} \sim 5 \times 10^7 \left(\frac{f}{a_{-5}^2} \right) \left(\frac{l}{10A^0} \right) \left(\frac{E}{0.2eV} \right)^{1/2} \left[\frac{n(H)}{n} \right] s^{-1}. \quad (81)$$

Here l^2 is the surface area of a catalytic site of the grain surface, f is the efficiency of H_2 formation, $n(H)$ is the density of atomic hydrogen, E is the kinetic energy of the escaping H_2 molecule and p is a random variable (see DW97). In addition to parameters given in Table 2, here we assume that $n(H)/n = 1$, $f = \frac{1}{3}$, $l = 10A^0$ and $E = 0.2 \text{ eV}$; we consider then the role of H_2 torques for $p = 1$, -1 corresponding to Γ_{H_2} parallel and antiparallel to \mathbf{a}_1 .

7.3.3 Trajectory maps

To illustrate the alignment with respect to the magnetic field for AMO, we construct phase trajectory maps using RATs obtained by averaging equations (10)–(12), for different radiation directions ψ . To do this we adopt the parameters from Table 2. For $\psi = 0^\circ$, that is, $\mathbf{B} \parallel \mathbf{k}$, the phase map shown in the upper panel of Fig. 13 exhibits a perfect alignment of \mathbf{J} with respect to \mathbf{B} .

Fig. 17 shows the phase trajectory maps for $\psi = 30^\circ, 60^\circ$ with two repellors A and B, and one low- J attractor point C.

For $\psi \sim 90^\circ$, the lower panel in Fig. 18 shows an attractor point C' at $\cos \xi = -0.1$ corresponding to $J \sim 0$ and two repellor points at $\cos \xi = 1$, respectively. It is shown that the phase map is not symmetric between upper and lower panels compared to the maps for $\psi < 90^\circ$. This stems from the fact that spinning and aligning torques are no longer symmetric. The existence of the attractor point C' indicates that there is, indeed, a ‘wrong’ alignment situation as predicted by our analysis above. However, to what extend of ψ the ‘wrong’ alignment occurs?

Fig. 19 shows the angle of attractor points (upper panel) and their corresponding angular momentum (lower panel) for a range $\psi = [89:5, 90^\circ]$. In each frame of Fig. 19 (lower panel), we show angular momentum of attractor points present in both upper and lower panels of a trajectory map (upper and lower panels are labelled).

For the case $Q_{\text{iso}} = 10^{-5}, p = 0$, the upper panel in Fig. 19 shows that there are always three attractor points in which one attractor point happens at $\cos \xi = -0.1, -0.05$ and 0 for $\psi = 89:5, 89:8$ and 90° , corresponding to ‘wrong’ alignment, two other with $\cos \xi = \pm 1$. However, their angular momentum is very low, about $1.5 I_1 \omega_T$ (top frame in Fig. 19, lower panel). When H_2 torques are taken into account, if H_2 torques are parallel to \mathbf{a}_1 , that is, $p = 1$, then the attractor points $\cos \xi = \pm 1$ are lifted to $J/I_1 \omega_T \sim 100$, while the angular momentum of the ‘wrong’ attractor point is unchanged (see the middle frame in Fig. 19, lower panel). In contrast, if $p = -1$, the angular momentum of the ‘wrong’ attractor point can be increased by H_2 torques to $J/I_1 \omega_T = 100$, but the attractor points $\cos \xi = \pm 1$ are unchanged (see lower frame in Fig. 19, lower panel). Note that the shift of ‘wrong’ attractor point position towards $\cos \xi = 0$ is also seen on the diagram when $\psi \rightarrow 90^\circ$ (Fig. 19, upper panel).

In summary, the presence of ‘wrong’ alignment with respect to magnetic fields can be expected, but it happens in a very narrow range of ψ in the vicinity of $\psi = \pi/2$. In addition, their angular momentum is very low in the absence of isotropic torques such as

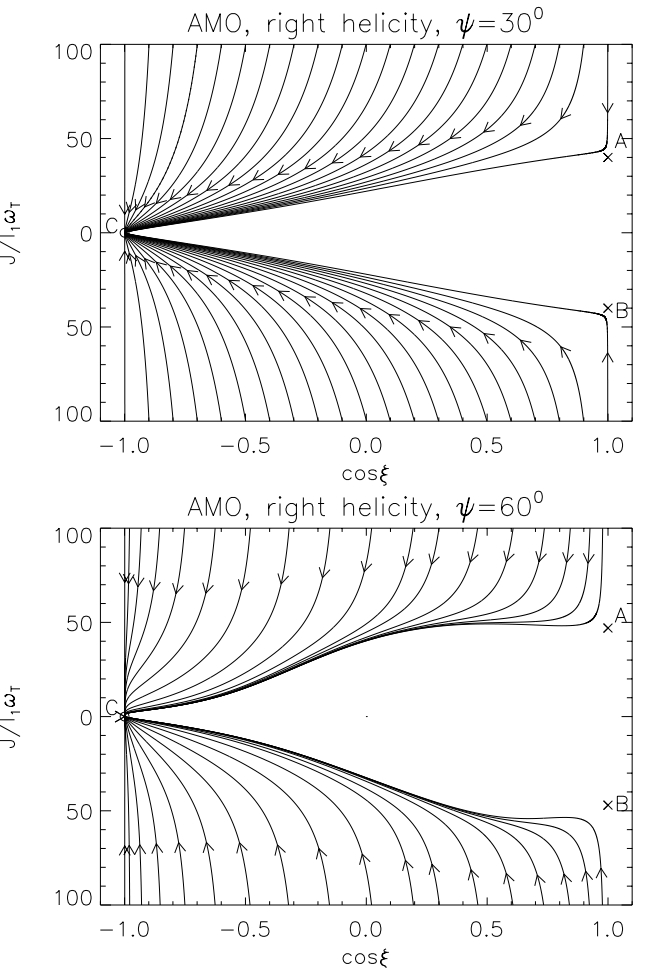


Figure 17. Phase trajectory maps for AMO for $\psi = 30^\circ$ (upper panel) and $\psi = 60^\circ$ (lower panel) both have zero attractor point C, and two repellor points A, B.

H_2 torques and ‘isotropic’ RATs. Naturally, the effects of isotropic torques are negligible if grains are flipping, and therefore are thermally trapped as it is discussed in LD99a.

7.4 Alignment for irregular grains

Similarly as in Section 6 we present the phase trajectory maps for shape 1, which is the ‘most irregular’ in terms of RATs. Consider first phase maps for shape 1 obtained for $\psi = 90^\circ$ first (see Fig. 20). For this case, RATs for shape 1 create an attractor point at $\xi = 90^\circ, J/I_1 \omega_T = 2$ in the phase map, which corresponds to *wrong alignment* (see Fig. 20). AMO also does produce such a ‘wrong’ alignment but at much smaller angular velocity, $J/I_1 \omega_T \sim 0$ (see Fig. 18). This difference is resulted from the property of Q_{e2} component. Following AMO, $Q_{e2} = 0$ at $\Theta = \pi/2$, while for shape 1, this component is not zero at this angle.

All in all, for various grain shapes studied, we found that there is a narrow range $\psi = 85^\circ\text{--}90^\circ$ in which there exists ‘wrong’ alignment.

In addition, we illustrate the alignment with respect to magnetic field with phase trajectories obtained for $\psi = 30^\circ$. For shape 1, similar studies were performed in DW97. However, their treatment of crossovers was different from ours. Thus the phase trajectories that we observe are different. We do not see cyclic maps with grains

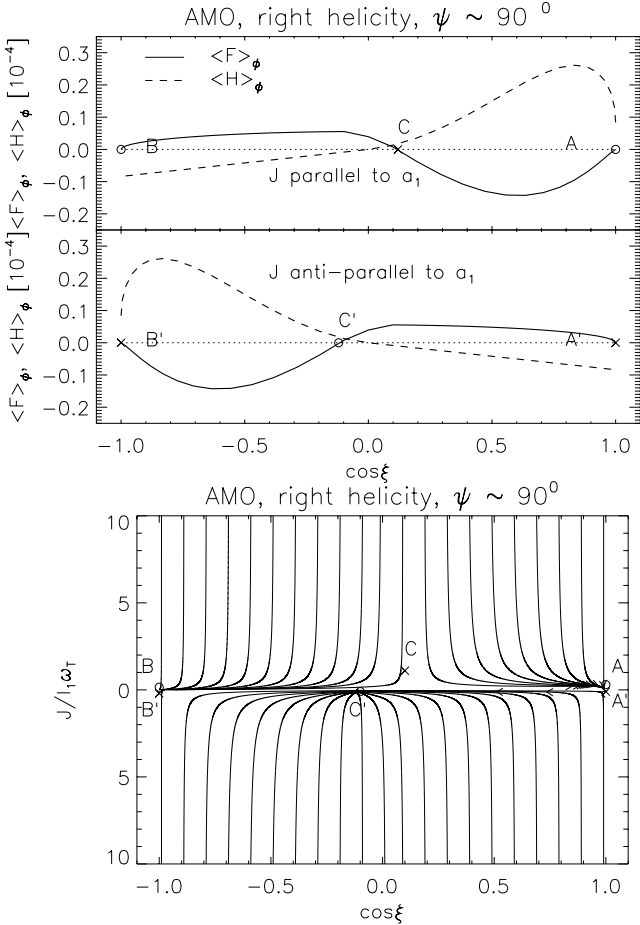


Figure 18. Aligning and spinning torques for the particular direction of light $\psi \sim 90^\circ$ and the corresponding phase map for AMO. Upper panel: Solid line shows the aligning torque $\langle F(\xi, \psi) \rangle_\phi$ with two zeros corresponding to two stationary points at $\cos \xi = 0.1, -0.1$ corresponding to the case J parallel and antiparallel to a_1 , besides two zeros $\cos \xi = \pm 1$, while the dashed line shows the spinning-up torque $\langle H(\xi, \psi) \rangle_\phi$. Lower panel: Phase map corresponding to RATs in the upper panel shows one ‘wrong’ attractor point C’ at very low $J/I_1 \omega_T \sim 0$ and $\cos \xi = -0.1$.

emerging from a crossover to get accelerated by RATs. Instead, we see, similar to the case of AMO (see Fig. 17, upper panel), the low- J attractor points (see Fig. 21).

Our study provides important insight into the role of Q_{e1} and Q_{e2} components. For instance, in the presence of magnetic field Q_{e1} tends to provide the alignment with long axes perpendicular to magnetic field, that is, the ‘right’ alignment. The possibility of ‘wrong’ alignment within a limited range of ξ is related to Q_{e2} . Similarly, the ratio of $Q_{e1}^{\max}/Q_{e2}^{\max}$ determines the existence of the high- J attractor points.

7.5 Ratio of $Q_{e1}^{\max}/Q_{e2}^{\max}$: existence of high- J and shift of low- J attractor points

The role of the ratio $Q_{e1}^{\max}/Q_{e2}^{\max}$ on the grain alignment has been studied in Section 6.6 for the case of no magnetic field (see Section 6 when this is applicable). Below we consider the role of this ratio when the magnetic field is present. We shall show that this ratio is important in determining whether grains have high- J attractor points.

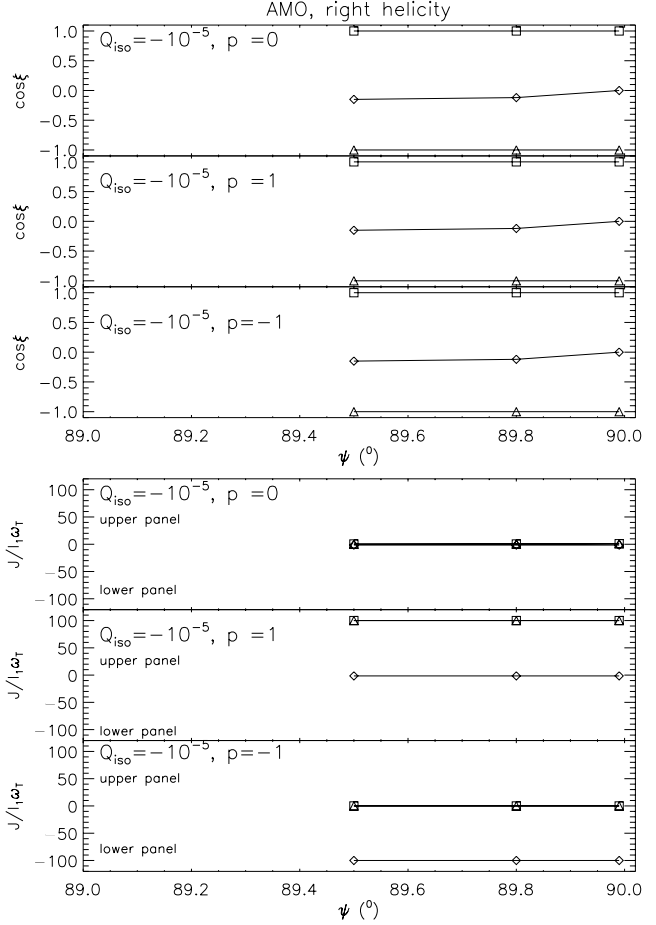


Figure 19. Diagram for the position (upper panel) and angular momentum (lower panel) of attractor points as function of ψ for three cases, $Q_{\text{iso}} = -10^{-5}, p = 0$ (no H_2 torques), $Q_{\text{iso}} = -10^{-5}, p = 1$ (Γ_{H2} is parallel to a_1), and $Q_{\text{iso}} = -10^{-5}, p = -1$ (Γ_{H2} is antiparallel to a_1). Each symbol (diamond, triangle and square) denotes an attractor point, and a symbol-line shows the extend of the ‘wrong’ alignment as a function of ψ .

In previous subsections we have derived the expressions for the stationary points, and presented the trajectory maps for the RAT alignment for a particular α , namely, $\alpha = 45^\circ$. It is clearly shown that stationary points $\cos \xi = \pm 1$ do not depend on the magnitude of Q_{e1}, Q_{e2} . However, their properties, that is, whether they are attractor or repellor points do so.

Let us first consider a realization of AMO in which the functional forms are established for $\alpha = 45^\circ$ and their magnitudes are rescaled to have $Q_{e1}^{\max}/Q_{e2}^{\max} = 0.78$ (see Fig. B6). Note that this ratio is similar to the ratio of RATs obtained by DDSCAT for the irregular shape 4 with radiation field of wavelength $\lambda = 1.2 \mu\text{m}$ (see Fig. 5).

Fig. 22 shows the obtained trajectory maps for $\psi = 60^\circ$ for both AMO and shape 4. We see that both AMO and shape 4 produce the maps with two attractor points A, B at $\cos \xi = -1$ and one low- J attractor point C, but one difference is that the percentage of grains on A and B for shape 4 is higher than that for AMO. For AMO and $\psi = 60^\circ$, the existence of high- J attractor points A and B with $Q_{e1}^{\max}/Q_{e2}^{\max} = 0.78$ is not found in the case $\alpha = 45^\circ$ that has $Q_{e1}^{\max}/Q_{e2}^{\max} = 1.2 > 1$ in which these points are repellor points (see Fig. 17). In other words, the existence of high- J attractor points depends on the value of $Q_{e1}^{\max}/Q_{e2}^{\max}$ as predicted in Section 6.6.

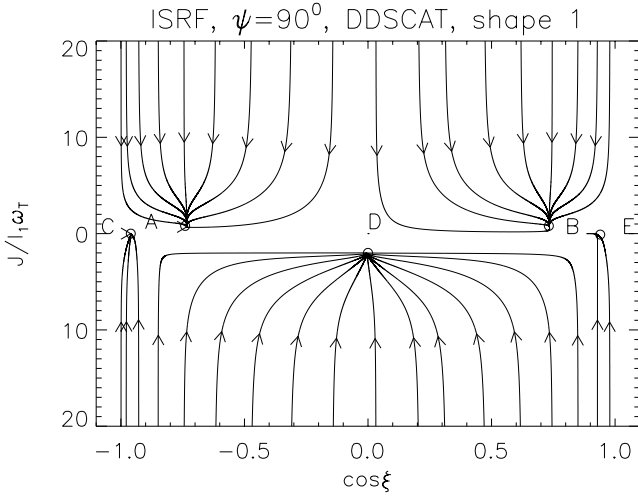


Figure 20. For $\psi = 90^\circ$, the map shows three high- J attractor point A, B and D and two low- J attractor points C and E. Most grains in the lower frame of the map align on D with long axes parallel to \mathbf{B} , that is, ‘wrong’ alignment.

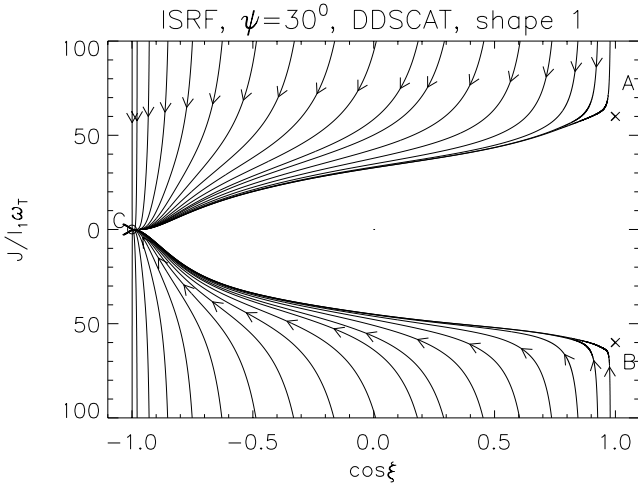


Figure 21. Phase trajectory map for grain shape 1 and $\psi = 30^\circ$ shows the alignment with two repellor points A and B and one low- J attractor point C.

Furthermore, the similarity in the phase maps between the AMO and shape 4, which have the similar ratio $Q_{e1}^{\max}/Q_{e2}^{\max} = 0.78$, indicates a good correspondence of AMO with irregular grains in terms of grain dynamics.

While in most cases, we show the phase trajectory maps that start from high values of J . In Fig. 23 we also show the phase trajectories starting at $J = J_{\text{th}}$. The dynamics with these initial conditions are similar. However, the alignment can be achieved faster (see further discussion in Section 9.3). The filled arrows in Fig. 23 mark time-scales of $0.5t_{\text{gas}}$. We see that it takes approximately less than $0.5 t_{\text{gas}}$ to get to the lower J attractor point C for grains with initial orientation close to C, for the typical interstellar diffuse gas conditions. Also, it takes about $3t_{\text{gas}}$ to get to the high- J attractor points A and B (see Fig. 23). These time-scales are usually much smaller than that for paramagnetic damping invoked in the Davis–Greenstein mechanism.

Now let us use the approximate functional form of RATs given by equations (61) and (62), and seek the range of $Q_{e1}^{\max}/Q_{e2}^{\max}$, in

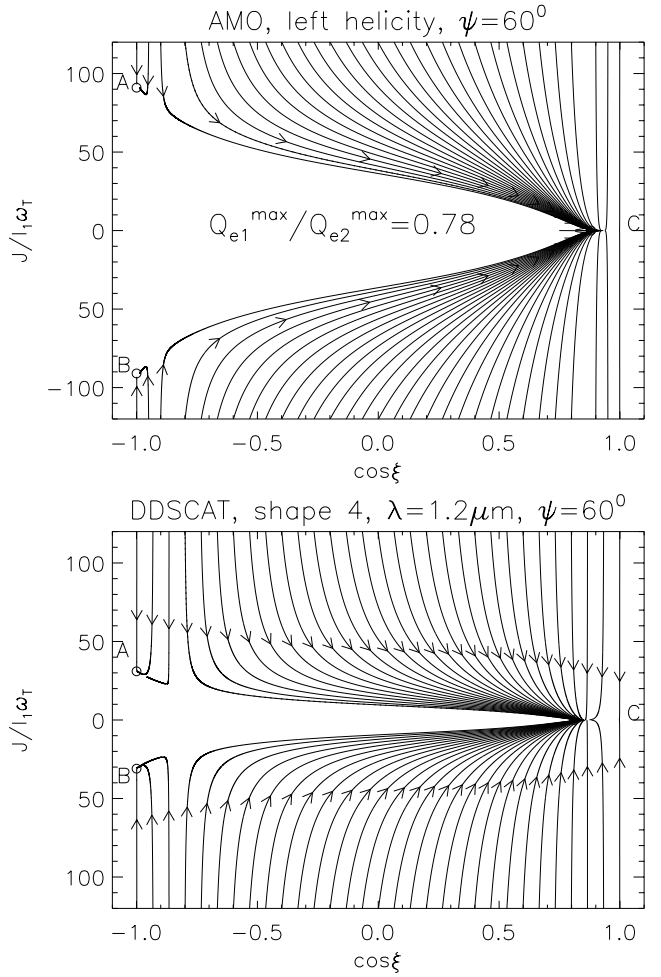


Figure 22. Phase trajectory maps with $\psi = 60^\circ$ for the case of AMO (upper panel) and for shape 4 (see Fig. 4) corresponding to the same ratio $Q_{e1}^{\max}/Q_{e2}^{\max} = 0.78$ (lower panel). The maps show that both AMO and DDSCAT give rise to two high- J attractor points A, B at $\cos \xi = -1$ and one low- J attractor point C.

which the phase map has high- J attractor points. Fig. 24 shows the ratio of $Q_{e1}^{\max}/Q_{e2}^{\max}$ for which there exist high- J attractor points in the phase trajectory map of grains. It is shown that for $\psi < 45^\circ$, Q_{e1} is required to be dominant over Q_{e2} , at least $Q_{e1}^{\max} = 2Q_{e2}^{\max}$, to have high- J attractor points; their ratio is an increasing function of ψ . At $\psi = 45^\circ$, one does not have high- J attractor points because Q_{e1}, Q_{e2} are equally projected to \mathbf{B} and to the direction ξ perpendicular to \mathbf{B} .

For $\psi > 45^\circ$, high- J attractor points occur when Q_{e2} becomes predominant, that is, $Q_{e1}^{\max}/Q_{e2}^{\max} < 1$ (see the lower panel in Fig. 24). Also in Fig. 24, the intermediate region with parallel lines corresponds to the range in which the phase trajectory map has only low- J attractor points, while high- J stationary points are repellors.

Fig. 24 shows also the existence of high- J attractor points for irregular shapes 1 (both monochromatic radiation field and ISRF), 2 and 4 (only monochromatic radiation). For shape 1 and radiation of $\lambda = 1.2 \mu\text{m}$, its phase map has low- J attractor points for $\psi < 60^\circ$ and high- J attractor points for $\psi \geq 60^\circ$. But, the map for ISRF has J attractor point only in a small range $\psi < 10^\circ$. Interestingly enough, for this wavelength, the ratio of $Q_{e1}^{\max}/Q_{e2}^{\max}$ exceeds those possible for the ‘original’ AMO. As a result, as we mentioned earlier, an attractor point is possible for $\psi = 0$, which also describes the

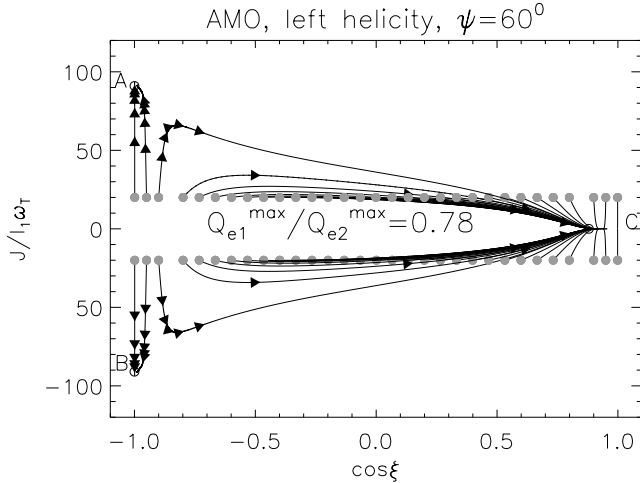


Figure 23. Similar to the upper panel in Fig. 22, but grains start from angular momentum smaller than the value of high- J attractor point. Filled circles show initial position of grains. Filled arrow shows the time interval of $0.5t_{\text{gas}}$. Some grains get aligned at low- J attractor point over a short time $t < 0.5t_{\text{gas}}$, some others get to the high- J attractor points over $t \sim 3t_{\text{gas}}$.

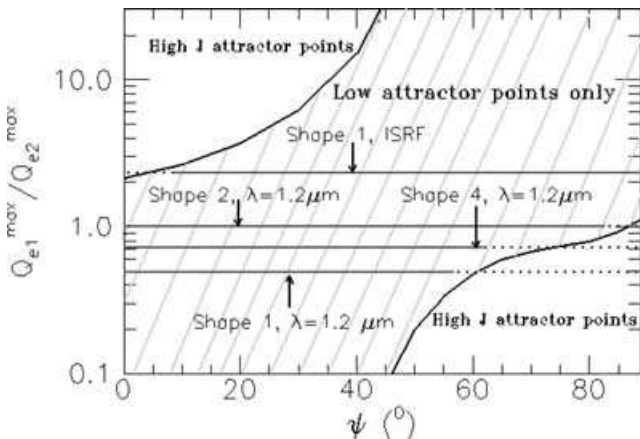


Figure 24. Ratio of $Q_{e1}^{\max}/Q_{e2}^{\max}$ for which the phase map has high- or low- J attractor points as a function of ψ . Curved solid lines show predictions by AMO, solid lines (maps with low- J attractor points only), dotted lines (maps with high- J attractor points) show the result for irregular grains.

situation of grain alignment in the absence of magnetic field. For such situations AMO has only repeller points (see Section 6).

The differences in the range of ψ in which the maps have high- J attractor points predicted by AMO and irregular grains (i.e. dotted lines extend outside the region surrounded by thick solid lines in Fig. 24) exist, but it is moderate. In fact, the correspondence between the ranges of ψ for the existence of the high- J attractor point revealed between our predictions and the actual irregular grains allows one to find out whether the high- J attractor point is expected if only the $Q_{e1}^{\max}/Q_{e2}^{\max}$ ratio is known. Note that the existence of high- J attractor points is important for evaluating the degree of grain alignment.

Another new effect related to the $Q_{e1}^{\max}/Q_{e2}^{\max}$ ratio is a regular shift of the position of the crossover point, which, as we discussed below, is also low- J attractor point. Fig. 25 (upper panel) shows this shift as a function of the ratio $Q_{e1}^{\max}/Q_{e2}^{\max}$ for different ψ predicted by AMO. It is shown that the low- J attractor point tends to shift to $\cos\xi = 0$ as Q_{e2}^{\max} increases. Particularly, for $\psi = 89.9 \sim 90^\circ$, the low- J

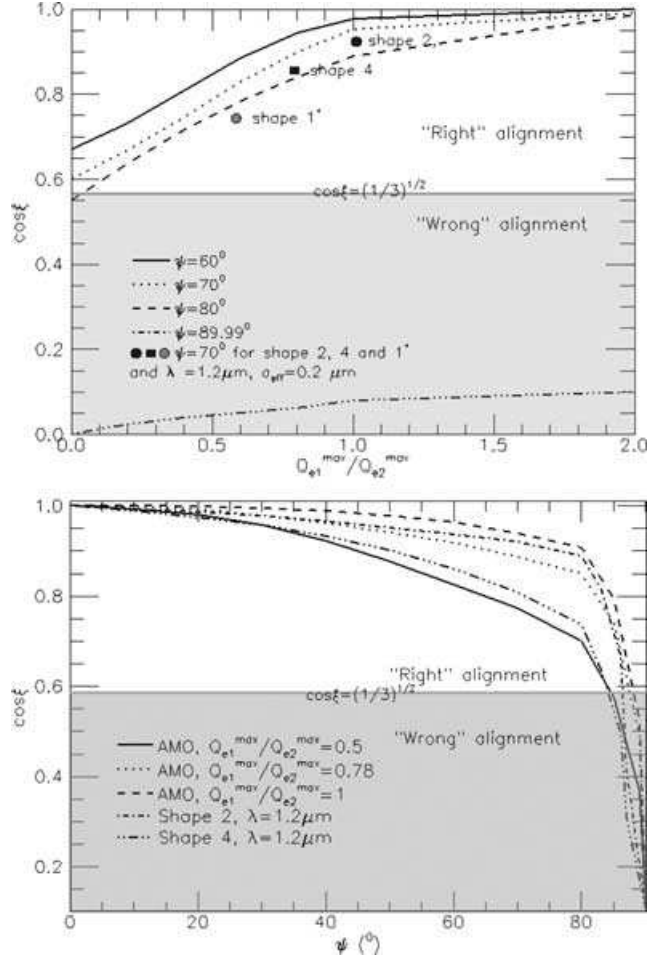


Figure 25. Upper panel: The shift of position of low- J attractor point as function of $Q_{e1}^{\max}/Q_{e2}^{\max}$ for different ψ . Lower panel: The shift of position of low- J attractor point with respect to ψ for AMO with three different ratios $Q_{e1}^{\max}/Q_{e2}^{\max}$ and for irregular grains. The shaded area corresponding to the degree of alignment $R = 1.5 \cos^2 \xi - 0.5 \leqslant 0$ shows the range of ‘wrong’ alignment.

attractor point coincides to $\cos\xi = 0$, that is, grains are aligned with long axes perpendicular to magnetic field. The above observed tendency is consistent with our earlier discussion in Section 6.4 that Q_{e2} acts to align grains perpendicular to \mathbf{B} .

Fig. 25 (lower panel) presents the shift as a function of ψ for AMO with different ratio $Q_{e1}^{\max}/Q_{e2}^{\max}$ of AMO and for irregular grains. It is clearly seen that the low- J attractor points for AMO and irregular grains are always at $\cos\xi = 1$ for $\psi = 0^\circ$, which means that no ‘wrong’ alignment possibility exists in this case. As ψ increases, they shift to $\cos\xi = 0$, and finally, fall on the perpendicular alignment angle $\cos\xi = 0$ at $\psi \sim 90^\circ$. For shape 4, however, the low- J attractor point can produce ‘wrong’ alignment earlier than for shape 2, that is, when $\psi \sim 85^\circ$. This is because shape 4 has the smaller ratio $Q_{e1}^{\max}/Q_{e2}^{\max}$ than shape 2.

We feel that $Q_{e1}^{\max}/Q_{e2}^{\max}$ provides a sufficiently good parametrization for torques of irregular grains. Therefore, in terms of practical calculations, establishing this ratio may be sufficient for describing the alignment of realistic irregular shapes. This would require much less computational efforts compared with obtaining the shapes for the entire range of Θ .

8 REGULAR CROSSOVER

The dynamics of AMO that we observed above was very different from that of grains in DW97. As we can see in Section 8, the properties of the RAT components are similar for AMO and irregular grains, including those studied by DW97. Therefore the difference stems from the different treatment of crossovers in our and the DW97 models.

The most striking difference between our and DW97 trajectory maps is that our crossover points correspond to $J = 0$ and grains cannot get out of these points. Therefore our crossover points are also the attractor points. Note that, unlike DW97, we do not observe cyclic maps. The latter are the artefact of their model of crossovers adopted there.

In what follows, we first discuss crossovers in the most general terms and later consider a particular case of a crossover which is not affected by thermal wobbling (cf. WD03). Then we briefly discuss the possible effects of thermal wobbling.

The crossover dynamics has two distinct regimes. The first one, described in Lazarian & Roberge (1997) takes place when the time of the crossover $t_{\text{cros}} \sim J_{\perp}/Q$ where J_{\perp} is the angular momentum component perpendicular to \mathbf{a}_1 (Spitzer & McGlynn 1979), that is, the time during which the grain undergoes a regular flipping subjected to the torque Q , is shorter than the time of internal relaxation t_{relax} . For H_2 torques Lazarian & Roberge (1997) obtained that this regime is fulfilled for grains larger than $a_c \sim 10^{-5}$ cm. When LD99b introduced nuclear relaxation it became clear that the typical critical size for interstellar grains $\sim 10^{-4}$ cm. This size depends on the value of the torques rather weakly, thus we may also accept it as the critical size of the grains in diffuse ISM in the presence of RATs. However, in the vicinity of really strong radiation sources the critical size gets smaller. Note that a_c is larger than the ‘typical’ a_{eff} in Table 2, but as we mentioned earlier, grains typical for diffuse interstellar gas are different from grains typical for other astrophysical environments.

The randomization of grains during a crossover happens due to random processes associated with atomic bombardment and H_2 formation. This is a random walk process in which the squared deviation in angular momentum $(\delta J)^2$ scales with the crossover time t_{cros} . Thus the deviation of the angular momentum in the process of a crossover scales as $\delta J/J_{\text{th}} \sim 1/J_{\text{th}} Q^{1/2}$. As $J_{\text{th}} \sim (kT_d I_1)^{1/2} \sim a_{\text{eff}}^{5/2}$ and assuming that Q is proportional to the cross-section $\sim a_{\text{eff}}^2$ (see Section 10), we get the deviation $\delta J/J \sim a_{\text{eff}}^{-7/2}$, which decreases quickly with the grain size. Therefore the assumption of *no randomization during crossovers* should initially be accurate for grains much larger than a_c . Such grains according to Cho & Lazarian (2005) are responsible for far-infrared polarization emanating from dark starless cores.

For grains smaller than the critical size a_c LD99a showed that the physics is different. As the angular momentum of a grain gets comparable with J_{th} , such grain wobbles fast due to coupling of rotational and vibrational degrees of freedom by the internal relaxation (see Lazarian & Roberge 1997). For H_2 torques this results in flipping that reverses the direction of torques and gets the grains ‘thermally trapped’ (see LD99a).

All in all, if grain dynamics is presented in the axes of J/J_{th} and $\cos \gamma$ with γ being the angle between \mathbf{a}_1 and \mathbf{J} , the assumption of $\mathbf{J} \parallel \mathbf{a}_1$ is accurate for $J/J_{\text{th}} \gg 1$. In the range of $J/J_{\text{th}} = [0, 1]$ the actual crossover physics should be accounted for.

In view of the discussion above, consider a regular crossover first, that is, assume that $a_{\text{eff}} \gg a_c$. The assumption that \mathbf{a}_1 is always parallel to \mathbf{J} breaks inevitably as $J_{\parallel} \rightarrow 0$. Indeed, whatever is the efficiency of the internal relaxation mechanism, there will be

some residual J_{\perp} . Lazarian & Roberge (1997) showed that the mean value of J_{\perp} during a regular crossover cannot be smaller than J_{th} . In addition, as J gets small, the efficiency of relaxation drops and the gaseous bombardment increases J_{\perp} further in accordance with the original Spitzer & McGlynn (1979) theory of crossovers.

To simplify our treatment we disregard all internal relaxation processes during the crossover. This is justifiable as for $a_{\text{eff}} \gg a_c$ the crossover happens on the time-scale shorter than the internal (e.g. nuclear) relaxation time. Since the mirror is assumed weightless, for AMO the dynamics of free rotation coincides with that of a spheroid. As a result, for a given J , \mathbf{a}_1 precesses around \mathbf{J} with a constant angle γ . The state of the grain is completely determined by describing \mathbf{J} in the lab and body systems. Equations of motion for this case are

$$\frac{d\mathbf{J}}{dt} = \Gamma - \frac{\mathbf{J}}{t_{\text{gas}}}, \quad (82)$$

$$\frac{J d \cos \gamma}{dt} = -\frac{dJ}{dt} \cos \gamma + \frac{dJ_{\parallel}}{dt}, \quad (83)$$

where Γ is RAT, and $J_{\parallel} = J \cos \gamma$ is the component of angular momentum along the maximal inertia axis. In the coordinate system J, ξ, ϕ , equation (82) returns to the set of equations of motion (65)–(67). Averaging over the angles, Φ and ϕ corresponding to the precession of \mathbf{a}_1 around \mathbf{J} and \mathbf{J} around \mathbf{B} , respectively, and solving three resulting equations for J, ξ, γ , we can obtain trajectory maps during the regime of low- J and regular crossover.

In Fig. 26 we show the phase map for the case $\psi = 30^\circ$. The most striking feature observed there is that the grain experiences not a single, but multiple crossovers. Unlike Purcell’s torques, as the grain flips, RATs do not change their direction. As a result, they drive J further down. In other words, the dynamics of grains roughly corresponds to what we observed in the earlier sections of the present paper (cf. DW97 where grains are spun up after passing $J = 0$).

Depending on magnetic field value, the crossover may happen on the time-scale smaller than the Larmor precession period. In this case, different grains will undergo crossovers at different ϕ and therefore will experience different torques during crossovers. However, this would not change the qualitative picture, as RATs will drive J to zero irrespectively of ϕ . We shall discuss this issue in more details elsewhere.

Let us consider qualitatively the issue of thermal fluctuations. For the Purcell’s torques those can be ignored during the crossovers for grains with size $a_{\text{eff}} \gg a_c$. RATs, however, are different. They tend to decrease J further rather than spin up the grains after a crossover. The time of relaxation, which is also the time over which thermal fluctuations of γ take place, increases as J decreases. Therefore in the absence of external collisions one can imagine two situations: according to one, RATs stop the grain completely, so no thermal wobbling of γ is possible, another is that J settles at the value that is of the order of J_{th} . The latter seems more probable for irregular grains.

An interesting consequence of the considerations above is that a grain tends to get to $J = 0$, but irregularities in the motion of the grain axes with respect to the photon flow prevents the angular momentum from reaching zero. Thus, we expect that for grains with moments of inertia closer to those of a spheroid, the value of angular momentum at the low- J attractor point is going to be smaller than that for more irregular grains.

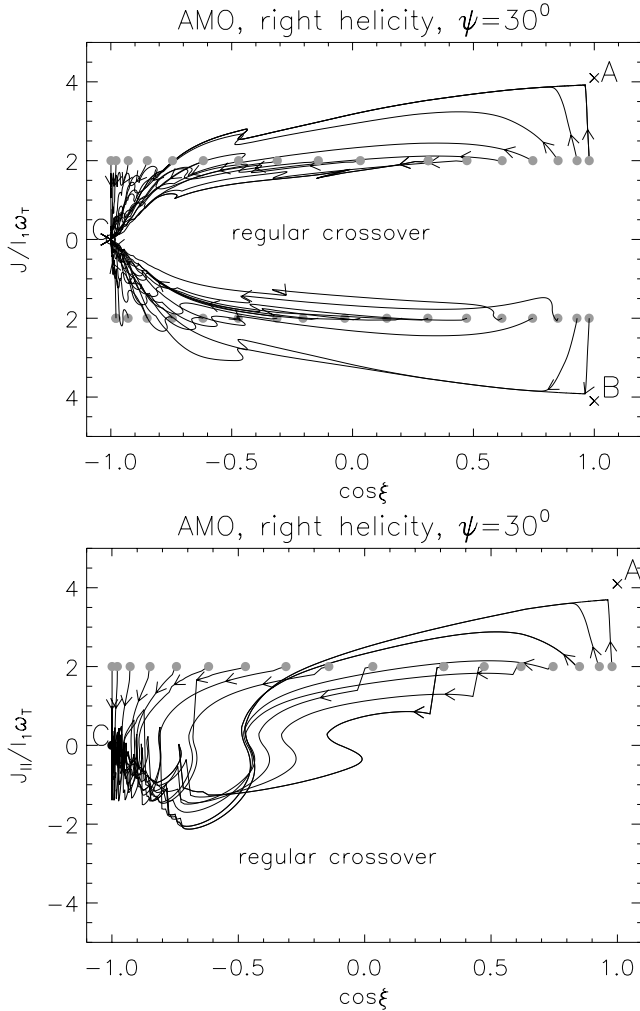


Figure 26. Phase maps for AMO with $\psi = 30^\circ$. Upper panel shows that all grains approach an attractor point C of $J = 0$ corresponding to the same angle $\cos \xi = -1$. However, regular crossovers corresponding to $J_{\parallel} = 0$ occur at different angles as illustrated by lower panel.

To find the actual value of effective J , one should recall that grains are subject to substantial random excitations in the typical astrophysical conditions. Gaseous bombardment, interactions with ions, absorption of photons (see Draine & Lazarian 1998 for a quantitative description of the processes), affects grain rotation at the low- J attractor point. We expect these influences to increase the mean value of J above J_{th} .

Another effect should also be present in the presence of random bombardment. If the phase maps have both high- and low- J attractor points, the bombardment allow more grains to get to a higher J attractor point. As low- J attractor points are characterized by higher internal randomization, quite counterintuitively, the random forcing can increase the degree of alignment.

All in all, our considerations above justify the simplified model of crossovers that we adopt in the paper. We shall provide a more detailed treatment in Hoang & Lazarian (in preparation).

9 PARTICULAR CASES

Our earlier discussion covered two limiting cases, namely, (i) the light beam being the axis of alignment, which corresponds to the

precession rate induced by RATs t_k^{-1} much larger than the Larmor precession rate t_B^{-1} and (ii) when the magnetic field constitutes the axes of alignment, that is, $t_B^{-1} \gg t_k^{-1}$. Can this case be ever astrophysically important?

9.1 Criterion for B alignment

Consider the precession of \mathbf{a}_1 or \mathbf{J} around \mathbf{k} driven by the component Q_{e3} which is perpendicular to the axes \mathbf{a}_1 and \mathbf{k} . The time-scale for RAT precession is defined by

$$t_k = \frac{2\pi}{|\mathbf{d}\phi/dt|} = \frac{10^{11}}{\hat{Q}_{e3}} (\hat{\rho} a_{-5} \hat{T})^{1/2} \left(\frac{1}{\hat{\lambda} \hat{u}_{\text{rad}}} \right) \text{s}, \quad (84)$$

where

$$\frac{d\phi}{dt} = \frac{\lambda a_{\text{eff}}^2 \gamma}{I_1 \omega} \mathbf{Q}_{\Gamma} \cdot \hat{\Phi} = \frac{\lambda a_{\text{eff}}^2 \gamma}{I_1 \omega} Q_{e3}. \quad (85)$$

Here ω is the angular velocity of a grain around the maximal inertia axis \mathbf{a}_1 . $\hat{Q}_{e3} = Q_{e3}/10^{-2}$, $\hat{\lambda} = \lambda/1.2 \mu\text{m}$, $\hat{u}_{\text{rad}} = u_{\text{rad}}/8.64 \times 10^{-13} \text{ erg cm}^{-3}$, and $\hat{\rho} = \rho/3 \text{ g cm}^{-3}$, $a_{-5} = a_{\text{eff}}/10^{-5} \text{ cm}$ and $\gamma = 0.1$ for anisotropy of ISRF. In deriving equation (84) the assumption $\omega = \omega_T$ is used. It is easy to see that for axisymmetric grain shapes, Q_{e1}, Q_{e2} are equal to zero, while Q_{e3} is non-zero (see equations 4–6). Therefore, the third component produces fast precession of grains about \mathbf{k} .

The precession rate above should be compared with the Larmor precession rate. A rotating grain acquires a magnetic moment by the Barnett effect which is shown to be much stronger than that arising from the rotation of its charged body (Dolginov & Mytrophanov 1976). The interaction of the magnetic moment with the external magnetic field causes the gradual precession of the grain around the magnetic field direction. The rate of Larmor precession around magnetic field, t_B , is given by

$$t_B = 3 \times 10^7 a_{-5} \hat{\rho}^{-1/2} \hat{\chi}^{-1} \hat{B}^{-1} \text{s}, \quad (86)$$

where $\hat{B} = B/5 \mu\text{G}$, $\hat{\chi} = \chi/3.3 \times 10^{-3}$ are normalized magnetic field and magnetic susceptibility, respectively.

The alignment of grains whether with the radiation or magnetic field depends on their precession rate around these axes. According to equations (84) and (86), the ratio of precession rate due to radiation and magnetic field is given by

$$\frac{t_k}{t_B} = \frac{3.33 \times 10^3}{\hat{Q}_{e3}} \hat{\rho} \hat{\chi} \hat{T}^{0.5} a_{-5}^{-1.5} \left(\frac{\hat{B}}{\hat{\lambda} \hat{u}_{\text{rad}}} \right). \quad (87)$$

It can be easily checked that for typical diffuse ISM, $t_B/t_k \sim 10^{-3}$, that is, the Larmor precession is much faster than precession induced by radiation, therefore magnetic field is the alignment axis.

For AMO, RATs can be very different as Q_{e3} arises from a spheroidal shape, while the other two components arise from a mirror; the ratio of the sizes of the mirror and the spheroidal body may be arbitrary. For irregular grains, however, we can see all three RAT components to be roughly comparable (see Figs 6–8). In this case, t_k can be used as a proxy for the time of ‘fast alignment’ (see Section 9.3).

9.2 Astrophysical implications

It is possible to estimate that for the magnetic field of $5 \mu\text{G}$ grains get aligned with the radiation beam when the density of energy in a beam is $u_{\text{rad}} > 10^3 u_{\text{ISRF}}$. The appropriate radiation fields is typical near-stars and supernovae.

Fig. 27 shows the variation of the ratio of precession time-scales with distance for different stars in which we use $Q_{e3} = Q_{e3}^{\max}$ (for

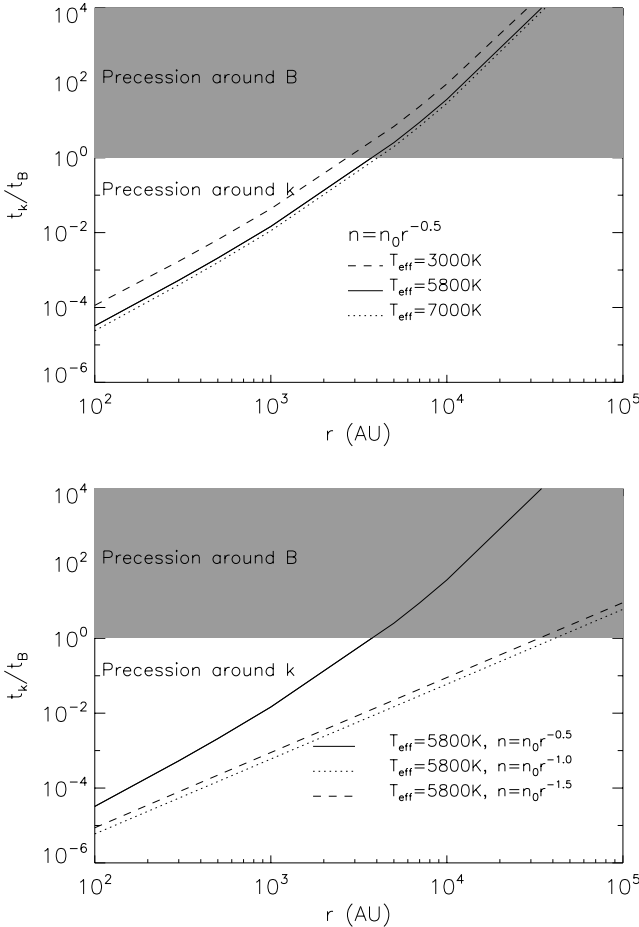


Figure 27. The ratio of time-scales for the precession about the light direction and about the magnetic field assuming that magnetic field is homogeneous with strength $B = 0.5 \mu\text{G}$ through envelopes. Upper panel: For three values of star temperature, the density dependence on the distance from the star is fixed. Lower panel: For a given star with different functions of density.

shape 1 and ISRF) for equation (87). It is apparent that near the stars, grains precess around \mathbf{k} much faster than around magnetic field. However, the ratio increases with distance as the radiation field decreases, so the precession around magnetic field is faster than around light, and grains align with magnetic field at some distance.

Another case when the alignment can happen with respect to the direction of light is the case of cometary dust. This case may be somewhat more complex, as electric field can be present near the comet head. This can induce precession of grains with dipole electric moment and therefore provide yet another axis of alignment. We discuss this problem in Hoang & Lazarian (in preparation).

If t_k^{-1} and t_B^{-1} are comparable, the axis of alignment does not coincide with either beam or \mathbf{B} . This case can be relevant to some part of comet grains, but a discussion of it is beyond the scope of the present paper.

Note that t_k^{-1} is a function of Θ . Therefore when its amplitude value is larger than t_B^{-1} this does not guarantee that the effect of magnetic field is negligible. For AMO the alignment drives grains into the position corresponding to $\Theta = \pi/2$, for which the component Q_{e3} gets zero and therefore the magnetic field again dominates. Thus the alignment is expected with respect to an intermediate axis. This may be important for explaining circular polarization arising from comets (Rosenbush et al. 2007). Naturally, not only precession

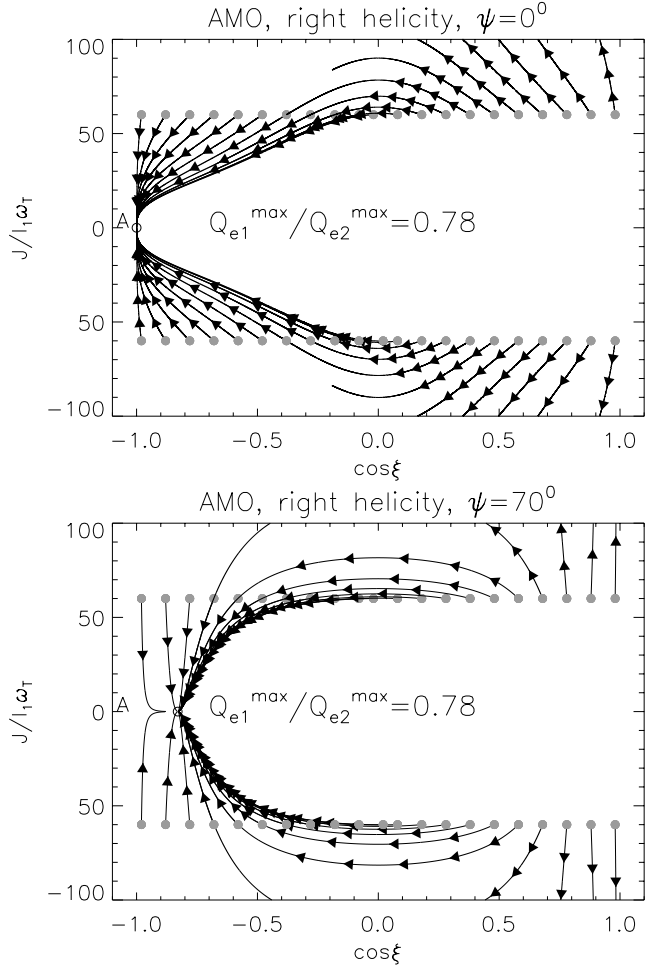


Figure 28. Alignment in the absence of gas damping for two directions of radiation $\psi = 0^\circ$ (upper panel) and 70° (lower panel). Here, the grey circles represent the initial position of grains. In the upper and lower panels, the distance between two filled arrows corresponds to a time interval $\Delta t = 10$ and $50t_k$, respectively.

arising from magnetic field, but also from electric field and mechanical torques (see Section 11.4) should be taken into account for that case.

9.3 Fast alignment

In this section we ignore the damping role of the ambient gas, and show that grains can be aligned by radiation on a time-scale shorter than the gas damping time. Such alignment can be called ‘fast alignment’ in analogy with the ‘fast dynamo’ process (see Vishniac, Lazarian & Cho 2003, and references therein) that can amplify magnetic field on the time-scales shorter than the magnetic diffusion time. In particular, supernova flashes can align grains around them with respect to the direction of light (see Section 6).

In Fig. 28 (upper panel) we show the map for $\psi = 0^\circ$ in which the distance between two arrows represents a time interval equal to 10 precession time t_k that is defined in equation (84). It can be seen that the grains that have initial orientations close to the attractor point A require alignment time-scales t_{phot}^{13} is approximately $40t_k$

¹³ t_{phot} is defined as the alignment time-scale of grains due to photon or radiation.

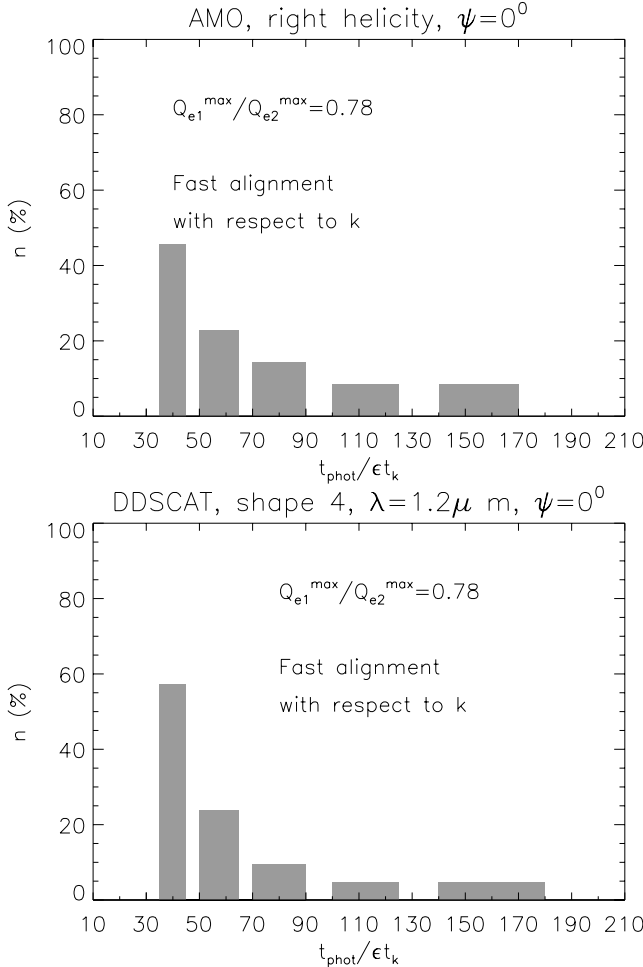


Figure 29. Percentage of grains as function of the ratio of the alignment time-scale due to photon, namely, t_{phot} to the precession time about the radiation direction, t_k , for AMO with $Q_{e1}^{\max}/Q_{e2}^{\max} = 0.78$ (upper panel) and shape 4 (lower panel). Here $\epsilon = \frac{Q_{e1}^{\max}}{Q_{e3}^{\max}}$, which is chosen to be equal to unity for AMO, and $\epsilon \sim 1$ for shape 4.

to get aligned (see Fig. 28, upper panel). In contrast, grains that have initial angles far away from the attractor point need more time (up to $\sim 160 t_k$) to get there (see Fig. 29).

Fig. 28 (lower panel) shows a similar effect for the case $\psi = 70^\circ$. However, the interval of two arrows represents a time interval $\Delta t = 50 t_k$. The map shows that grains bound to the low- J attractor point A reach it fast, about $70 t_k$, that is, on the time-scales much less than the rotational damping time. Some grains that otherwise would go to the high- J attractor point stream to infinite J in the absence of damping (lower panel).¹⁴ In practical terms the latter fact for this regime (i.e. alignment time-scale $t_{\text{phot}} < t_{\text{gas}}$) is not so important, as most grains get aligned at the low- J attractor points anyhow. We also observe the shift of low- J attractor point A as in the upper panel of Fig. 25.

The corresponding time for the fast alignment is proportional to ratio of grain angular momentum and the component of the torque

¹⁴ We may observe that phase trajectories in Fig. 28 (lower panel) directed to high- J attractor points also correspond to the aligned state of grains, although the stationary state requires t_{gas} to be achieved. In this sense all grains get aligned fast.

Γ_{rad} . In terms of RATs normalized components Q_Γ that is related to Γ_{rad} via equation (1) the relevant combination is given by equation (84). The corresponding function F depends only on Q_{e1} and Q_{e2} . The amplitudes of those can be very different from the component Q_{e3} that causes the grain precession. Therefore for such grains, the ratio of $J/\Gamma_{\text{rad}} \propto J/F$ can be measured in units of ‘the period of radiation-induced precession’, namely, in $t_k \propto J/Q_{e3}$ (see equation 84). To make AMO more correspond to irregular grains in this respect, we choose the amplitude of the AMO components Q_{e3} to be similar to the amplitude of Q_{e1} .

Histograms showing the distribution of grains on the low- J attractor point as a function of alignment time-scale corresponding to AMO and an irregular grain shape 4 are shown in Fig. 29. It can be seen that, for AMO, about 45 per cent grains get aligned with respect to k over $t_{\text{phot}} \sim 35$ to $45 t_k$, and about 22 per cent of grains get there over $t_{\text{phot}} \sim 50$ to $65 t_k$. A few per cent of grains require longer time to get aligned, up to $170 t_k$ (see Fig. 29, upper panel). This relative inefficiency of alignment is a consequence of small amplitude of the function F in the vicinity of the low- J attractor points ($F = 0$ at the stationary points). On the other hand, for shape 4, Fig. 29 (lower panel) shows that about 55 and 21 per cent of grains get aligned with k over 35 and $65 t_k$, respectively. Some others can get aligned over $170 t_k$. We see that the similar distribution of grains as functions of alignment time between shape 4 and AMO, though the slight difference in percentage of grains corresponding to each t_{phot}/t_k present due to the fact that, their functional forms of their torques are not completely the same.

Fast alignment happens with respect to magnetic field provided that $t_B < t_k$ (see equation 87), but $t_{\text{phot}} < t_{\text{gas}}$. The ratio $t_{\text{gas}}/t_B = 1.2 \times 10^5 (\frac{\hat{\rho}^{3/2} \hat{B} \hat{X}}{\hat{n} \hat{T}_g^{1/2}}) a_{-5}^{-1}$ which provides a substantial parameter space if t_{phot} is much larger than t_k , for example, $t_{\text{phot}} \sim 10^2 t_k$. Comparing t_{gas} in Table 2 and t_k given by equation (84) we may conclude that for typical grains in diffuse interstellar gas t_{gas} is marginally smaller than t_{phot} and therefore the grain phase trajectories are still determined by t_{gas} . However, closer to stars t_{phot} provides the measure of the characteristic time of alignment.¹⁵

10 FITTING FORMULAE FOR RATS

Astrophysically motivated situations require calculations of RATs for grains of different sizes and at many wavelengths. This requires rather intensive numerical computations. Our encouraging results with AMO motivate us to consider whether we can predict the scalings of torques.

Dolginov & Mytrophanov (1976) associated RATs with the scattering of right- and left-handed photons by a grain. For this model one should conjecture that amplitude of RATs decreases rapidly with increasing λ/a_{eff} as the grain–photon interactions get into the random walk regime. In other words, a sharp peak is expected for the torque efficiency for photons with $\lambda \sim a_{\text{eff}}$. AMO, on the contrary, suggests of a linear increase for $\lambda \ll a_{\text{eff}}$. Our computation, however, indicates that RAT gets constant for $\lambda < a_{\text{eff}}$. However, both computational and DDSCAT intrinsic limitations do not allow us to perform calculations for $\lambda/a_{\text{eff}} < 0.1$. More studies with other techniques, for example, ray-tracing one, are necessary.

¹⁵ We see that the alignment times are more than $30 t_k$. This is due to the fact that the aligning torque gets weaker near the low- J attractor points (see Fig. 18, upper panel).

For grains with $\lambda \gg a_{\text{eff}}$, Lazarian (1995) suggested that the scaling of RATs efficiency should be $\sim (\lambda/a_{\text{eff}})^{-4}$. Such considerations disregard the variations of the optical constants. Therefore the testing is essential.

We calculated RATs in function of λ/a_{eff} for three grain shapes. Shapes 1 and 2 are shown in Fig. 4, and a hollow grain is produced from shape 1 by removing the core of grain. The latter is done to reduce the amount of necessary DDSCAT computations while achieving smaller λ/a_{eff} ratios.

We use both the dielectric function for the smoothed astronomical silicate (DW97; Weingartner & Draine 2001; Cho & Lazarian 2005) and constant refractive index. Results are shown in Figs 30 and 31.

We see that the approximate self-similarity (i.e. the dependence on λ/a_{eff}) is an intrinsic property of RATs. When optical constant changes as a function of wavelength, RAT efficiencies for different grain sizes mostly differ at wavelengths corresponding to resonance absorption features.

In addition, RATs have nearly constant magnitude as $\lambda \sim a_{\text{eff}}$, and decrease steeply with the ratio of wavelength to grain size. This is because the scattering of photon by irregular grains is the strongest as $\lambda \sim a_{\text{eff}}$. We can fit our calculations for RATs (see Figs 30, 31)

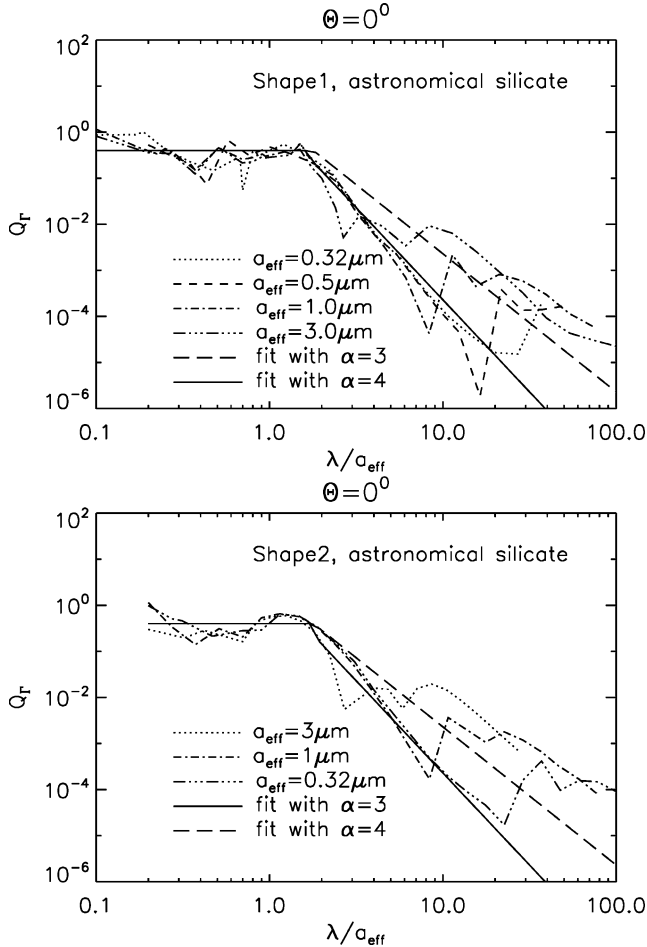


Figure 30. Upper panel: RATs for grain shape 1, as the function of wavelength to grain size for the direction $\psi = 0^\circ$. We see that RATs decrease steeply as λ/a_{eff} increases. Around $\lambda/a_{\text{eff}} \sim 1$ the dependence flattens. Several positions at which RATs decrease dramatically correspond to the peculiarities of dielectric susceptibility. If those peculiarities are ignored, RATs are self-similar. Lower panel: The same as the upper panel but for shape 2. RATs can be fitted by analytical functions with $\eta = 3$ or 4 (see equation 88).

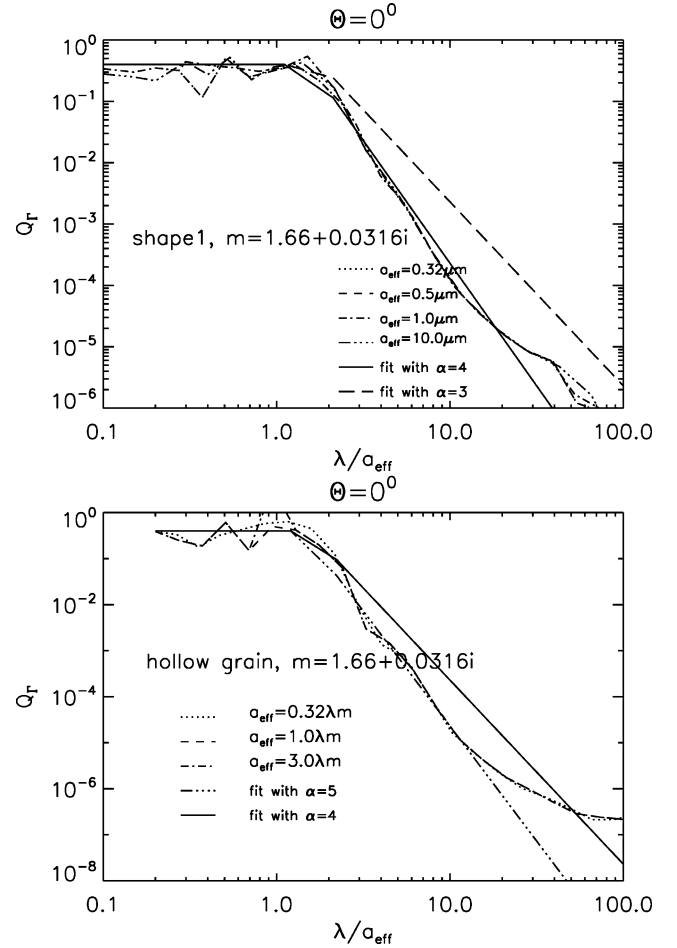


Figure 31. RATs for shape 1 and hollow grain with constant refractive index: self-similarity exhibits extremely well. They can be fitted by a step function and a power function with $\eta = 3, 4$ (upper panel) and $\eta = 4, 5$ (lower panel) where η is defined in equation (88).

by a simple function given by

$$Q_\Gamma = 0.4 \text{ for } \frac{\lambda}{a_{\text{eff}}} < 1.8, \\ = 0.4 \left(\frac{\lambda}{a_{\text{eff}}} \right)^{-\eta} \text{ for } \frac{\lambda}{a_{\text{eff}}} > 1.8, \quad (88)$$

where α is the spectral index that according to Figs 30 and 31 is between 3 and 4. The first case provides a good fit in the whole range of λ/a_{eff} . In contrast, the latter case gives better fit for the range of $\lambda/a_{\text{eff}} < 20$. Cho & Lazarian (2006) use the former fit formulae to calculate polarization degree for accretion discs because the grains there are widely believed to be very large.

For the case when a_1 makes an angle $\Theta = 45^\circ$ with respect to k , we found that the self-similarity is also valid. However, the curve of RATs is shallower, and can be fitted by a power index $\eta = -2$.

To study the efficiency of the self-similarity, we calculate rotation velocity of grains induced by RATs in which RATs are directly computed from DDSCAT and derived from the self-similarity assumption. We use radiation intensity of a molecular cloud (see Mathis, Mezger & Panagia 1983) to calculate RATs for different optical depths A_v . Resulting rotation speed obtained with these two methods (see Fig. 32) shows clearly that the self-similarity provides a fair agreement between exact calculations and those based on the

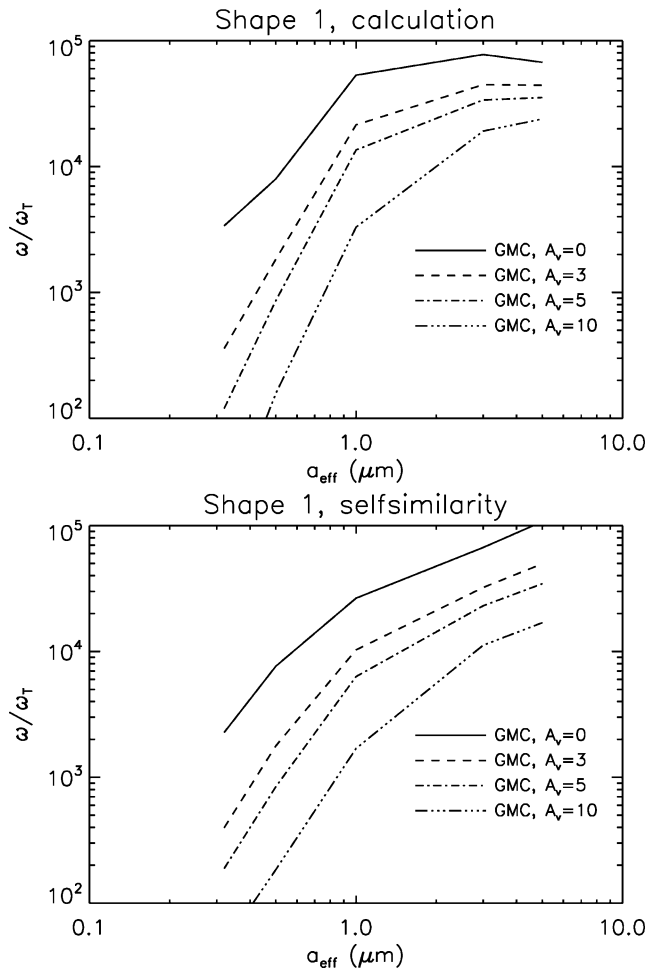


Figure 32. Ratio of rotation speed to thermal rotation speed with respect to grain size obtained with exact RATs from DDSCAT (upper panel) and using the self-similarity (lower panel). Here, radiation direction is assumed to be parallel to the maximal inertia axis a_1 that is constrained to be frozen to angular momentum \mathbf{J} . The figures show the rapid increase of the rotational speed with grain size, and even in the cloud core with high visual extinction $A_v = 10$, large grains still have suprathermal rotation rate, ensuring that grain alignment is not susceptible to random collision by atomic gas.

self-similarity arguments. This allows us to reduce the DDSCAT computational efforts substantially.

11 DISCUSSION

Our study above has approached an important problem of the RAT alignment mechanism by studying the fundamental properties of RATs. The goal of such studies was to change the status of the RAT alignment from an empirical fact to a theoretically understood process. Our work indicates that grain helicity is an essential property of realistic grains, which suggests that it should be accounted not only for RATs, but also for mechanical alignment as well.

11.1 Evolution of ideas on RATs

For the first time grain spin-up due to differential scattering of left- and right-handed photons was considered in Dolginov (1972). The suggestion was limited to quartz grains, however. In Dolginov & Mytrophanov (1976) it was realized that grains made of more ac-

cepted astrophysical materials can be spun up, provided that they are somewhat twisted. This ground-breaking study qualitatively considered both the possibility of the RAT alignment with respect to magnetic field and the radiation beam. Regretfully, it was not appreciated in its time.

A reason of the lukewarm response of the community to this work was probably related to both the absence of reliable estimates of RAT efficiencies and to the fact that some features of grain dynamics were unknown at that time. For instance, Dolginov & Mytrophanov (1976) claimed that prolate grains should align along magnetic field, while oblate grains should align perpendicular to magnetic field. The former conclusion was based on the assumption that grain rotation along the axis of minimal inertia is stable. It is only later that Purcell (1979) discovered so-called Barnett relaxation and concluded that only rotation about the axis of maximal inertia is stable.¹⁶ On the basis of this Lazarian (1995) claimed that the alignment of both prolate and oblate helical grains should happen with long axes perpendicular to magnetic field. However, it was not quite clear at that moment what makes the grain helical. In addition, Lazarian (1995) underestimated the importance of the RAT alignment.

The quantitative stage of RAT studies was initiated by Draine & Weingartner (DW96 and DW97). There RATs were shown to be generic for irregular (and therefore realistic) grains and the magnitude of RATs was reliably quantified. The alignment with respect to magnetic field was demonstrated in numerical simulations. On the basis of these simulations DW97 claimed that the RAT alignment was the dominant process responsible for polarization arising from dust in the diffuse ISM. However, the RAT alignment was an empirical fact in DW97 that was based on a limited sample. In this situation additional important complexities arising from including thermal wobbling of grains (WD03), gaseous bombardment, etc. could not help to improving our physical understanding of the RAT alignment.

What we have done in the present paper is that we attempted to clarify the basics of the RAT alignment by seeking the generic properties of RATs that induce the alignment. We used analytical modelling which was tested with numerical DDSCAT simulations. As we discuss further, we hope that this work contributes to both more intuitive understanding of the alignment and to further elaborating of the mechanism in order to get precise predictions of the alignment degree in different astrophysical situations.

It is worth mentioning that even when we know the analytical form of the torques, the dynamics of the system does not get completely trivial. It definitely exhibits interesting properties.

11.2 Our approach

While RATs were initially treated as a quantum effect arising from the difference of scattering of left- and right-handed photons (see Dolginov & Mytrophanov 1976), above we presented an entirely classical model of a grain (see Fig. 2) that reproduces well their properties (see Fig. 5).

The gist of our approach above is to consider the basic generic properties of RATs and to relate these properties with the RAT alignment. AMO plays a central role in our considerations. Our toy model of a helical grain allowed an analytical description, which enabled us to treat RATs analytically. In our study we concentrated on the properties of RAT components in the scattering system (see Fig. 1), that

¹⁶ The Barnett magnetization that induced Ed Purcell to think about the relaxation was described in the same Dolginov & Mytrophanov (1976) paper.

is, on the properties of Q_{e1} , Q_{e2} and Q_{e3} . These components show a remarkable similarity for grains of very different shapes (see Fig. 8) and AMO (see Fig. 5). The χ^2 test we present in Section 4.5 returns the mean value of χ^2 for both Q_{e1} and Q_{e2} about 0.2 (see Fig. 10). This provided us with the empirical justification of using AMO for studies of RAT alignment. AMO provides us with both useful intuitive model to think about the alignment and analytical formulae that allow straightforward quantitative calculations.

We find that the basic properties of RATs obtained with AMO are very similar to the those of RATs for arbitrary shaped grains. This, for instance, allows us to talk about helicity of grains being the most important attribute for the RAT alignment.

Our major goal above was to get a better understanding of the physics of the RAT alignment. To do this we adopt a model, similar to one in DW97, which disregards the wobbling of the grain axes with respect to angular momentum direction (cf. Lazarian 1994; Lazarian & Roberge 1997; LD99ab), but treats crossovers differently, that is, in the spirit of the Spitzer & McGlynn (1979) model. This provides a substantial change in the dynamics of grains. For instance, we do not observe cyclic maps reported in DW97.

While studying the properties of RATs we addressed the question of the necessary conditions for RAT alignment to happen and to fail. We also study the RAT alignment that takes place in the radiatively-dominated environments, where the direction of radiation defines the axis of alignment (see Dolginov & Mytrophanov 1979; Lazarian 2003). Such an alignment is both astrophysically important and provides a good insight into the physics of the RAT alignment.

11.3 Accomplishments and limitations of the present study

We feel that our major accomplishment in the paper above was establishment of the analytical form of RATs and clarification of the role of different RAT components. We hope that AMO unveils the mystery that have surrounded the RAT alignment from the time of the mechanism introduction.

Another important conclusion that follows from AMO is that the RAT alignment is not limited to grains with $\lambda \sim a_{\text{eff}}$, as it was believed before. As the similarities between the torques that we obtained for AMO in the $\lambda \ll a_{\text{eff}}$ limit and for irregular grains in the $\lambda \geq a_{\text{eff}}$ limit are striking, our work shows that the RAT alignment should take place also for large grains, which are present in accretion discs and dark cloud cores (see Cho & Lazarian 2005, 2007).

Obtaining generic properties of RATs makes the RAT alignment more a predictable theory and opens avenues for further theoretical advances, for example, including thermal fluctuations, random bombardment, H_2 torques, etc. Our establishing of a subdominant nature of one of the RAT components, namely Q_{e3} , simplifies the theoretical treatment of RATs. Insights into the generic properties of two other components allow us to reduce the amount of numerical computations necessary to determine the degree of achievable alignment. For instance, in the current paper, we found that the existence of high- J attractor points depends on the $Q_{e1}^{\max}/Q_{e2}^{\max}$ ratio. For practical applications, it is important that the criterion for this established with AMO works well with irregular grains. We note parenthetically that while Q_{e1} and Q_{e2} demonstrate universal behaviour, the aligning and spinning torques (see equations 68 and 69) that present their combinations do not demonstrate this.

The present study identifies a parameter space for which the RAT alignment may be suspected to be ‘wrong’, that is, to happen with

long axes parallel to magnetic field. In addition, it provides simple scalings for RAT dependences on the ratio of the radiation wavelength to the grain size.

Our study reveals new properties of the RAT alignment. First of all, the alignment may be fast, that is, happen in a small fraction of gas damping time (see Section 9.3). This has important consequences for the environments with fast changing radiation, that is, circumstellar regions, ISM in the vicinity of supernova flashes, etc. Moreover, we could see that the alignment is different depending whether the initial angular momentum is small or large (see Figs 22 and 23).

The approximate self-similarity of RATs (see Section 10) is another practically useful property of RATs. Combined with the established universality of the functional form of the components Q_{e1} and Q_{e2} and the established dependences of the properties of trajectory maps on the ratio of these components, this allows us to radically reduce the DDSCAT calculations that may be necessary to find the expected degree of alignment for an ensemble of realistic grains subjected to a realistic radiation field. In fact, we find that RATs change the ratio of $Q_{e1}^{\max}/Q_{e2}^{\max}$ with λ and this is the most important difference that the variation of the radiation wavelength entails. The functional forms of the torques do not change much and can be well approximated with those of AMO.

One limitation of AMO is the upper limit of the ratio $Q_{e1}^{\max}/Q_{e2}^{\max}$, which makes AMO more appropriate to irregular grains with $\lambda > 3 a_{\text{eff}}$ and $\lambda < a_{\text{eff}}$. It indicates that, though AMO is established based on the geometric optics, that is, $\lambda \ll a_{\text{eff}}$, it is also applicable for the opposite limit.

In more general terms, our study proved that irregular grains can be characterized by helicity. Grain rotation provides the averaging that defines the helicity axis, while the irregularities define whether the helicity is left- or right-handed. The phase trajectories of grains that are the mirror symmetric images of each other are mirror symmetric (see Fig. 13). As expected, the torque component Q_{e3} , unlike the other two components, coincide for an irregular grain and its mirror symmetric image (see the lower panel in Fig. 8). Indeed, this component is subdominant for most of the alignment processes and not related to grain helicity.

In our study we do not directly address the grain alignment efficiency. Some statements can be made, however. For instance, when grains are aligned rotating suprathermally the direction of \mathbf{J} is immune to the randomization arising from the gaseous bombardment. In addition in this case, $\mathbf{J} \parallel a_1$ provides a good approximation. We find, however, that an appreciable subset of grains rotates with thermal velocities. For those the internal randomization of grain axes with respect to \mathbf{J} may be important. Does this signify a new crisis of the grain alignment theory? We do not believe so. Even in the absence of high- J attractor points RATs will drive \mathbf{J} back to low- J attractor points, which in most cases, as we discussed in the paper, correspond to the preferential alignment of grains with long axes perpendicular to magnetic field. As for the internal alignment, according to Roberge & Lazarian (1997) for typical interstellar grains, this alignment is tangible even for $J \sim J_{\text{th}}$. A detailed study of the attainable degrees of alignment is provided elsewhere.

We have not discussed RATs of the strongly absorbing materials, for example, graphite. We expect the torque components to show more irregularity for such grains. As the grain alignment theory matures and extends to the environments different from molecular clouds and diffuse interstellar gas (see Lazarian 2007), the importance of the studies of wider range of materials will get more pressing.

11.4 Rates of alignment and rotation

As we mentioned above the RAT alignment can happen on time-scales much shorter than the gaseous damping time. This finding corresponds to the notion in Dolginov & Mytrophanov (1976) that the alignment happens on the time-scale that is required for the RATs to deposit a grain with the angular momentum of the order of its initial angular momentum. Such a fast alignment makes grains good tracers of magnetic field when radiation direction changes quickly.

The fast alignment takes place for low- J attractor points of the grain phase trajectory map. These are the most probable attractor for the grains to end up with. Thus, most grains do not rotate suprathermally when subject to RATs. In this sense the RAT alignment tends to minimize grain angular momentum.

While we expect that in the presence of thermal wobbling and gaseous bombardment most grains will rotate thermally, there is a radical difference between this effect and the effect of thermal trapping discussed in LD99ab. The effect of thermal trapping is based on the compensation of the Purcell rocket torques, for example, those related to H₂ formation, by thermal flipping of grains. The more efficient the thermal flipping, the more efficient is the trapping and the less chance of a grain to get high angular momentum. On the contrary, we have seen in Sections 6 and 7 that without thermal wobbling, the significant fraction of grains ends up in the state of $J = 0$. In other words, thermal fluctuations increase the value of J to a *higher*, that is, thermal value.

In spite of the fact that most of the grains tend to rotate with velocities much less than the maximal velocities, ω_{\max} , that RATs can spin the grain up, we believe that the parametrization of the alignment in terms of ω_{\max}/ω_T , where ω_T is the thermal rotational velocity, may be a rough practical way of describing alignment. Indeed, the above ratio reflects the relative importance of RATs compared with those related to gas. When RATs force the grain into a low- J attractor point, their ability to do this would also depend on this ratio. A further research should reveal more sophisticated and precise parametrization of the RAT alignment, however. This parametrization is necessary, for instance, to predict the expected alignment from the numerical simulations of magnetized molecular clouds (see Cho & Lazarian 2005; Bethell et al. 2007; Pelkonen et al. 2007).

We have discussed in Section 7.5 that for some phase trajectories high- J attractor points are available. The suprathermally rotating grains correspond to high- J attractor points. It takes them about three damping times to reach such points (see also DW97). However, our analysis shows that grains get aligned even before they reach high- J attractor points. Therefore the RAT alignment can happen over shorter time-scales for all grains provided that the radiation is intensive enough.

The predominance of low- J attractor points has consequences that go beyond the problems of grain alignment. If grains rotate slowly, then loosely connected conglomerates constituting fractal grains can exist. Ever since the classical work by Purcell (1979), the suprathermal rotation had been thought to destroy such grains. When LD99ab showed that Purcell's torques may not be capable to spin up grains less than 10⁻⁴ cm, it was still thought that RATs can do the job. Our work questions this (see also WD03).

11.5 Direction of alignment

The alignment may happen with respect to radiation rather than to magnetic field if the precession induced by RATs is faster than the Larmor one (see Section 9). We found that in the presence of

magnetic field the alignment can still happen with respect to the direction of the beam or, equivalently, the direction of the anisotropy of radiation, provided that the rate of precession arising from the RATs is faster than rate of the Larmor precession. This is the case of comets sufficiently close to the Sun, ISM in the vicinity of supernovae and some circumstellar regions. Over vast expanses of diffuse ISM and molecular clouds, however, the generic RAT alignment is with respect to magnetic field, thus enabling easy tracing of magnetic fields via polarimetry. Note that our study shows that many features characteristic of the alignment in the absence of magnetic field carry over to the case when magnetic field is present.

Our important finding is that while the generic alignment is 'right', that is, with the long grain axes perpendicular to magnetic field, for a range of angles ψ between the magnetic field and the direction of the beam around $\psi = \pi/2$, the alignment may be 'wrong', that is, it happens with long grain axes parallel to magnetic field. However, the range of the angles is rather narrow. As a result, we do not expect the effect of 'wrong alignment' to persist when grains undergo thermal wobbling. This wobbling is likely to vary the direction of the grain axes with respect to the light direction beyond the range angles in which the alignment is 'wrong'.

11.6 Magnetic field and gas streaming

Unlike DW97, in this paper we disregarded the effects of paramagnetic alignment altogether. When we consider dynamically important field, its only effect is to induce averaging due to Larmor precession. We believe that our approach is correct, as for paramagnetic grains the effects of paramagnetic relaxation are marginal on times over which the RAT alignment takes place.

Gas streaming can induce its own alignment direction. Dolginov & Mytrophanov (1976) assumed that magnetic field or a gaseous flow defines the axis of alignment depending on the ratio of Larmor precession time to that of mechanical alignment. On the basis of our study of Q_{e3} with AMO, we believe that a more physically motivated distinction is related to the rate of Larmor precession versus the precession arising from the mechanical analogy of the Q_{e3} torque. Such torque for a spheroidal grain can be obtained from formulae in Appendix B by substituting the value of the gas atom momentum mv instead of the photon momentum. The corresponding precession time-scales ratio is (see equation 85)

$$\frac{t_{\text{flow}}}{t_B} = 3 \times 10^5 \frac{\hat{\alpha} \hat{\chi} \hat{T}^{-0.5} \hat{a}_{-5}^{-0.5}}{\alpha \hat{v}_{\text{flow}}^2 \hat{n}_H} \frac{\hat{B}}{\hat{Q}_{e3,\text{gas}}}, \quad (89)$$

where $\hat{Q}_{e3,\text{gas}}$ is the third component of torques induced by the gaseous flow, which is the analogue of Q_{e3} for RATs. In equation (89), $\alpha = \hat{\alpha} \times 0.1$ is the probability of elastic collision, $v_{\text{flow}} = \hat{v}_{\text{flow}} \times v_{\text{thermal}}$ is gas flow velocity, $n_H = \hat{n}_H \times 30$, $T = \hat{T} \times 100$ is gas density and temperature, respectively. Equation (89) indicates that for sufficiently intensive gaseous flows, for instance, $\hat{v}_{\text{flow}} > 10^2$, the alignment will indeed happen with respect to the flow direction. Note that we predict that gaseous flows may define the direction of alignment for a wider parameter range compared to that in Dolginov & Mytrophanov (1976). Moreover, we claim that mechanical flows can define the axis of alignment even for subsonic flow velocities, that is, at those velocities for which the Gold alignment and its modifications (cf. below, however) are marginal.

A conceivable situation is that the gaseous bombardment arising from grain streaming defines the axis of alignment, while RATs do the alignment job. This situation takes place when $Q_{e3,\text{RATs}}$ is less

than $Q_{e3,\text{gas}}$, which defines

$$\frac{t_{\text{flow}}}{t_k} \sim \frac{u_{\text{rad}}}{\alpha m_{\text{H}} v_{\text{flow}}^2 n_{\text{H}}} \sim 10^1 \frac{\hat{u}_{\text{rad}}}{\hat{\alpha} \hat{v}_{\text{flow}}^2 \hat{T} \hat{n}_{\text{H}}}, \quad (90)$$

where $u_{\text{rad}} = \hat{u}_{\text{rad}} u_{\text{ISRF}}$.

This can be the case of alignment in a part of comet atmosphere.¹⁷ Naturally, combining equations (89) and (90) it is possible to establish when streaming defines the alignment axis in spite of the presence of magnetic field.

11.7 AMO and mechanical alignment of helical grains

Our present paper is devoted to RATs and the alignment that they entail.

However, our consideration of a helical grain is quite general. In fact, the functional dependence of the torques that we obtain for our model grain is valid when atoms rather than photons are reflected from the mirror. Therefore we may predict that for elastic gas-grain collisions the helical grains¹⁸ will align with long grain axes perpendicular to the flow in the absence of magnetic field and with long axes perpendicular to \mathbf{B} , when dynamically important magnetic field is present. If atoms attach to the grain surface and then are thermally ejected from it, this changes the values of torques by a factor of the order of unity. The only way that the uncompensated torques can vanish for a helical grain is if the correlation is lost between the place at which the atom strikes the grain surface and leaves it.¹⁹ The latter is rather improbable for sufficiently large grains. As the result, one has to conclude that helicity is a generic property of the interaction of irregular grains and atomic flows.

This conclusion alters substantially the paradigm of grain motions in diffuse gas. Since the time when Gold (1951) proposed his first simple model of mechanical alignment, it was considered essential to have supersonic grain-gas velocities to achieve any tangible alignment. Indeed, both the Gold original process and the ones proposed for suprathermally rotating grains, namely, cross-sectional and crossover alignments (Lazarian 1995) require the supersonic drift to ensure that the momentum deposited in a regular way exceeds one deposited due to thermal atomic motions. This is not a requirement for the alignment of helical grains! For those the regular momentum is deposited in proportion to the number of collisions, while the randomization adds up only as a random walk. In fact, the difference between the mechanical alignment of spheroidal and helical grains is similar to the difference between the stochastic Harwit (1970) alignment by stochastic absorption of photons and the RAT alignment. While the Harwit alignment requires very special conditions dominate, the regular RATs easily beat randomization.

Similarly as in the case of RATs, where it is frequently possible to disregard the Harwit process, it should be possible to disregard the Gold-type processes²⁰ for the alignment of helical grains.

¹⁷ Another case also relevant to the comet atmosphere is that the grains have electric dipole moments, while comet atmosphere has electric field. Then the comet electric field defines the axis of alignment.

¹⁸ The mechanical alignment of helical grains was briefly discussed in Lazarian (1995) and Lazarian et al. (1997), but was not elaborated there.

¹⁹ Even in this case the local anisotropies of the surface at the place of atom impact can result in effective helicity similar to the case of damped oscillator in Fig. 18 (lower panel).

²⁰ This alignment tends to minimize grain cross-section, which means, for instance, that for grains streaming along magnetic fields the non-helical stochastic torques will tend to align grains with longer axes parallel to magnetic field, while helical torques will tend to align in the perpendicular direction.

Note that because of the property of helicity not to change sign during grain flipping, we do not expect to observe the thermal trapping effects described in LD99a to be present for the mechanical spin-up of helical grains. The effects that decrease the efficiency of the mechanical alignment of helical grains are discussed elsewhere.

In typical conditions of diffuse ISM, the mechanical alignment of helical grains tends to act to align grains in the same direction as the RATs, that is, with longer axes perpendicular to magnetic field. The relative role of the two mechanisms should be revealed by further research. The currently available data (see Lazarian 2007) agree with the RAT mechanism being the primary source of alignment. However, the situations are possible, when mechanical alignment reveals magnetic field, when RATs fail to do so.

12 SUMMARY

In this paper, we studied the properties of RATs, and how different RAT components affect the grain alignment. Briefly, our results are as follows.

(1) We found that a simple model of a helical grain which consists of a reflecting spheroidal grain with an attached mirror reproduces well the functional dependences of RATs obtained for irregular grains using DDSCAT.

(2) From the generic properties of RATs we predicted the preferential alignment of grains with long axes perpendicular to the direction towards the source of light, provided that magnetic field effect is subdominant.

(3) The magnetic field is important and defines the axis of alignment when it induces the Larmor precession that is faster than the precession arising from the Q_{e3} -component of RATs, that is, the component not related to grain helicity. This component is present for spheroidal grain, for instance.

(4) When magnetic field is important, RATs tend to provide both the alignment of long grain axes perpendicular to magnetic field. With or without magnetic field, most of grains are driven to the low angular momentum attractor points, as RATs align grains. Grains can be driven to the low- J attractor points on the time-scales much less than the gaseous damping time. The very existence of the high angular momentum attractor points, and therefore grains rotating much faster than the thermal velocity, is not a default and depends on the ratio Q_{e1} and Q_{e2} components.

(5) RATs can also induce ‘wrong alignment’, that is, the alignment with long grain axes parallel to magnetic field. The range of angles for ‘wrong alignment’ is narrowly centred around the $\pi/2$ angle between the direction of light and magnetic field. This range is expected to be diminished when thermal fluctuations are accounted for. Thus the RAT alignment is capable to account for most of the observed polarization.

(6) RATs exhibit approximate self-similarity that allows one to express them as a function of the ratio of the wavelength to grain size. The dynamics of the grains can be reproduced relatively accurately when the self-similarity is used.

(7) The RAT alignment is a particular case of the alignment of the helical grains. Therefore our results can be generalized to describe the mechanical alignment of irregular grains. Such an alignment is efficient for both supersonic and subsonic gaseous flows. The mechanical alignment may happen either with respect to the magnetic field or the direction of the flow depending on the rates of precession that are induced by the flow and magnetic field, respectively.

ACKNOWLEDGMENTS

We acknowledge the support by the NSF Centre for Magnetic Self-Organization in Laboratory and Astrophysical Plasmas. AL acknowledges a partial support by the NSF grant AST 0507164. We thank the anonymous referee for his/her comments which improved the paper, especially for comments on the symmetries of the RAT components.

REFERENCES

- Abbas M. M. et al., 2004, ApJ, 614, 781
 Bastien P., Jenness T., Molnar J., 2005, in Adamson A., Aspin C., Davis C. J., Fujiyoshi T., eds, ASP Conf. Ser. Vol. 343, Astronomical Polarimetry: Current Status and Future Directions. Astron. Soc. Pac., San Francisco, p. 69
 Bethell T., Cherpunov A., Lazarian A., Kim J., 2007, ApJ, in press
 Bohren C., 1974, Chem. Phys. Lett., 29, 458
 Cho J., Lazarian A., 2005, ApJ, 631, 361
 Cho J., Lazarian A., 2006, ApJ, submitted
 Davis L., Greenstein J. L., 1951, ApJ, 114, 206
 Dolginov A. Z., 1972, Ap&SS, 16, 337
 Dolginov A. Z., Mytrophanov I. G., 1976, Ap&SS, 43, 291
 Dolginov A. Z., Silantev N. A., 1976, Ap&SS, 43, 337
 Draine B., 1985, ApJS, 57, 587
 Draine B., Flatau P., 1994, J. Opt. Soc. Am. A, 11, 1491
 Draine B., Lazarian A., 1998, ApJ, 508, 157
 Draine B., Lee H., 1984, ApJ, 285, 89
 Draine B., Weingartner J., 1996, ApJ, 470, 551 (DW96)
 Draine B., Weingartner J., 1997, ApJ, 480, 633 (DW97)
 Gold T., 1951, Nat, 169, 322
 Goodman A., Jones T., Lada E., Myers P., 1995, ApJ, 448, 748
 Hall J., 1949, Sci, 109, 166
 Harwit M., 1970, Nat, 226, 61
 Hildebrand R., 2002, in Trujillo-Bueno J., Moreno-Insertis F., Sanchez F., eds, Astrophysical Spectropolarimetry. Cambridge Univ. Press, Cambridge, p. 265
 Hildebrand R., Davidson J. A., Dotson J. L., Wovell C. D., Novak G., Vaillancourt J. E., 2000, PASP, 112, 1215
 Hiltner W., 1949, Sci, 109, 165
 Hoang T., Lazarian A., 2007, MNRAS, submitted
 Jones M., Spitzer L., 1967, ApJ, 147, 943
 Lazarian A., 1994, MNRAS, 268, 713
 Lazarian A., 1995, ApJ, 453, 229
 Lazarian A., 1997a, MNRAS, 288, 609
 Lazarian A., 1997b, ApJ, 483, 296
 Lazarian A., 2003, J. Quant. Spectrosc. Radiat. Transfer, 79, 881
 Lazarian A., 2007, J. Quant. Spectrosc. Radiat. Transfer, 106, 225
 Lazarian A., Draine B., 1999a, ApJ, 516, L37 (LD99a)
 Lazarian A., Draine B., 1999b, ApJ, 520, L67 (LD99b)
 Lazarian A., Roberge W., 1997, ApJ, 484, 230
 Lazarian A., Goodman A. A., Myers P. C., 1997, ApJ, 490, 273
 Lebedev P., 1901, Ann. der Physik, 6, 433
 Lee H., Draine B., 1985, ApJ, 290, 211
 Mathis J., 1986, ApJ, 308, 281
 Mathis J., Mezger P., Panagia N., 1983, A&A, 128, 212
 Novak G. et al., 2004, in Antebi J., Lemke D., eds, Proceedings of the SPIE, Vol. 5498, Millimeter and Submillimeter Detectors for Astronomy II, p. 278
 Pelkonen V., Juvela M., Padoan P., 2007, A&A, 461, 551
 Purcell E., 1979, ApJ, 231, 404
 Purcell E., Spitzer L., 1971, ApJ, 167, 31
 Roberge W., Hanany S., 1990, BAAS, 22, 862
 Roberge W. D., DeGraff T. A., Flaherty J. E., 1993, ApJ, 418, 287
 Roberge W. G., Lazarian A., 1999, MNRAS, 305, 615
 Rosenbush V., Kolokolova L., Lazarian A., Shakhovskoy N., Kiselev N., 2007, Icarus, 186, 317
 Serkowski K., Mathewson D. S., Ford V. L., 1975, ApJ, 196, 261
 Spitzer L., McGlynn T. A., 1979, ApJ, 231, 417
 Vishniac E., Lazarian A., Cho J., 2003, in Falgarone E., Passot T., eds, Lecture Notes in Physics, Vol. 614, Turbulence and Magnetic Fields in Astrophysics. p. 376
 Ward-Thompson D., Kirk J. M., Crutcher R. M., Greaves J. S., Holland W. S., Andre P., 2000, ApJ, 537, L135
 Weingartner J., Draine B., 2001, ApJ, 548, 296
 Weingartner J., Draine B., 2003, ApJ, 589, 289 (WD03)

APPENDIX A: REFLECTING OBLATE SPHEROID

The toy model of a grain (see Fig. 2) allows us to derive analytical formulae for RATs. Let us consider RATs for an oblate reflecting spheroid characterized by semi-axes a, b where $s = a/b < 1$ (see Fig. A1). $\hat{a}_1, \hat{a}_2, \hat{a}_3$ are principal axes of the spheroid with moments of inertia $I_1 > I_2 = I_3$, respectively. Assuming that a photon beam of wavelength λ is shined along $\mathbf{k} \parallel \hat{e}_1$, the photon reflections happen on the spheroidal surface at the location determined by a normal unit vector \hat{N} and a radius \mathbf{r} . For the sake of simplicity, a perfect reflection is always assumed in this study. The location of impact on the grain surface is specified by the radius \mathbf{r} and the normal vector \hat{N} , which are, respectively, given by

$$\mathbf{r} = a \sin \eta \hat{a}_1 + b \cos \eta \cos \xi \hat{a}_2 + b \cos \eta \sin \xi \hat{a}_3, \quad (\text{A1})$$

$$\hat{N} = a_1 \sin \eta \hat{a}_1 + b_1 \cos \eta \cos \xi \hat{a}_2 + b_1 \cos \eta \sin \xi \hat{a}_3, \quad (\text{A2})$$

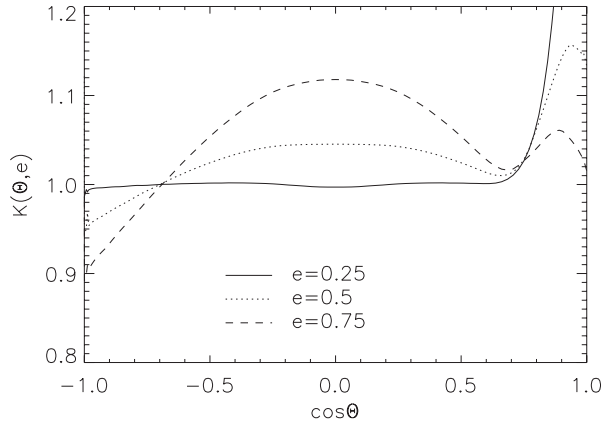
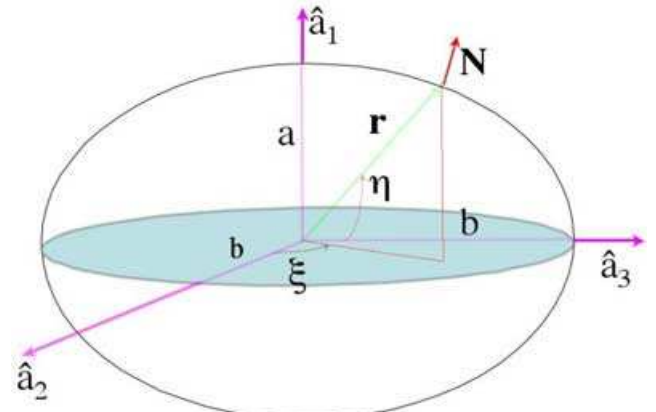


Figure A1. Upper panel represents the coordinates and vectors for the spheroid. Lower panel shows the fitting function $K(\Theta, e)$ for Q_{e3} , depending on the eccentricity of the spheroid e and its angle with light beam Θ .

where $a_1 = [\sin^2 \eta + (1 - e^2 \cos^2 \eta)]^{-1/2}$, $b_1 = a_1(1 - e^2)^{1/2}$ and e is the eccentricity of the spheroid, $\xi = [0, \pi]$, $\eta = [-\pi/2, \pi/2]$ (see Fig. A1; see also Roberge, DeGraff & Flaherty 1993).

Due to the symmetry around $\hat{\mathbf{a}}_1$, we only need to find RATs for a single rotation angle, for example, for $\beta = 0$. Therefore, when the grain axis \mathbf{a}_1 makes an angle Θ with respect to the photon beam, we have

$$\hat{\mathbf{a}}_1 = \cos \Theta \hat{\mathbf{e}}_1 + \sin \Theta \hat{\mathbf{e}}_2, \quad (\text{A3})$$

$$\hat{\mathbf{a}}_2 = -\sin \Theta \hat{\mathbf{e}}_1 + \cos \Theta \hat{\mathbf{e}}_2, \quad (\text{A4})$$

$$\hat{\mathbf{a}}_3 = \hat{\mathbf{e}}_3. \quad (\text{A5})$$

Substituting equations (A3)–(A5) into (A1) and (A2) we obtain

$$\begin{aligned} \mathbf{r} = & (a \cos \Theta \sin \eta - b \sin \Theta \cos \eta \cos \xi) \hat{\mathbf{e}}_1 \\ & + (a \sin \Theta \sin \eta + b \cos \Theta \cos \eta \cos \xi) \hat{\mathbf{e}}_2 \\ & + b \cos \eta \sin \xi \hat{\mathbf{e}}_3, \end{aligned} \quad (\text{A6})$$

$$\begin{aligned} \hat{\mathbf{N}} = & (a_1 \cos \Theta \sin \eta - b_1 \sin \Theta \cos \eta \cos \xi) \hat{\mathbf{e}}_1 \\ & + (a_1 \sin \Theta \sin \eta + b_1 \cos \Theta \cos \eta \cos \xi) \hat{\mathbf{e}}_2 \\ & + b_1 \cos \eta \sin \xi \hat{\mathbf{e}}_3. \end{aligned} \quad (\text{A7})$$

Hence, RAT produced by the photon beam is defined by

$$d\Gamma_{\text{rad}} = \gamma \mathbf{r} \times \Delta \mathbf{P} = -2p\gamma F dA(\mathbf{k} \cdot \hat{\mathbf{N}})[\mathbf{r} \times \hat{\mathbf{N}}], \quad (\text{A8})$$

where γ is the anisotropy degree of radiation field, p_{ph} is the momentum of each photon, F is the flux of the incident light beam and dA is an area element on the grain surface given by

$$dA = eb^2 f(\eta) \cos \eta d\eta d\xi, \quad (\text{A9})$$

$$\text{where } f(\eta) = \sqrt{\frac{1-e^2}{e^2} + \sin^2 \eta}.$$

Therefore

$$\begin{aligned} d\Gamma_{\text{rad}} = & -2p_{\text{ph}}\gamma F(\hat{\mathbf{e}}_1 \cdot \hat{\mathbf{N}}) dA[(r_2 N_3 - r_3 N_2) \hat{\mathbf{e}}_1 + (r_3 N_1 - r_1 N_3) \hat{\mathbf{e}}_2 \\ & + (r_1 N_2 - r_2 N_1) \hat{\mathbf{e}}_3]. \end{aligned} \quad (\text{A10})$$

Substituting $p_{\text{ph}} = \frac{h}{\lambda}$, $F = n_{\text{ph}}c = \frac{u_{\text{rad}}}{hc/\lambda}c = \frac{u_{\text{rad}}\lambda}{h}$, and dA from equation (A9) into the above equation, we obtain

$$\begin{aligned} d\Gamma_{\text{rad}} = & \frac{\gamma u_{\text{rad}}\lambda b^2}{2} \left\{ -\frac{4e}{\lambda}(\hat{\mathbf{e}}_1 \cdot \hat{\mathbf{N}})[(r_2 N_3 - r_3 N_2) \hat{\mathbf{e}}_1 \right. \\ & \left. + (r_3 N_1 - r_1 N_3) \hat{\mathbf{e}}_2 + (r_1 N_2 - r_2 N_1) \hat{\mathbf{e}}_3] f(\eta) \cos \eta d\eta d\xi \right\}. \end{aligned} \quad (\text{A11})$$

From equations (A7) and (A8), we get

$$r_2 N_3 - r_3 N_2 = \frac{ab_1 - ba_1}{2} \sin 2\eta \sin \xi \sin \Theta, \quad (\text{A12})$$

$$r_3 N_1 - r_1 N_3 = \frac{ab_1 - ba_1}{2} \sin 2\eta \sin \xi \cos \Theta, \quad (\text{A13})$$

$$r_1 N_2 - r_2 N_1 = \frac{ab_1 - ba_1}{2} \sin 2\eta \cos \xi. \quad (\text{A14})$$

Plugging equations (A12)–(A14) into equation (A11), and integrating over the surface, we obtain

$$\Gamma_{\text{rad}} = \frac{\gamma u_{\text{rad}}\lambda b^2}{2}(Q_{e1}\hat{\mathbf{e}}_1 + Q_{e2}\hat{\mathbf{e}}_2 + Q_{e3}\hat{\mathbf{e}}_3), \quad (\text{A15})$$

where the RAT components are given by

$$\begin{aligned} Q_{e1} = & \int_{-\pi/2}^{\pi/2} \int_0^\pi \frac{-4e}{\lambda} \frac{ab_1 - ba_1}{2} |a_1 \sin \eta \cos \Theta \\ & - b_1 \cos \eta \cos \xi \sin \Theta| \sin 2\eta \sin \xi \sin \Theta f(\eta) \cos \eta d\xi d\eta, \end{aligned} \quad (\text{A16})$$

$$\begin{aligned} Q_{e2} = & \int_{-\pi/2}^{\pi/2} \int_0^\pi \frac{-4e}{\lambda} \frac{ab_1 - ba_1}{2} |a_1 \sin \eta \cos \Theta \\ & - b_1 \cos \eta \cos \xi \sin \Theta| \sin 2\eta \sin \xi \cos \Theta f(\eta) \cos \eta d\xi d\eta, \end{aligned} \quad (\text{A17})$$

$$\begin{aligned} Q_{e3} = & \int_{-\pi/2}^{\pi/2} \int_0^\pi \frac{-4e}{\lambda} \frac{ab_1 - ba_1}{2} |a_1 \sin \eta \cos \Theta \\ & - b_1 \cos \eta \cos \xi \sin \Theta| \sin 2\eta \cos \xi f(\eta) \cos \eta d\xi d\eta. \end{aligned} \quad (\text{A18})$$

Note that we use the absolute value for $\hat{\mathbf{e}}_1 \cdot \hat{\mathbf{N}}$ because in the integral over η , we always use the range $[-\pi/2, \pi/2]$.

Due to the presence of the term $\sin \xi$ in equations (A16) and (A17), their integrals over the range $\xi = [0, \pi]$ vanish. The integral given by equation (A18) provides us a function of Θ which can be fitted by a function $\sin 2\Theta$ and a fitting factor

$$Q_{e3}(\Theta) = \frac{2ea}{\lambda}(s^2 - 1)K(\Theta, e) \sin 2\Theta, \quad (\text{A19})$$

where $K(\Theta, e)$ is a function of e and Θ (see the lower panel in Fig. A1).

Thus, unpolarized radiation produces only the third component of RATs, that is, Q_{e3} for the spheroid, while two first components Q_{e1} , Q_{e2} vanish.

APPENDIX B: MIRROR ON A POLE MODEL

B1 RATs calculations

Consider now a grain consisting of a square reflective mirror of side l_2 , attached to the spheroid by a pole of the length l_1 (see Fig. 2). Here we calculate RATs acting on the mirror. Its orientation in the grain coordinate system, $\hat{\mathbf{a}}_1$, $\hat{\mathbf{a}}_2$, $\hat{\mathbf{a}}_3$, is characterized by a normal unit vector $\hat{\mathbf{N}}$, given by

$$\hat{\mathbf{N}} = n_1 \hat{\mathbf{a}}_1 + n_2 \hat{\mathbf{a}}_2, \quad (\text{B1})$$

where $n_1 = \sin \alpha$, $n_2 = \cos \alpha$ with α the angle between $\hat{\mathbf{N}}$ and $\hat{\mathbf{a}}_2$ (see Fig. 2). The use of the grain coordinate system is appropriate as the spheroidal body determines the grain inertia.

Since $l_1 \gg l_2$, the radius vector determining the position of each reflecting event on the mirror surface \mathbf{r} is nearly parallel to $\hat{\mathbf{a}}_3$, thus

$$\mathbf{r} = l_1 \hat{\mathbf{a}}_3. \quad (\text{B2})$$

The orientation of the grain in the lab coordinate system is determined by Θ and β as follows:

$$\hat{\mathbf{a}}_1 = \cos \Theta \hat{\mathbf{e}}_1 + \sin \Theta \hat{\mathbf{e}}_2, \quad (\text{B3})$$

$$\hat{\mathbf{a}}_2 = \cos \beta [-\sin \Theta \hat{\mathbf{e}}_1 + \cos \Theta \hat{\mathbf{e}}_2] + \sin \beta \hat{\mathbf{e}}_3, \quad (\text{B4})$$

$$\hat{\mathbf{a}}_3 = -\sin \beta [-\sin \Theta \hat{\mathbf{e}}_1 + \cos \Theta \hat{\mathbf{e}}_2] + \cos \beta \hat{\mathbf{e}}_3. \quad (\text{B5})$$

Plugging equations (B3–B5) into equations (B1) and (B2) we get

$$\begin{aligned} \hat{\mathbf{N}} = & \hat{\mathbf{e}}_1(n_1 \cos \Theta - n_2 \cos \beta \sin \Theta) \\ & + \hat{\mathbf{e}}_2(n_1 \sin \Theta + n_2 \cos \beta \cos \Theta) \\ & + \hat{\mathbf{e}}_3 n_2 \sin \beta, \end{aligned} \quad (\text{B6})$$

$$\mathbf{r} = l_1(\hat{\mathbf{e}}_1 \sin \beta \sin \Theta - \hat{\mathbf{e}}_2 \sin \beta \cos \Theta + \hat{\mathbf{e}}_3 \cos \beta). \quad (\text{B7})$$

Hence, RAT produced by the photon beam acting on the mirror is

$$d\Gamma_{\text{rad}} = \gamma \mathbf{r} \times \Delta \mathbf{P} = (-2p_{\text{ph}})\gamma F dA(\mathbf{k} \cdot \hat{\mathbf{N}})[\mathbf{r} \times \hat{\mathbf{N}}]. \quad (\text{B8})$$

Integrating over the full mirror, RAT becomes

$$\Gamma_{\text{rad}} = -2p\gamma FA_{\perp}(\mathbf{k} \cdot \hat{\mathbf{N}})[\mathbf{r} \times \hat{\mathbf{N}}], \quad (\text{B9})$$

where $A_{\perp} = A|\hat{\mathbf{e}}_1 \cdot \hat{\mathbf{N}}|$ is the cross-section of the mirror with respect to the photon flux.

Substituting $p_{\text{ph}}, F, \mathbf{k} \equiv \hat{\mathbf{e}}_1$ and $A_{\perp} = l_2^2|\hat{\mathbf{e}}_1 \cdot \hat{\mathbf{N}}|$ into equation (B9), we get

$$\begin{aligned} \Gamma_{\text{rad}} = & \frac{\gamma u_{\text{rad}} \lambda l_2^2}{2} \left(-\frac{4}{\lambda} \right) |\hat{\mathbf{e}}_1 \cdot \hat{\mathbf{N}}|(\hat{\mathbf{e}}_1 \cdot \hat{\mathbf{N}})[(r_2 N_3 - r_3 N_2)\hat{\mathbf{e}}_1 \\ & + (r_3 N_1 - r_1 N_3)\hat{\mathbf{e}}_2 + (r_1 N_2 - r_2 N_1)\hat{\mathbf{e}}_3]. \end{aligned} \quad (\text{B10})$$

From equations (B6) and (B7), we obtain

$$\begin{aligned} \frac{r_2 N_3 - r_3 N_2}{l_1} = & -n_2 \sin \beta \cos \Theta \sin \beta \\ & - \cos \beta(n_1 \sin \Theta + n_2 \cos \beta \cos \Theta) \\ = & (-n_1 \cos \beta \sin \Theta - n_2 \cos \Theta), \end{aligned} \quad (\text{B11})$$

$$\begin{aligned} \frac{r_3 N_1 - r_1 N_3}{l_1} = & \cos \beta(n_1 \cos \Theta - n_2 \cos \beta \sin \Theta) \\ & - \sin \beta \sin \Theta n_2 \sin \beta \\ = & n_1 \cos \beta \cos \Theta - n_2 \sin \Theta, \end{aligned} \quad (\text{B12})$$

$$\frac{r_1 N_2 - r_2 N_1}{l_1} = n_1 \sin \beta. \quad (\text{B13})$$

Therefore, we can write

$$\Gamma_{\text{rad}} = \frac{\gamma u_{\text{rad}} \lambda l_2^2}{2} (Q_{e1}\hat{\mathbf{e}}_1 + Q_{e2}\hat{\mathbf{e}}_2 + Q_{e3}\hat{\mathbf{e}}_3), \quad (\text{B14})$$

where the RAT components are given by

$$\begin{aligned} Q_{e1} = & -\frac{4l_1}{\lambda} |\hat{\mathbf{e}}_1 \cdot \hat{\mathbf{N}}| (n_1 \cos \beta \sin \Theta + n_2 \cos \Theta) [-n_1 \cos \Theta \\ & + (n_2 \cos \beta) \sin \Theta], \end{aligned} \quad (\text{B15})$$

$$\begin{aligned} Q_{e2} = & -\frac{4l_1}{\lambda} |\hat{\mathbf{e}}_1 \cdot \hat{\mathbf{N}}| (n_1 \cos \beta \cos \Theta - n_2 \sin \Theta) [n_1 \cos \Theta \\ & - n_2 \cos \beta \sin \Theta], \end{aligned} \quad (\text{B16})$$

$$Q_{e3} = -\frac{4l_1}{\lambda} |\hat{\mathbf{e}}_1 \cdot \hat{\mathbf{N}}| n_1 \sin \beta [n_1 \cos \Theta - n_2 \cos \beta \sin \Theta]. \quad (\text{B17})$$

Simplifying the above equations, we get

$$\begin{aligned} Q_{e1} = & \frac{4l_1}{\lambda} |n_1 \cos \Theta - n_2 \sin \Theta \cos \beta| \left[n_1 n_2 \cos^2 \Theta \right. \\ & \left. + \frac{n_1^2}{2} \cos \beta \sin 2\Theta - \frac{n_2^2}{2} \cos \beta \sin 2\Theta - n_1 n_2 \sin^2 \Theta \cos^2 \beta \right], \end{aligned} \quad (\text{B18})$$

$$\begin{aligned} Q_{e2} = & -\frac{4l_1}{\lambda} |n_1 \cos \Theta - n_2 \sin \Theta \cos \beta| \left[n_1^2 \cos \beta \cos^2 \Theta \right. \\ & \left. - \frac{n_1 n_2}{2} \cos^2 \beta \sin 2\Theta - \frac{n_1 n_2}{2} \sin 2\Theta + n_2^2 \cos \beta \sin^2 \Theta \right], \end{aligned} \quad (\text{B19})$$

$$\begin{aligned} Q_{e3} = & -\frac{4l_1}{\lambda} |n_1 \cos \Theta - n_2 \sin \Theta \cos \beta| n_1 \sin \beta [n_1 \cos \Theta \\ & - n_2 \cos \beta \sin \Theta]. \end{aligned} \quad (\text{B20})$$

Averaging over the rotational angle β in the range $[0, 2\pi]$, we get

$$Q_{e1} = \frac{4\pi l_1 n_1 n_2}{\lambda} (3 \cos^2 \Theta - 1) f(\Theta, \alpha), \quad (\text{B21})$$

$$Q_{e2} = \frac{4\pi l_1 n_1 n_2}{\lambda} \sin 2\Theta g(\Theta, \alpha), \quad (\text{B22})$$

$$Q_{e3} = 0, \quad (\text{B23})$$

where $f(\Theta, \alpha), g(\Theta, \alpha)$ are fitting functions depending on α and Θ . The dependence on Θ characterizes the influence of variation of the mirror cross-section on RATs. We will find these fitting functions in the following section.

B2 Fitting functions

As we have seen above, RATs can be decomposed into analytical terms and fitting functions which are functions of both Θ and α (see equations B18 and B19). Below we discuss an analytical approximation to the fitting functions $f(\Theta, \alpha), g(\Theta, \alpha)$.

In the vicinity of $\Theta = 0, \pi, |n_1 \cos \Theta - n_2 \sin \Theta \cos \beta| \sim n_1$, so this factor does not make β -averaging more involved, however.

As $\Theta \sim \pi/2$, equations (B15) and (B16) can be written as

$$\begin{aligned} Q_{e1} = & \frac{4l_1}{\lambda} |-n_2 \cos \beta| \left[n_1 n_2 \cos^2 \Theta + \frac{n_1^2}{2} \cos \beta \sin 2\Theta \right. \\ & \left. - \frac{n_2^2}{2} \cos \beta \sin 2\Theta - n_1 n_2 \sin^2 \Theta \cos^2 \beta \right], \end{aligned} \quad (\text{B24})$$

$$\begin{aligned} Q_{e2} = & -\frac{4l_1}{\lambda} |-n_2 \cos \beta| \left[n_1^2 \cos \beta \cos^2 \Theta - \frac{n_1 n_2}{2} \cos^2 \beta \sin 2\Theta \right. \\ & \left. - \frac{n_1 n_2}{2} \sin 2\Theta + n_2^2 \cos \beta \sin^2 \Theta \right]. \end{aligned} \quad (\text{B25})$$

Integrating equations (B24) and (B25) over β in a range $[0, 2\pi]$, we get

$$Q_{e1} = \frac{4l_1}{\lambda} \frac{4n_1 n_2 |n_2|}{3} (5 \cos^2 \Theta - 2), \quad (\text{B26})$$

$$Q_{e2} = \frac{4l_1}{\lambda} \frac{10n_1 n_2 |n_2|}{3} \sin 2\Theta. \quad (\text{B27})$$

Comparing equations (B18) and (B19) with (B26) and (B27), we have

$$f_{\pi/2}(\Theta, \alpha) = \frac{|\cos \alpha|(5 \cos^2 \Theta - 2)}{3\pi(3 \cos^2 \Theta - 1)}, \quad (\text{B28})$$

$$g_{\pi/2}(\Theta, \alpha) = \frac{10|\cos \alpha|}{3\pi}. \quad (\text{B29})$$

The fitting functions $f_{\pi/2}(\Theta, \alpha)$ and the tabulated function $f(\Theta, \alpha)$ for $\alpha = 45^\circ$ are shown in Fig. B1.

Interestingly enough, the approximation of the fitting functions obtained in the vicinity of $\Theta \sim \pi/2$ presents a reasonable approximation for the fitting function f over the entire range of Θ . Indeed, Fig. B1 shows the tabulated function $f(\Theta, \alpha)$ obtained by substituting Q_{e1}, Q_{e2} resulted from numerically averaging equations (B15) and (B16) into equations (B18) and (B19) (solid lines) and the fitting function $f_{\pi/2}(\Theta, \alpha)$ given by equation (B28) (dashed line) for a particular case of $\alpha = 45^\circ$. It is shown that the fitting function $f_{\pi/2}(\Theta, \alpha)$ has a good agreement with $f(\Theta, \alpha)$. Similar results are also found for other α angles (see Fig. B3).

However, the fitting function $g_{\pi/2}$ given by equation (B29) is independent of Θ and therefore does not provide a good fit to the tabulated function g . In this case, we perform a quadratic fitting for

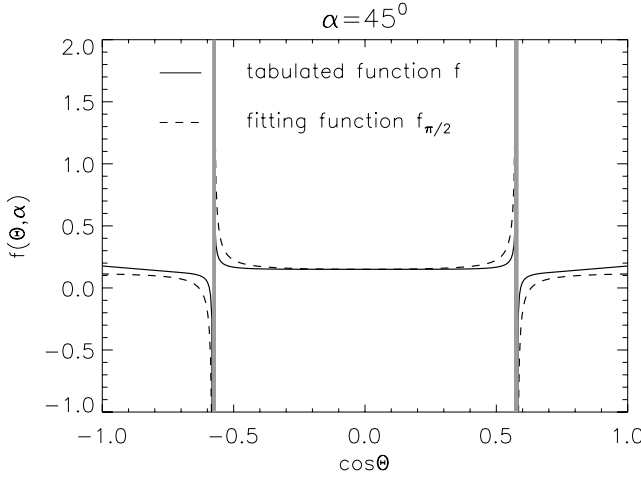


Figure B1. Tabulated and fitting functions f for $\alpha = 45^\circ$. Shaded lines show the vicinity of the singular line $\cos \Theta = 1/\sqrt{3}$.

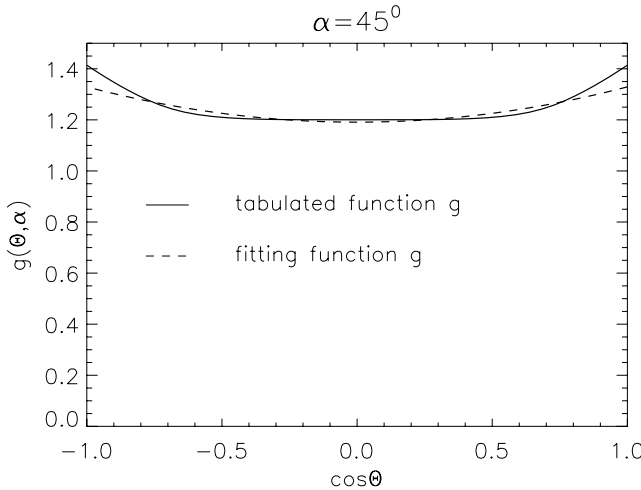


Figure B2. Tabulated and fitting functions g for $\alpha = 45^\circ$.

tabulated functions for different α angles. The results for $\alpha = 30^\circ$, 45° and 60° are given by

$$g(\Theta, \alpha = 30^\circ) = 1.4675 - 0.5 \cos^2 \Theta, \quad (\text{B30})$$

$$g(\Theta, \alpha = 45^\circ) = 1.191 + 0.1382 \cos^2 \Theta, \quad (\text{B31})$$

$$g(\Theta, \alpha = 60^\circ) = 0.864 + 0.869 \cos^2 \Theta. \quad (\text{B32})$$

Tabulated and fitting functions g are shown in Fig. B2 for $\alpha = 45^\circ$ (see Fig. B4 for g corresponding to other angles α).

Figs B3 and B4 show f, g for $\alpha = 30^\circ$ and 60° . Fig. B3 shows that there is a change in sign of the tabulated function f as $|\cos \Theta| \rightarrow 1/\sqrt{3}$ between $\alpha = 30^\circ$ and 60° . This stems from the fact that, for $\alpha < 45^\circ$, the influence of A_\perp shifts the zero of Q_{e1} from $|\cos \Theta| = 1/\sqrt{3}$ to $|\cos \Theta| < 1/\sqrt{3}$. As a result, when the term $3\cos^2 \Theta - 1$ approaches the zero from the left-hand side of $\cos \Theta = -1/\sqrt{3}$, for instance, then Q_{e1} is still positive, which causes f rise sharply to the positive direction as in Fig. B3 (upper panel).

As an example, in this paper we mostly discuss the case in which the mirror is tilted by an angle of $\alpha = \pi/4$ for which there is the best fit between the fitting function $f_{\pi/2}$ and the tabulated function

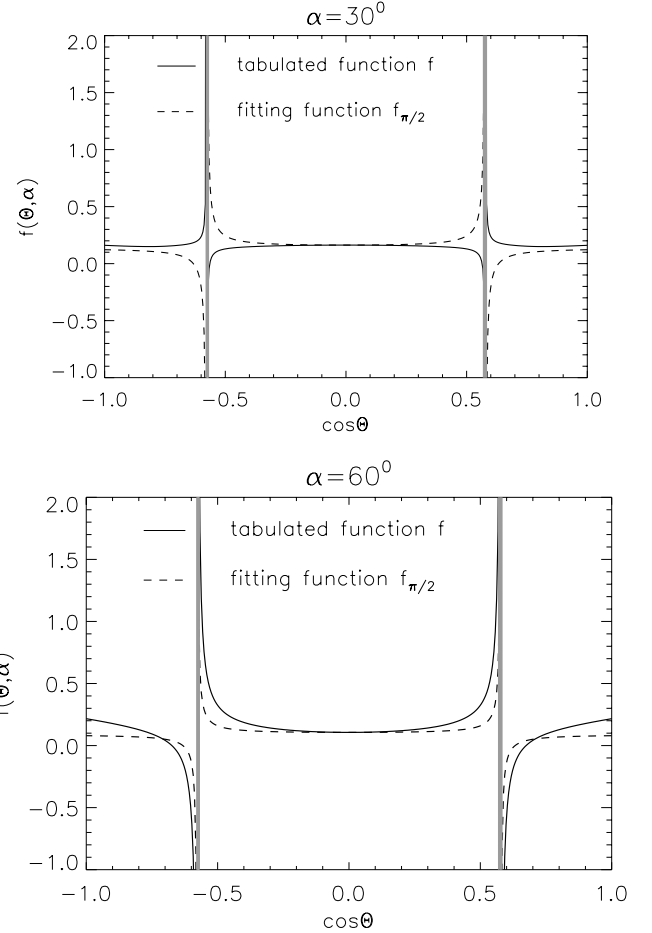


Figure B3. Fitting function f for two tilted angles of the mirror in the body system: upper and lower panels correspond to $\alpha = 30^\circ, 60^\circ$. Shaded lines show the vicinity of the singular line $|\cos \Theta| = 1/\sqrt{3}$.

f except a narrow range in the vicinity of $|\cos \Theta| = 1/\sqrt{3}$ (see Fig. B1). Similarly, g given by equation (B31) also provides a good fit for Q_{e2} (see Fig. B2). Therefore, RATs acting upon the mirror can be roughly approximated by equations (B18)–(B19) with f, g and are given in equations (B28) and (B31).

Needless to say that such an approximation entails errors in calculating the torques Q_{e1} and Q_{e2} . Fig. B5 shows the torques with f, g being the tabulated and fitting functions. It can be seen that there is a very good fit for the component Q_{e2} , but there exists some deviation for the component Q_{e1} towards the range $\cos \Theta \sim \pm 1$. These errors could be decreased by using more sophisticated analytical fits, for example, piecewise analytical fit. However, this would decrease the heuristic value of the formulae. Therefore while using the approximate fits (B28) and (B31) for some analytical calculations below, for most of the quantitative estimates, including those related to evolving the phase trajectories, we tabulate the fitting functions f and g . Naturally, the latter is equivalent to the direct use of averaged equations (B15)–(B16) for RAT components.

What is the purpose of having the analytical form of the fitting functions, if they do not provide exact fits for the torque components (see Fig. B5)? We may see that the actual RATs acting on irregular grains (e.g. Fig. 5) also differ somewhat from the corresponding AMO RATs. These differences, however, do not change substantially, as we show in the rest of the paper, the alignment of

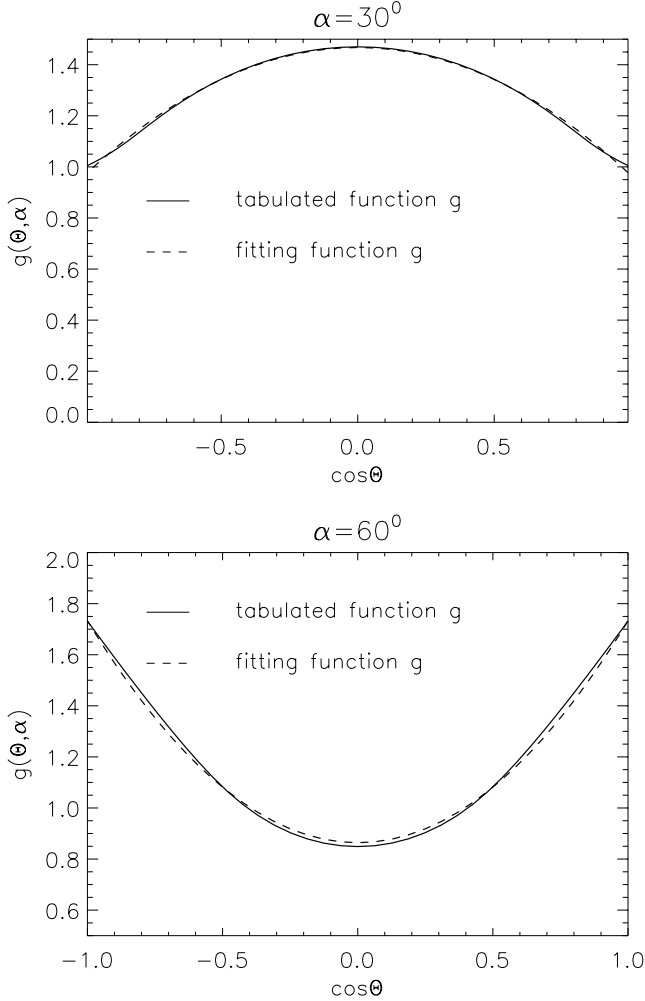


Figure B4. Fitting and tabulated functions g for two tilted angles of the mirror in the body system: upper and lower panels correspond to $\alpha = 30^\circ$, 60° .

irregular grains in comparison with the alignment predicted by AMO. Thus we believe that the slightly distorted AMO with the appropriate analytically fitting functions should also reflect correctly the generic properties of the RAT alignment.

B3 Dependences on α

Fig. B6 shows that the variation of the mirror orientation can change the ratio of their maximum $Q_{e1}^{\max}/Q_{e2}^{\max}$. Here we denote Q_{e1}^{\max} the maximum of $|Q_{e1}|$ which is exactly its amplitude at $\Theta = 0$ or π , and Q_{e2}^{\max} the maximum of Q_{e2} . In Fig. B6 it is obviously shown that $Q_{e1}^{\max}/Q_{e2}^{\max}$ increases with α , increasing due to the increase of the cross-section A_\perp . However, the ratio Q_{e1}^{\max}/Q_{e2} is limited to the upper limit of 1.3. We will see later that the ratio plays an important role on the alignment that is discussed in Section 7.5.

Moreover, the variation of α does not only give rise to the change of the ratio $Q_{e1}^{\max}/Q_{e2}^{\max}$, but it can also affect the symmetric functional form of RATs. Our calculations show that for α smaller than 20° or larger than 80° , the RATs have some changes in the functional form of the Q_{e1} and Q_{e2} compared to what is shown in Fig. 3.

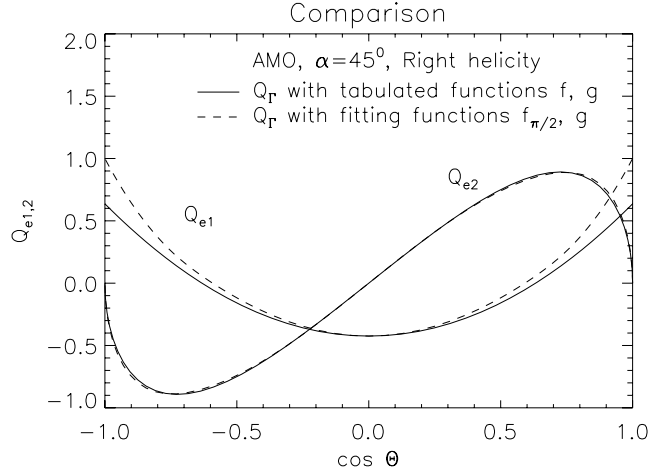


Figure B5. The comparison of RAT components. Dashed lines show RATs obtained from the analytical approximation given by equations (B18)–(B19) and solid lines show RATs obtained by numerically averaging equations (B15)–(B16) over β .

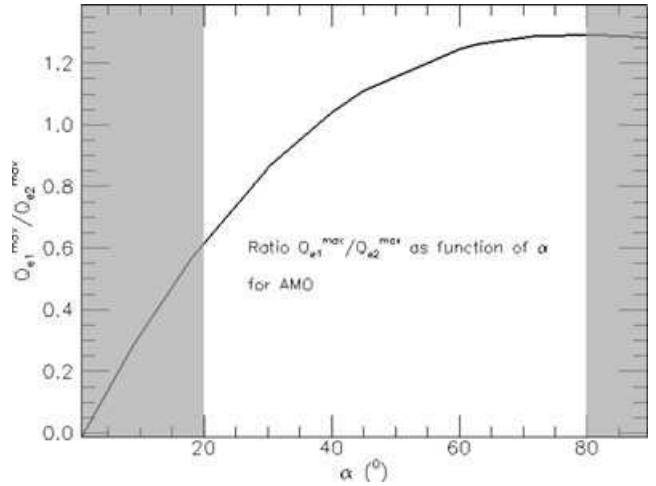


Figure B6. Variation of $Q_{e1}^{\max}/Q_{e2}^{\max}$ as a function of α . This ratio determines the existence of high- J attractor points and the shift of a crossover point as we describe in Section 6.6. Shaded areas show the range of α in which the symmetry of RATs are significantly affected by the cross-section.

Let us explain why for small α , the symmetry of RATs for AMO is affected. Consider equation (B18) with $n_1 = \sin \alpha$, $n_2 = \cos \alpha$:

$$Q_{e1} = \frac{4l_1}{\lambda} |\sin \alpha \cos \Theta - \cos \alpha \sin \Theta \cos \beta| \left[\sin \alpha \cos \alpha \cos^2 \Theta + \frac{\sin^2 \alpha}{2} \cos \beta \sin 2\Theta - \frac{\cos^2 \alpha}{2} \cos \beta \sin 2\Theta - \sin \alpha \cos \alpha \sin^2 \Theta \cos^2 \beta \right]. \quad (\text{B33})$$

The first term is the cross-section A_\perp , and the second term is Q_{e1} without cross-section. The second term when averaged gives rise to $Q_{e1} \sim 5 \cos^2 \Theta - 2$. It indicates that if the cross-section is constant, Q_{e1} is fully symmetric. Consider α small, $\cos \alpha$ is significant, and equation (B33) reduces to

$$\begin{aligned} Q_{e1} = & \frac{4l_1}{\lambda} | -\cos \alpha \sin \Theta \cos \beta | \left[\sin \alpha \cos \alpha \cos^2 \Theta \right. \\ & + \frac{\sin^2 \alpha}{2} \cos \beta \sin 2\Theta - \frac{\cos^2 \alpha}{2} \cos \beta \sin 2\Theta \\ & \left. - \sin \alpha \cos \alpha \sin^2 \Theta \cos^2 \beta \right]. \end{aligned} \quad (\text{B34})$$

Obviously, when averaging over β , the absolute term containing $\sin \Theta$ contributes to modify substantially the symmetry of the resulting torques. The same problem also occurs for Q_{e2} . We found that for both $\alpha \leq 20^\circ$ or $\alpha \geq 80^\circ$, the functional forms of RATs are very influenced. However, for α within $[20^\circ, 80^\circ]$, their functional forms are not much different from what is shown in Fig. 3 for $\alpha = 45^\circ$.

APPENDIX C: RATS WITH DDSCAT

In the discrete electric dipole approximation (Draine & Flatau 1994), a grain is presented as an ensemble of electric dipoles. The interaction between the electric field of incident light and the dipoles produces radiative forces and torques. RATs produced by radiation on a grain consisting of N electric dipoles are

$$\Gamma_{\text{rad}} = \sum_{j=1}^N \mathbf{r}_j \times \mathbf{F}_j + \sum_{j=1}^N \mathbf{p}_j \times \mathbf{E}_j, \quad (\text{C1})$$

where \mathbf{r}_j is radius of j th dipole, $\mathbf{E}_j, \mathbf{F}_j$ are electric field at the location of, and radiative force which acts on the j th dipole. Radiative force \mathbf{F} present in equation (C1) is produced by the gradient of electric field in the grain and the Lorentz force due to vibration of electric dipole in magnetic field.

Radiation field inside the grain consists of that of incident and scattered light. Each dipole receives the incident light which induces its vibration and scattered light produced by all electric dipoles except the dipole under study. Hence, the total RAT can be written in a different form:

$$\Gamma_{\text{rad}} = \Gamma_{\text{inc}} + \Gamma_{\text{sca}}. \quad (\text{C2})$$

RAT efficiency \mathcal{Q}_{Γ} is defined as follows:

$$\Gamma_{\text{rad}} = \frac{u_{\lambda} a_{\text{eff}}^2 \lambda}{2} \gamma \mathcal{Q}_{\Gamma}, \quad (\text{C3})$$

where γ is the anisotropy, and u_{λ} is the energy density of radiation field of wavelength λ . Hence, equation (C2) can be rewritten as

$$\mathcal{Q}_{\Gamma} = \mathcal{Q}_{\text{inc}} + \mathcal{Q}_{\text{sca}}. \quad (\text{C4})$$

Here $\mathcal{Q}_{\text{inc}} \equiv \mathcal{Q}_{\text{abs}}$ and \mathcal{Q}_{sca} are given by (DW96)

$$\begin{aligned} \mathcal{Q}_{\text{inc}} = & \frac{4k}{a_{\text{eff}}^2 |E_{\text{inc},0}|^2} \operatorname{Re} \sum_{j=1}^N \mathbf{p}_j(0) \times \mathbf{E}_{\text{inc},0} e^{ik\mathbf{r}_j} \\ & - ik \times \sum_{j=1}^N \mathbf{r}_j [\mathbf{p}_j \cdot \mathbf{E}_{\text{inc},0}] e^{ik\mathbf{r}_j}, \end{aligned} \quad (\text{C5})$$

$$\mathcal{Q}_{\text{sca}} = \frac{-k^5}{\pi a_{\text{eff}}^2 |E_{\text{inc},0}|^2} \int d\Omega \operatorname{Re}(S_E^* V_B + S_B^* V_E). \quad (\text{C6})$$

In the above equations, \mathbf{E}_{inc} denotes electric field of incident light, S_E, S_B, V_E, V_B are given by

$$S_E = \sum_{j=1}^N [\mathbf{r}_j - (\hat{\mathbf{n}} \cdot \mathbf{r}_j) \hat{\mathbf{n}} - \frac{2i}{k} \hat{\mathbf{n}}] \cdot \mathbf{p}_j(0) \exp(-ik\hat{\mathbf{n}} \cdot \mathbf{r}_j), \quad (\text{C7})$$

$$S_B = \mathbf{r} \cdot \sum_{j=1}^N \mathbf{p}_j(0) \times \mathbf{r}_j \exp(-ik\hat{\mathbf{n}} \cdot \mathbf{r}_j), \quad (\text{C8})$$

$$V_E = \sum_{j=1}^N \mathbf{p}_j(0) - \hat{\mathbf{n}}[\hat{\mathbf{n}} \cdot \mathbf{p}_j(0) \exp(-ik\hat{\mathbf{n}} \cdot \mathbf{r}_j)], \quad (\text{C9})$$

$$V_B = -\hat{\mathbf{N}} \times V_E, \quad (\text{C10})$$

where \mathbf{p}_j is j th electric dipole moment, k is wavenumber, \mathbf{r} is the radius vector and $\hat{\mathbf{n}}$ is normal unit vector.

We use DDSCAT code to compute separately the components arising from absorption, scattering and total RAT for a grain in which its direction with respect to \mathbf{k} is determined by the angles Θ, β, Φ (see Fig. 1). Here Θ is the angle between \mathbf{a}_1 and \mathbf{k} ; β is the rotational angle of the grain around \mathbf{a}_1 and Φ is the precession angle of \mathbf{a}_1 about \mathbf{k} . For our study (see Table 1), we compute RATs for the spectrum of the ISRF, over 21 directions of Θ from 0 to π and 21 values of β from 0 to 2π , at $\Phi = 0$.

RAT can be decomposed into components in the scattering system via

$$\mathcal{Q}_{\Gamma} = Q_{e1}\hat{e}_1 + Q_{e2}\hat{e}_2 + Q_{e3}\hat{e}_3, \quad (\text{C11})$$

where $\hat{e}_1, \hat{e}_2, \hat{e}_3$ are shown in Fig. 1.

Mean RAT over wavelengths, $\overline{\mathcal{Q}}(\Theta, \beta, \Phi)$ is defined by

$$\overline{\mathcal{Q}} = \frac{\int \mathcal{Q}_{\lambda} u_{\lambda} d\lambda}{\int u_{\lambda} d\lambda}. \quad (\text{C12})$$

Since β varies very fast due to the swift rotation of the grain around the axis of major inertia \mathbf{a}_1 , we can average RATs over β from 0 to 2π .

APPENDIX D: ATTRACTOR AND REPELLOR POINTS

Here we derive the condition for which a stationary point becomes an attractor and a repeller point following the approach in DW97. Assuming that the stationary point has the angle ξ_s with respect to magnetic field and angular momentum J_s , one can expand the right-hand sides of equations of motion around this point. As a result, equations (66) and (67) give

$$\frac{d\xi}{dt} = \frac{\langle F(\xi_s) \rangle_{\phi}}{J_s} + \frac{d\langle F \rangle_{\phi}}{J_s d\xi}(\xi_s, J_s) - \frac{\langle F(\xi_s) \rangle_{\phi}}{J_s^2}(J - J_s), \quad (\text{D1})$$

$$\frac{dJ}{dt} = \langle H(\xi_s) \rangle_{\phi} - J_s + \frac{d\langle H \rangle_{\phi}}{d\xi}(\xi - \xi_s) - (J - J_s), \quad (\text{D2})$$

where $\langle H(\xi) \rangle_{\phi}, \langle F(\xi) \rangle_{\phi}$ are spinning and aligning torques already averaged over the precession angle ϕ . Since for stationary points ξ_s, J_s , we have $\langle F(\xi_s) \rangle_{\phi} = 0, \langle H(\xi_s) \rangle_{\phi} - J_s = 0$, equations (D1) and (D2) become

$$\frac{d\xi}{dt} = A(\xi - \xi_s) + B(J - J_s), \quad (\text{D3})$$

$$\frac{d\omega}{dt} = C(\xi - \xi_s) + D(J - J_s), \quad (\text{D4})$$

where

$$A = \frac{d\langle F \rangle_{\phi}}{J_s d\xi}(\xi_s, J_s), \quad (\text{D5})$$

$$B = -\frac{\langle F(\xi_s) \rangle_{\phi}}{J_s^2}, \quad (\text{D6})$$

$$C = \frac{d\langle H \rangle_\phi}{d\xi}(\xi_s, J_s), \quad (D7)$$

$$D = -1. \quad (D8)$$

To have an attractor point, one requires

$$A + D < 0, \quad (D9)$$

$$BC - AD < 0. \quad (D10)$$

In other words,

$$\frac{d\langle F \rangle_\phi}{\langle H \rangle_\phi d\xi}(\xi_s, J_s) < 1, \quad (D11)$$

$$H \frac{d\langle F \rangle_\phi}{d\xi}(\xi_s, J_s) < \langle F \rangle_\phi \frac{d\langle H \rangle_\phi}{d\xi}(\xi_s, J_s), \quad (D12)$$

where we have substituted $J_s = H(\xi_s)$.

APPENDIX E: EFFECTIVE GRAIN SIZE FOR AMO

For phase maps, we numerically average equations (10)–(12) to obtain exact RATs for AMO, rather than using approximate formulae as in the analysis. However, for this case, the absolute magnitude of torques matters. Therefore, we normalize AMO in the following way. Assuming that the size l_2 of the mirror and l_1 are chosen so that the RAT for AMO has the magnitude equal to that of irregular grain of an effective size a_{eff} . Thus, following equations (1) and (9) we have

$$\frac{\lambda u_{\text{rad}} l_2^2}{2} Q_{\text{AMO}} = \frac{\lambda u_{\text{rad}} a_{\text{eff}}^2}{2} Q_{\text{DDSCAT}}, \quad (E1)$$

where Q_{AMO} and Q_{DDSCAT} are the magnitudes of RATs for AMO and an irregular grain, respectively. We can simplify further by

normalizing RAT components over the maximum of Q_{e1} , and let Q_{AMO} , Q_{DDSCAT} equal the maximum of Q_{e1} for AMO and irregular grain. As a result, for AMO, we have $Q_{\text{AMO}} = |Q_{e1}|^{\max} = \frac{16\pi n_1 n_2^2 l_1}{\lambda}$, and substituting into equation (E1), we get

$$l_2^2 l_1 = \frac{\lambda}{16\pi n_1 n_2^2} a_{\text{eff}}^2 Q_{\text{DDSCAT}}. \quad (E2)$$

We can define the effective size of AMO subject to the mirror size and the rod length as

$$a_{\text{AMO}}^2 = l_2^2 \left(\frac{l_1}{\lambda} \right). \quad (E3)$$

Equations (E5) and (E4) enables us to find the effective size of AMO that produce the same RAT magnitude with the irregular grain of size a_{eff} , given by

$$a_{\text{AMO}}^2 = \frac{1}{16\pi n_1 n_2^2} a_{\text{eff}}^2 Q_{\text{DDSCAT}}. \quad (E4)$$

As we discuss in Section 10 that the magnitude of RATs for irregular grains can be crudely approximated as

$$Q_{\text{DDSCAT}} = 0.4 \left(\frac{\lambda}{a_{\text{eff}}} \right)^\eta, \quad (E5)$$

where $\eta = 0$ for $\lambda < 1.8 a_{\text{eff}}$ and $\eta = 3$ or 4 for $\lambda > 1.8 a_{\text{eff}}$ (see Section 10).

Equations (E5) and (E4) allow us to roughly estimate the effective size of AMO, a_{AMO} as a function of the effective size of irregular grain, a_{eff} , provided that the wavelength of radiation field is known.

This paper has been typeset from a $\text{\TeX}/\text{\LaTeX}$ file prepared by the author.